UNIVERSITÀ DEGLI STUDI DI CATANIA

DOTTORATO DI RICERCA IN FISICA

CARMEN LOREDANA ALTANA

THE ROLE OF NANOSTRUCTURED TARGETS IN LASER-PRODUCED PLASMAS FOR NUCLEAR ASTROPHYSICS STUDIES

PHD THESIS

TUTORS:

PROF. CLAUDIO SPITALERI

DOTT. SALVO TUDISCO

PHD COORDINATOR:

PROF. VINCENZO BELLINI

XXIX CICLO – 2014-2017

This work has been supported by a triennial scholarship, *funded by the Italian Ministry of University MIUR under the grant "LNS-Astrofisica Nucleare (fondi premiali)" .*

Contents

List of Figures

List of Tables

Abbreviations

B-B	: Bound-Bound
CCD	: Charged Coupled Device
CE	: Coronal Equilibrium
CRE	: Collisional Radiative Equilibrium
CTE	: Complete Thermal Equilibrium
DDG	: Digital Delay Generator
DLs	: Double Layers
F-B	: Free-Bound
ICCD	: Intensified Charged Coupled Device
KL	: Knudsen Layer
LPP	: Laser Produced Plasma
LTE	: Local Thermal Equilibrium
MCP-PH	: MicroChannel Plate – Phosphor Screen
NWs	: Nanowires
QE	: Quantum Efficiency
RoI	: Region of Interest
SBS	: Stimulated Brillouin Scattering
SRS	: Stimulated Raman Scattering
ToF	: Time of Flight
TPD	: Two-Plasmon Decay
TPS	: Thomson Parabola Spectrometer
UAE	: Unsteady Adiabatic Expansion

Introduction

The laser-matter interaction is a subject of considerable theoretical as well as practical importance. The availability of extremely high-power laser beams has opened up new possibilities in the field of research. Laser beams can generate plasma from interaction with solid targets, and, in proper conditions, they can also trigger nuclear reactions. Thus, laser induced phenomena have acquired a great deal of attention from scientists working in a variety of areas like optics, materials science, plasma physics and nuclear fusion.

The aim of this work is the experimental study of laser produced plasmas for nuclear astrophysics applications.

Since the even more increasing need to find alternative methods to produce energy, substituting carbon fuels, important developments in fusion research employing high-density plasmas are required. Therefore, nuclear physics is one of the most promising field where laser produced plasmas can be employed.

Moreover, the 99% of the matter in the Universe is plasma, which has a primary role in modern astrophysics. Therefore, the investigation of the origin of stars and related phenomena dials closely with plasma physics. The measurements of nuclear reaction rates and theoretical estimations in order to understand the origin of the chemical elements and the energy generation in stars is possible thanks to Nuclear Astrophysics. It is a branch of astrophysics, which helps the understanding of the Universe through the knowledge of the microcosm of the atomic nucleus.

Therefore, Nuclear and Astrophysical research cannot be improved without a fully understanding of plasma physics. Although it is impossible to

reproduce the extreme properties of stellar matter, a methodology largely employed in other fields of plasma physics allows to rescale plasma parameters (e.g. temperature and density) in order to make similar to the real world our laboratory conditions. In fact, keV temperature plasmas can be rather easily generated in laboratory, but with densities orders of lower magnitude than the stellar ones.

In order to achieve conditions of astrophysical interest and suitable for nuclear fusion, the plasma parameters should be optimized.

On this purpose, nanostructured materials used as targets in laser-matter interaction have been studied. In particular, nanostructured targets present different nanowires parameters, i.e. various metal (Co, Fe, Ni and Ag), different geometries (length and diameter of nanowires),techniques of deposition and confinement.

The optimization of the specific characteristics of nanomaterials, containing metal nanowires, could lead to a stagnant, hotter and denser plasma and to implement the above mentioned studies successfully. In fact, while in an typical bulk target, the laser energy is absorbed in a very thin (hundred of nm) layer at the target surface, nanostructured targets can absorb more electromagnetic energy and transport it deeper inside the material, forming a plasma which is expected at higher density and temperature.

The work presented in this thesis covers the experimental results on the plasma produced with moderately high power laser of about 4×10^{12} W/cm^2. The characterization of laser-produced plasma from nanostructured compared with Al-Bulk target has been carried out. The fundamental frequency (1064 nm) from a Q-switched Nd:YAG laser with 6 ns pulse duration is used for the present studies. Various diagnostics were employed for the characterization of the Laser Produced Plasma (LPP), which include optical imaging, X-ray emission studies, and Time of Flight (ToF) measurements.

Moreover, morphological analysis of craters formed for the laser irradiation was performed.

Finally, preliminary ions energy distributions with a Thomson Parabola Spectrometer were carried out in order to verify the effectiveness of nuclear reaction rates measurements.

The work is organized as briefly outlined below.

Chapter 1 gives a brief introduction of the most useful concepts and definitions for nuclear reactions studies in astrophysics environment. Moreover, an overview of the relevant aspects of laser interaction with solids and the various phenomena taking place inside the plasma are reviewed.

The main atomic processes and plasma equilibrium models employed to describe laser produced plasmas are presented in the Chapter 2.

Chapter 3 gives the description of the experimental apparatus: the plasma chamber and experimental setups for the various plasma diagnostic techniques are summarized. The samples preparation technique and the features of nanostructures are also investigated.

Chapter 4 presents the study of the dynamics of laser-produced plasmas from nanostructured and ordinary bulk targets.

Chapter 1

Laser-produced plasmas

Laser Produced Plasmas are of great interest for Nuclear Astrophysics. Therefore, in this chapter an overview of the state-of-the art of nuclear reactions studies in astrophysics environment and issues related to the determination of the cross sections at energies of astrophysical interest will be given. Then, a description of the fundamental proprieties of plasma in general and the basic physics of a nanosecond laser generated plasma will be presented.

1.1. Physics case: Thermonuclear Reactions

Performing accurate measurements of nuclear reaction rates of proton and alpha burning processes is essential for the correct understanding of many astrophysical processes, such as stellar evolutions, supernova explosions, Big Bang nucleosynthesis, etc. Direct and indirect measurements of the relevant cross sections have been performed over the years. Direct measurements using accelerated beams show that, at very low energies, the electrons in the target's atoms partially screen the Coulomb barrier between the projectile and the target, resulting in an enhancement of the measured cross section compared with the bare nucleus cross section. Therefore, electron screening prevents a direct measurement of the bare nucleus cross section at the energies of astrophysical interest. In the last decade, the bare cross section has been successfully measured in certain cases by using several indirect methods.

However, measurements of cross-sections at extremely low energetic domains including plasmas effect, i.e. in an environment that under some circumstances and assumptions can be considered as "stellar-like", is of relevant importance.

Thermonuclear reactions play a main role in understanding energy production and nucleosynthesis of the elements in stars. It is possible to describe astrophysics environments by means of energy, density or temperature, which follow Maxwell-Boltzmann energy distribution. Particles in stars interact by means of their thermal mean energy, which is of the order of few keV. This energy is lower than the values of the Coulomb barrier height between the interacting species, typically of the order of a few MeV. Therefore, the reactions proceed, according to quantum mechanics, through the tunnel effect, which strongly reduces their cross section to values of the order of a few 10^{-9} - 10^{-12} barn, thus making it difficult to realize the study in terrestrial laboratories.

In the following, we define the physical parameters useful to understanding the astrophysical nuclear processes.

1.1.1. Coulomb barrier and penetration factor

In stars, nuclear reactions take place between charged particles because the atoms are in most cases completely stripped of their atomic electrons. It is assumed that they are almost completely ionized because of the typical high temperature conditions (around a few keV at least). This high temperature is on the other hand needed to permit the reactions, because nuclei are positively charged and repel each other with a Coulomb force proportional to their nuclear charge. Nuclear reaction between charged particles at such low energies are strongly suppressed by the presence of the Coulomb barrier, whose height is given by:

$$E_C = \frac{Z_1 Z_2 e^2}{R_n} \qquad (1.1.1)$$

Where Z_1 and Z_2 are the atomic number of the two incident nuclei and R_n is the nuclear interaction radius.

Fig. 1.1.1 represents the schematic view of the effective potential resulting when one combines the very strong and attractive nuclear potential with the electromagnetic potential.

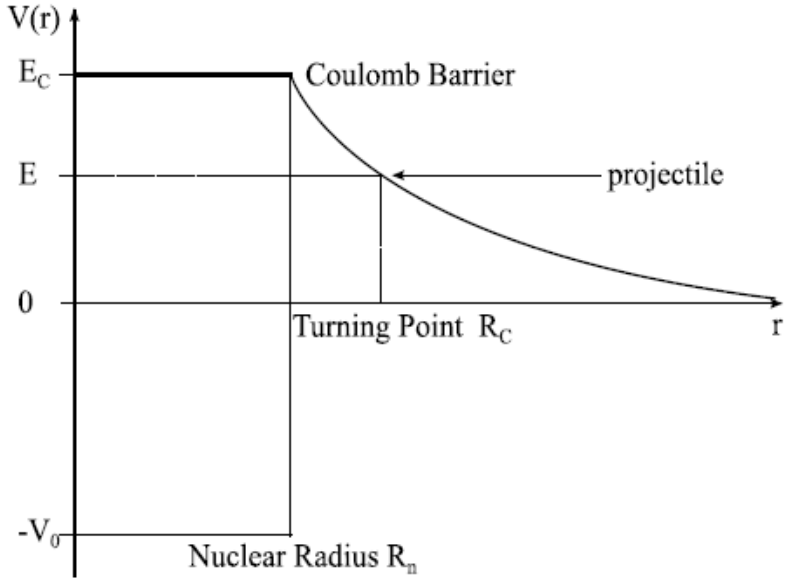

Fig. 1.1.1 – Schematic representation of the combined nuclear and Coulomb potentials.

Consequently, if this is the case, the fractions of particles whose energies exceeds the Coulomb barrier is negligible and it seems necessary a higher stellar temperature. This obstacle was removed when Gamow showed that, in according to the quantum mechanics, there is a small but finite probability for the particles with energies $E < E_C$ to penetrate the barrier even if its energy is lower than the barrier's height.

It is possible to define the penetration factor through the Coulomb barrier as [1]:

$$T_l = \frac{|\chi(R_n)|^2}{|\chi(R_C)|^2} \qquad (1.1.2)$$

where R_C is the classical turning point and $\chi(r)$ is the radial wave function. It can be calculated by solving the radial part of the Schrödinger equation:

$$\frac{d^2\chi_l}{dr^2} + \frac{2\mu}{\hbar^2}[E - V_l(r)] = 0 \qquad (1.1.3)$$

where $V_l(r)$ is the potential for the l^{th} partial wave.

At low energies or, equivalently, where the classical turning point is much larger than the nuclear radius, equation (1.1.2) can be approximated by the simpler expression giving the so-called Gamow factor:

$$T = e^{-2\pi\eta} \qquad (1.1.4)$$

where $\eta = Z_1 Z_2 e^2/\hbar v$ is the Sommerfeld parameter, which depend only on the relative velocity of the two interacting particles and their charges.

1.1.2. Cross section and astrophysical factor

Since nuclear reactions are governed by the laws of quantum mechanics, the cross section must be described by the energy-depend quantity:

$$\sigma = \pi\lambda_B^2 \frac{1}{E} \qquad (1.1.5)$$

where λ_B represents the De Broglie wavelength.

For charged-particle nuclear reaction the cross section is strongly suppressed by Coulomb and centrifugal barriers and it drops rapidly for $E < E_C$. It is possible to factorize the cross section as:

$$\sigma = \frac{1}{E} S(E) e^{-2\pi\eta} \qquad (1.1.6)$$

where *S(E)* is the so-called astrophysical factor and contains all nuclear effects. The astrophysical factor is a much more useful quantity because for non-resonant reactions it is a smoothly varying function of energy.

Fig. 1.1.2 shows that *S(E)* varies much less rapidly with beam energy than the cross section and it allows an easier procedure for extrapolating the energy behaviour at astrophysical energies.

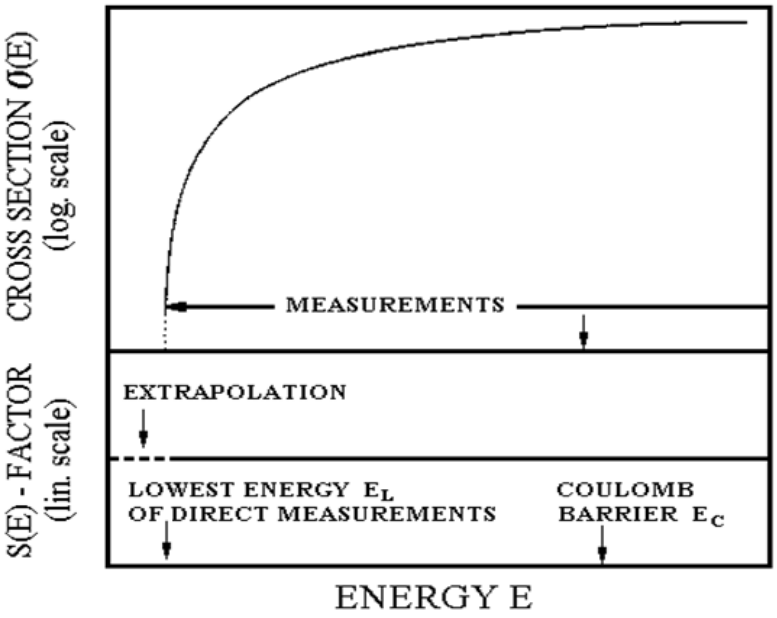

Fig. 1.1.2 – Comparison between the energy behavior for cross section and astrophysical factor. While the cross section has a dramatical energy-dependence, the astrophysical factor is practically constant.

1.1.3. Reaction rate and Gamow Peak

It is important to introduce another quantity, the so-called reaction rate, to describe the nuclear process in astrophysical scenarios. The reaction rate is defined as the number of reaction per unit volume and per unit time and it is written in terms of cross section as:

$$r = \frac{1}{1+\delta_{xA}} N_x N_A \langle \sigma(v) v \rangle \qquad (1.1.7)$$

where N_x and N_A represent the number of projectile and target nuclei respectively. For identical particles the Kronecker symbol δ_{xA} is introduced, otherwise each pair would be counted twice. The bracketed quantity $<\sigma(v)v>$ is referred to as the reaction rate per particles pair and it is the mean of the product over all the possible energies, weighted over the Maxwell-Boltzmann distribution:

$$r = \frac{1}{1+\delta_{xA}} N_x N_A \int_0^\infty v\sigma(v)\phi(v)dv \qquad (1.1.8)$$

By introducing the center of mass energy $E\ \frac{1}{2}\mu v^2$ with μ representing the reduced mass of interacting particles, the reaction rate is then expressed as:

$$r = \frac{1}{1+\delta_{xA}} N_x N_A \sqrt{\frac{8}{\pi\mu}} \frac{1}{\sqrt{(k_B T)^3}} \int_0^\infty \sigma(E) E exp\left(-\frac{E}{k_B T}\right) dE \qquad (1.1.9)$$

By introducing equation (1.1.6) into equation (1.1.9), one obtains:

$$\langle \sigma v \rangle = \sqrt{\frac{8}{\pi\mu}} \frac{1}{\sqrt{(k_B T)^3}} \int_0^\infty S(E) exp\left(-\frac{E}{k_B T} - \left(\frac{E_G}{E}\right)^{1/2}\right) dE \qquad (1.1.10)$$

where E_G is the so-called Gamow energy. The integrand, because of the limited dependence of $S(E)$ from E, is governed by the combination of two exponential terms: the first represents the Maxwell-Boltzmann distribution and the second one is the probability of tunneling through the Coulomb barrier. The maximum of the integrand is reached at an energy E_0:

$$E_0 = \left(\frac{k_B T}{2}\right)^{3/2} {E_G}^{1/2} \qquad (1.1.11)$$

The convolution of the two functions results into a peak, the so-called Gamow peak, centered near the energy E_0 and generally much larger than k_BT.

As it can see from Fig. 1.1.3 the Gamow peak has an effective width Δ, which is referred as Gamow window, wherein most of reactions take place:

$$\Delta = \frac{4}{\sqrt{3}}\sqrt{E_0 k_B T} \qquad (1.1.12)$$

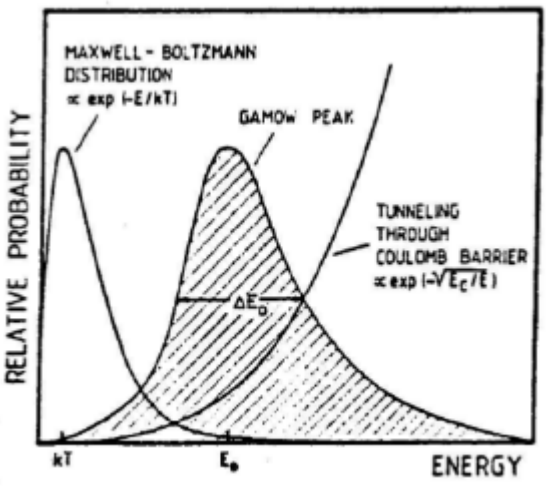

Fig. 1.1.3 – The Gamow peak is the result of the convolution of two functions: the Maxwell-Boltzmann distribution and the quantum mechanical tunneling function through the Coulomb barrier. The energetic region relevant for the astrophysical investigation (the zone with gray lines) is around the value E_0.

Usually the effective energy for thermonuclear reactions ranges from few keV to about a hundred keV depending on both the reaction and the astrophysical site in which the reaction occurs. However, the nuclear processes of astrophysical interest occur at energies that in general are too low for direct measurement in laboratory. These difficulties are related to different problems and usually the standard solution is to measure the cross section or, equivalently, the S-factor over a wide range of energies and to the

lowest energies possible and then to extrapolate the data downward to E_0 with the help of theoretical arguments and other methods.

1.1.4. The electron screening effect

A relevant source of uncertainty in the extrapolation of the astrophysical factor down to zero energy is the enhancement of *S(E)* due to the electron screening effect. Up to now, it was assumed that the interacting nuclei be completely stripped of electrons, so the Coulomb potential is typically expressed as in equation (1.1.1), being essentially bare nuclei. On the contrary, when nuclear reactions are studied in a laboratory, the projectile is usually in the form of an ion and the target is usually a neutral atom or molecule surrounded by their electronic cloud [2]. The atomic electron cloud surrounding the nucleus acts as a screening potential and consequently the total potential goes to zero outside the atomic radius (R_a):

$$V_{eff} = \frac{Z_1 Z_2 e^2}{R_n} - \frac{Z_1 Z_2 e^2}{R_a} \qquad (1.1.13)$$

Then the projectile effectively sees a reduced Coulomb barrier. As a consequence, at low energies the cross section for screened nuclei, $\sigma_s(E)$, is enhanced, with respect to the cross section of the bare nucleus $\sigma_b(E)$, by a factor:

$$f(E) = \frac{\sigma_s}{\sigma_b} \propto exp\left(\pi\eta \frac{U_e}{E}\right) \qquad (1.1.14)$$

where U_e, representing the screening potential for the studied reaction, must be taken into account to determine the bare nucleus cross section. Because of the high temperature of stars, atoms are generally completely ionized, and one can imagine that electron screening has no effect on nuclear reactions in stars. However, nuclei are immersed in a sea of free electrons, the so-called plasma, resulting in an effect similar to the one discussed above.

The shielding effect reduces the Coulomb potential as in laboratory and it increases the reaction rate, or equivalently the cross section, by a factor *g(E)* according to the equation:

$$\langle \sigma v \rangle_s = g(E) \langle \sigma v \rangle_b \qquad (1.1.15)$$

It is necessary to know the electron screening factor in the laboratory in order to extract the bare nucleus cross section from the $\sigma_s(E)$.Then the proper stellar screening factor should be applied to that (1.1.15). One of the most important uncertainties in experimental nuclear astrophysics derives from this procedure and, because of this, more exhaustive and precise determinations of σ_b are needed at energies as low as possible.

1.2. Introduction to laser-produced plasmas

When a pulsed laser beam is focused onto a solid target a plasma is rapidly created from a thin surface layer of the target, provided the intensity of the beam on the target is sufficiently high (over $10^{10} \div 10^{12}$ W/cm^2). The physical processes through which the initial ionization takes place starting from the cold, solid-state material, strongly depend upon the intensity and the temporal profile of the laser beam [3].

LPPs have more than 50 years of research history. The study of ablation plumes by photography was initiated by Ready [4] in 1963, employing millisecond lasers pulse length.

Later, Basov and Krokhin [5] made the first suggestion of laser fusion, and as higher power lasers were used, vacuum ultraviolet [6] and X-ray emissions [7] were detected. Higher power also led to the observation of multiply charged ions [8] and to two- [9] and three-photon [10] photoemission. Measurable neutron fluxes from laser-heated targets were first reported in 1968 [11].

Finally, of great importance in terms of modern applications of ablation, the first laser deposition of thin films was demonstrated by Smith and Turner [12] in 1965, employing LPP on a wide range of solids targets with several types of lasers (Ruby, Neodynium and Carbon Dioxide Lasers).

To generate a plasma the irradiance must be about $\geq 10^7$ W/cm^2 with a pulse duration of 0.5 ms [3]. Nanosecond Lasers Pulses (6 – 9 ns) have been introduced with Q-switched Ruby lasers invention, in the 60′ s. This immediately leads to raise the available laser irradiance to become on the order of $10^9 - 10^{13}$ W/cm^2; ions emission having different charge states with energies up to some keV′ s is then obtained [3].

The development of more powerful lasers and with very short pulse widths leads to even more complicated laser-matter interactions (nanosecond lasers can easily generate 10 ps pulses with $10^{16} - 10^{18}$ W/cm^2 of output power, introducing in this way the use of Picosecond Lasers pulses). In this case, the produced plasma is characterized by relativistic electron oscillations in the intense electromagnetic field of the laser light wave, and electron-phonon interactions must be taken into account. Significant influence of the ponderomotive force is also expected [13]. Today picosecond lasers have been mostly substituted by Femtosecond Laser pulses, which reach power densities higher than 10^{18} W/cm^2. In this regime the plasma is strongly influenced by nonlinear ponderomotive forces acting on the plasma; this mechanism is described by weak plasma oscillations. LPP by Femtosecond laser are mostly employed for ion acceleration [14].

1.2.1. Basic plasma parameters

Plasma conditions span a very wide range of temperatures and densities, as demonstrates in Fig. 1.2.1. For example, whereas the interstellar gas contains only a few particles/cm^3, white dwarfs have of the order of 10^{30}

particles/cm^3. Similarly the temperatures range from room temperatures in non-neutral electron plasmas to 10^8 K in plasmas in magnetic fusion experiments.

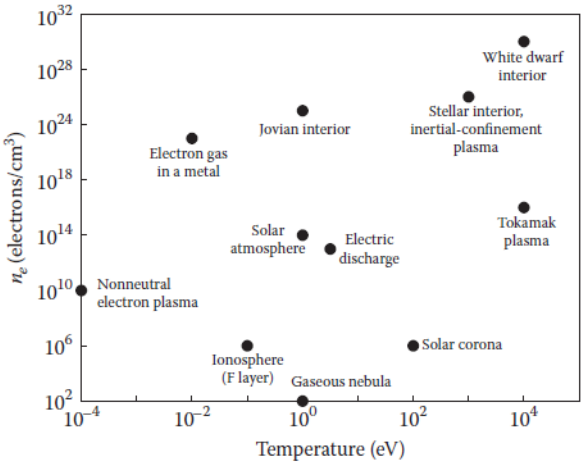

Fig. 1.2.1– Different kinds of plasmas as a function of temperature and density [15].

All these different types of plasma share a common definition: a plasma is a collection of ionized matter that admits quasi-neutrality and exhibits collective behavior [16]. The term quasi-neutrality implies ionized assembly is neutral enough so that the electron and ion charge densities are approximately equal over a large scale. Collective behaviour implies existence of long ranged electromagnetic force in a large collection of charged particles. Then the motion depends not only on local conditions, but on state of plasma in remote regions as well [17].

The basic parameter that characterizes the plasma behavior is the so-called Debye length λ_D, defined by [18]:

$$\lambda_D = \sqrt{\frac{\varepsilon_0 k_B T_e}{e^2 n_e}} \qquad (1.2.1)$$

where ε_0 is the permittivity of free space, k_B is the Boltzmann constant, T_e is the plasma temperature (in eV), e is the electron charge and n_e is the electron density (in m^{-3}).

An extension of the Debye length is the Debye sphere, i.e. the sphere with a radius equal to the Debye length, outside which the electric field of the enclosed charge is zero (fully shielded). The number of electrons, N_D, inside the Debye sphere is then given by [19]:

$$N_D = \frac{4}{3}\pi\lambda_D^3 n_e \qquad (1.2.2)$$

The conditions for the existence of a collective behavior are that $\lambda_D >> L$, where L is the length of the plasma, and that the number of particles in the Debye sphere is very high, i.e. $N_D >> 1$.

The collective response of the plasma manifests itself as a wave–like motion of the particles within the plasma. If by some mechanism the electrons are displaced by a small distance, the electrons will tend to move back to their equilibrium positions. The equation of motion of the electrons is found to have an oscillatory solution corresponding to the collective motion of the electrons. This so called electron wave oscillates with a frequency, ω_p, given by:

$$\omega_p = \sqrt{\frac{n_e e^2}{m_e \varepsilon_0}} \qquad (1.2.3)$$

This plasma frequency plays an important role in almost all plasma processes.

1.3. Absorption mechanisms

When a laser pulse is incident on a material, the first question that arises is how this laser energy is coupled to the material or plasma so formed. The

absorption of laser light in plasma is rather complex and many different processes take place simultaneously [20-22]. The most instinctive mechanism for the dissipation of laser energy is via collision between electrons and ions. This mechanism is more dominant in case of long duration pulses or very high-density plasmas. Significant absorption is, however, possible even in collisionless or weakly collisional plasmas.

1.3.1. Waves in plasma

An important property of plasmas is their ability to transmit collective waves, which in the simplest case are just fluctuations in the electron or ion density. In the following, the different types of waves will be investigated.

The linear dispersion relationship for an electromagnetic wave in a plasma with a uniform density is influenced by the presence of the free electrons and is given by:

$$\omega^2 = \omega_p^2 + k^2 c^2 \qquad (1.3.1)$$

where ω_p is the electron plasma frequency (1.2.3). This relation implies that an electromagnetic wave at frequency ω_L can propagate inside the plasma only in regions where $\omega_L > \omega_p$, that can also be expressed as function of the critical density n_{cr}:

$$n_e < n_{cr} = \frac{4\pi^2 c^2 m_e \varepsilon_0}{e^2 \lambda_L^2} \approx \frac{1.1 \times 10^{21}}{(\lambda_L(\mu m))^2} cm^{-3} \qquad (1.3.2)$$

Thus, inside a plasma electromagnetic wave can only propagate in the under-dense region and reflected back from the critical density.

A plasma can support the propagation of longitudinal waves, consisting in oscillations of the charge density. Due to the difference in mass between electrons and ions, their respective oscillations have a quite different behavior. The electron density longitudinal oscillations, called Langmuir waves, fulfills the dispersion relation given by:

$$\omega^2 = \omega_p^2 + 3k_B^2 v_{th}^2 \qquad (1.3.3)$$

Due to their inertia, the ions can be regarded, on the time scales involved in this oscillations, at rest, so that only the electrons motion have to be considered in a periodic fluctuations of the charge in the plasma.

The longitudinal waves at lower frequency, the so-called ion-acoustic waves, involve the periodic fluctuation of the ion density, with the electrons closely following the ion motion so as to preserve the charge neutrality. The dispersion relation is:

$$\omega^2 = k^2 \frac{Z k_B T_e + 3 k_B T_i}{m_i} \qquad (1.3.4)$$

where Z is the atomic number, T_e and T_i are the electron and ion temperature and m_i is the ion mass.

It should be noted that Langmuir waves and ion acoustic waves are longitudinal waves, whereas electromagnetic waves are of transversal character.

The detailed derivation of these dispersion relations is reported in [23].

1.3.2. Inverse Bremsstrahlung absorption

Inverse bremsstrahlung absorption is an essential mechanism for coupling laser energy to the plasma. Laser light is absorbed near the critical surface via this mechanism. In particular, the electrical field induced by the laser the causes electrons in the plasma to oscillate. This oscillation energy is converted into thermal energy via electron-ion collisions.

The electron-ion collision frequency for a Maxwellian distribution of the electrons can be written as [19]:

$$\nu_{ei} = \left(\frac{2\pi}{m_e}\right)^{1/2} \frac{4Z^2 e^4 n_i}{3(k_B T_e)^{3/2}} \ln \Lambda \qquad (1.3.5)$$

where $ln\Lambda$ is the so-called Coulomb logarithm for the electron-ion collision. The absorption coefficient of the laser wave due to this mechanism can be written as:

$$k_{ib} = \frac{\nu_{ei}}{c}\frac{\omega_p^2}{\omega_L^2}\left(1 - \frac{\omega_p^2}{\omega_L^2}\right)^{-1/2} \qquad (1.3.6)$$

and substituting the expression for the collision frequency (1.3.5), one obtains:

$$k_{ib} \sim \frac{Z}{T_e^{3/2}}\frac{n_e^2}{\omega_L^2}\left(1 - \frac{\omega_p^2}{\omega_L^2}\right)^{-1/2} \qquad (1.3.7)$$

This expression shows that inverse Bremsstrahlung is most efficient in high density and low temperature regions. The fraction of laser energy absorbed through this mechanism during the propagation up to the critical density depends on the electron density profile, temperature and the Coulomb logarithm. The difficult is that all these values are time-dependent. However, for laser pulses of 1 ns duration or longer with intermediate intensities ($<10^{14}$ W/cm^2), the electron temperature and Coulomb logarithm can be assumed to constant. Therefore, for a linear density profile, Ginzburg [16] showed that the analytical solution for the absorption coefficient is given by:

$$\alpha_{ib} = 1 - exp\left[-\frac{32}{15}\frac{\nu_{ei}(n_c)l}{c}\right] \qquad (1.3.8)$$

and Kruer [23] demonstrated that for an exponential profile one obtains:

$$\alpha_{ib} = 1 - exp\left[-\frac{8}{3}\frac{\nu_{ei}(n_c)l}{c}\right] \qquad (1.3.9)$$

where l is the propagation distance.

Although inverse bremsstrahlung is an important absorption process in plasmas, it is not the only one. Inverse bremsstrahlung absorption is only efficient if enough collisions take place. However, from Eq. (1.3.5) it follows that the collision frequency ν_{ei} scales as $T_e^{-3/2}$. This means for higher temperatures inverse bremsstrahlung becomes less and less effective. This effect has been verified in many experiments in which the absorption coefficient for a low-Z solid like aluminum was measured for different laser input energies [19]. Fig. 1.3.1 shows the different behavior between the long pulse duration (of the order of 1 ns) for different laser wavelength (1 μm, 1/2 μm, 1/3 μm, 1/4 μm) and short laser pulses (of about 100 fs) with a wavelength of 0.8 μm.

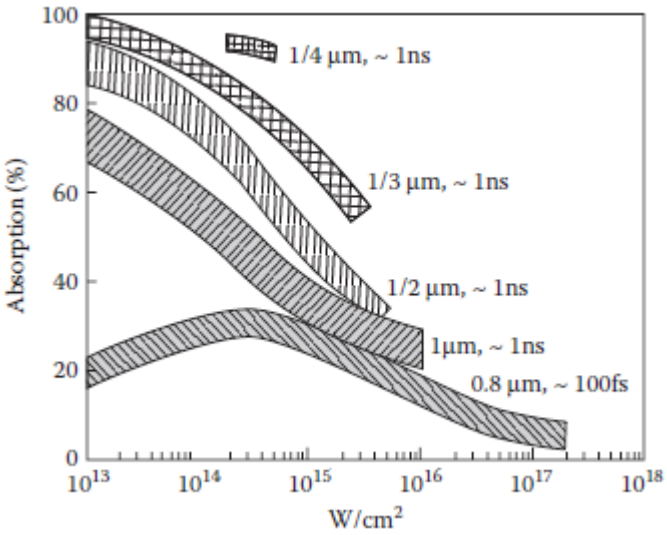

Fig. 1.3.1 – Experimental data of the laser absorption in solid low-Z targets [19].

However there are other processes that couple the energy of the laser light at higher laser intensities into the plasma; in particular, resonance absorption and parametric instabilities, which we consider in the following two sections.

1.3.3. Resonance absorption

Inverse Bremsstrahlung becomes inefficient in a hot plasma due to the rapid decrease of the electron-ion collision frequency with temperature. Collective effects in the plasma then determine the absorption of laser light.

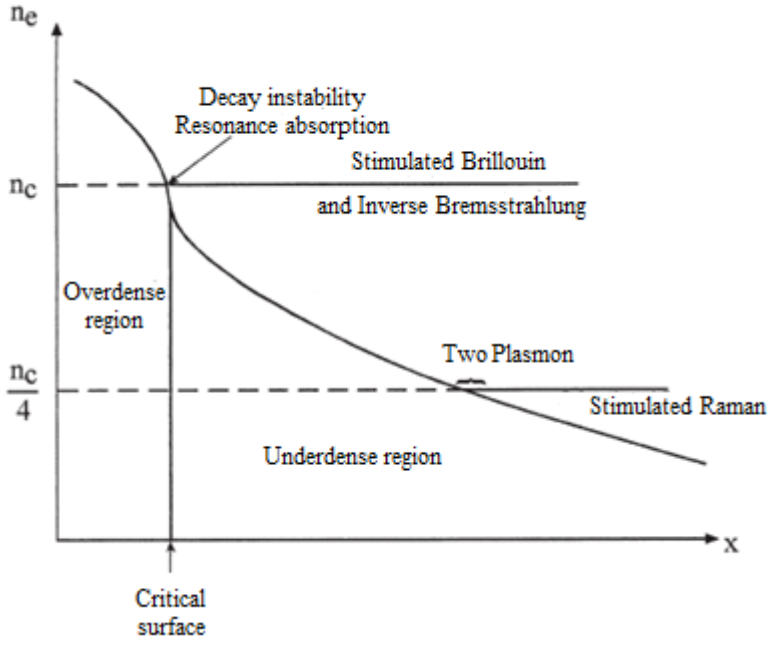

Fig. 1.3.2 – Possible absorption mechanisms and the domain of wave – wave interactions along the density profile.

As illustrated in Fig. 1.3.2, the plasma that is created by the interaction of the laser with a solid target has an inhomogeneous density profile comprising both underdense and overdense regions. Whenever light meets a plasma with these characteristics, electrostatic waves are excited if any component of the electric field of the light coincides with the direction of the density gradient (p-polarized interaction). Light absorption via collective processes occurs most efficiently for densities near the critical density n_c, where the local electron plasma frequency ω_p equals the radiation frequency ω_L. In this case, the electric field becomes very large near the critical surface, and it is here

that waves are resonantly excited. In this way, energy is transfered from the electromagnetic into plasma waves. Because these waves are damped, energy will eventually be converted into thermal energy, thus heating the plasma. In [16, 24-26] a model description for resonance absorption is reported.

The resonance absorption can dominate over inverse bremsstrahlung absorption for high plasma temperatures, low critical densities, and short plasma scale-length.

The main feature of the this mechanism is the creation of hot electrons, since only a minority of the plasma electrons acquires most of the absorbed energy in contrast to collision absorption (inverse bremsstrahlung), which heats all of the electrons.

1.3.4. Parametric instabilities

As already mentioned, a hot plasma supports the excitation of waves. Waves can enhance absorption, which would be a desirable effect, but can also reduce the absorption of the laser light. Here, we briefly report the main conclusions relative to the most important instabilities occurring in laser-plasma interactions, with particular attention to matching conditions and laser intensity thresholds.

The energy and momentum conservation in the wave–wave interaction is described by the following equations:

$$\omega_0 = \omega_1 + \omega_2 \qquad \boldsymbol{k}_0 = \boldsymbol{k}_1 + \boldsymbol{k}_2 \tag{1.3.10}$$

where ω_0 and $\boldsymbol{k}_0$ are the frequency and wave number of the pumping laser field that decays into two waves (ω_1, $\boldsymbol{k}_1$) and (ω_2, $\boldsymbol{k}_2$). Using these conservation laws and the dispersion relations (1.3.1), (1.3.3) and (1.3.4), the wave–wave interactions are induced in the following domain.

Stimulated Brillouin Scattering (SBS)

A laser pump with frequency $\omega_L >> \omega_p$ may decay into a photon and an acoustic wave, resulting in backscattering and thus reduced laser absorption. SBS contains a low-energy ion wave that takes only a small fraction of the laser energy, while the rest of the energy can be scattered out of the plasma. The instability occurs at $n_e < n_{cr}$.

In general, SBS can cause large rejection of the incident laser radiation leading to a strong reduction of plasma heating. The threshold intensity of the SBS instability in terms of the electron density scalelength L (μ m), the plasma electron temperature T_e(eV), and the laser light wavelength λ_L (μ m), is [27]:

$$I_{SBS} = 7 \times 10^{12} \frac{T_e}{L\lambda_L} \frac{n_{cr}}{n_e} \, W/cm^2 \qquad (1.3.11)$$

Stimulated Raman Scattering (SRS)

A laser pump with frequency $\omega_L > 2\omega_p$ may decay into a photon and a plasmon, leading to laser scattering, including backscattering. This instability reduces the laser absorption and occurs at $n_e << ¼\, n_{cr}$.

Again, in the case of inhomogeneous plasma and in the limit of $n_e << ¼\, n_{cr}$, the (back-scattering) threshold intensity is [27]:

$$I_{SRS} = \frac{4 \times 10^{17}}{L\lambda_L} W/cm^2 \qquad (1.3.12)$$

We observe that, in contrast with the SBS threshold, the SRS threshold does not depend upon the electron temperature. This equation holds provided that the electron density is sufficiently small compared to the upper limit density at which the instability can occur.

Two-Plasmon Decay (TPD)

A laser pump with frequency $\omega_L \approx 2\omega_p$ may decay into two plasmons, inducing laser absorption. This phenomenon happens at an electron density $n_e \approx$ ¼ n_{cr}.

The inhomogeneous threshold intensity is given by [27]:

$$I_{TPD} = 5 \times 10^{12} \frac{T_e}{L_{1/4}\lambda_L} \, W/cm^2 \qquad (1.3.13)$$

where $L_{1/4}$ (μ m) is the electron density scalelength at $n_e \approx$ ¼ n_{cr}. A signature of the occurrence of two plasmon decay in laser plasma interaction experiments is the production of electromagnetic radiation at a frequency corresponding to half-integer harmonics of the incident laser light, and in particular at the three-half harmonic.

1.3.5. Plasmonic resonance

In order to enhance the laser–plasma coupling, in the last years, large efforts were dedicated to testing nanostructured targets. Evidences of a larger absorptivity of laser radiation and of an enhancement of X-ray emission, higher than that obtained by standard flat targets [28-36], and of a higher amount and temperature of the hot electrons generated [29, 37-40] has been obtained for nanostructured targets. The mechanisms able to produce an enhancement of the absorptivity of a nanostructured, depending on the geometry and dimensions of the structures, are related to the enhancement of the local electric field due to the presence of plasmonic resonances in the absorption spectrum [41-45].

Plasmons are collective electron excitations formed on the surface of metals, caused by electromagnetic radiation. Due to plasmonic excitations, a metal nanowire exposed to electromagnetic radiation acts as a waveguide, despite being much smaller than the incident wavelength: photons can be

absorbed at one end of the nanowire, transported through its length as an electrical impulse, and re-emitted as photons (with some loss in intensity) at the opposite end [46].

Plasmons, which can be treated as quasi-particles, propagate with specific wavelength and polarization, and nanowires have their own resonant frequency, which is strongly dependent on geometrical characteristics of the nanostructures. Therefore, photon-plasmon coupling is dependent on wavelength, and nanostructures' parameters can be tuned - at least in principle - to absorb specific wavelengths [46].

Light absorption of nanowires depend on incidence angle, favoring absorption along the nanowires (NWs) axis. This is favorable for our applications, since alumina pores (and thus nanowires grown in them) are normal to the surface, and will transport light deep inside the material. The specific absorption spectrum of nanowires depend on a great number of parameters, such as geometry, NWs metal and surrounding material (NWs freed from alumina have a remarkably different behavior) [47].

Many experiments were performed by irradiating a nanowire target with an ultra-short pulse and an interesting effect is the capability of plasmonic effect to transfer energy delivered by laser beam from the surface to the interior of a target. This allows volumetric instead of superficial heating of matter, which is of great interest for dense plasma formation [48].

Chapter 2

Atomic processes and Equilibria models in Plasmas

The key atomic processes prevalent in laser-produced plasmas will be summarized along with the main plasma expansion and plasma equilibrium models employed to describe laser produced plasmas.

2.1. Atomic Processes in plasma

In a plasma, atoms and ions undergo transitions between their quantum states through radiative and collisional processes. Among these processes, the most important are spontaneous radiative transitions and collisional transitions induced by electron impact (collisions) [49]. In the following, we review this processes.

2.1.1. Collisional processes

In LPP electron-neutral collision are important for excitation and de-excitation processes of plasma particles and are related to emission of radiation. Ionization processes have a primary role in the early stage of the plasma formation, when the temperatures are very high and high charge states can be produced. Moreover, electron-ion collisions limit electron thermal conduction, which then affects the cooling rate of the plume during it's expansion. Binary collision are essentially due to two different type of atomic processes, called Bound-Bound transitions (B-B) and Free-Bound

transitions (F-B). The firsts occur when an electron occupying a discrete energy level in an atom or ion, is promoted or demoted to another discrete energy level during a collision with another electron or by emission (or absorption) of a photon. Bound-Free processes occur when an ion receives enough energy to eject one of its bounded electrons into the continuum, thereby incrementing its ionization state by one, or an electron in the continuum loses energy and falls into a discrete energy level of an ion thereby reducing its ionization state by one. These processes are hence classified in:

Electron Impact Excitation and De-excitation

Electron Impact Excitation occurs when some or all of the kinetic energy of a free electron is transferred to a bound electron exciting it to a higher energy level [50]. The energy gained by the bound electron is equal to the energy lost by the free electron.

Conversely, Electron Impact De-excitation occurs when a bound electron in an excited state loses energy and is demoted to a state of lower energy upon collision of the host atom or ion with (usually) a free electron. The kinetic energy of the free electron will be increased by the same amount or quantum of energy that lost by the bound electron in the collision.

The balance equations for these processes is given by:

$$A + e(\varepsilon_1) \Leftrightarrow A^* + e(\varepsilon_2) \qquad (2.1.1)$$

where A represents the atom/ion in a lower energy state, A* denotes the atom/ion in an excited state, and ε_1 and ε_2 denote the free electron kinetic energies before and after the collision respectively. If equation (2.1.1) is read from the left-hand side to the right-hand side, it describes the process of electron-impact excitation, vice-versa it describes the process of electron-

impact excitation for electron-impact de-excitation. Fig. 2.1.1 shows schematically the atomic processes described above.

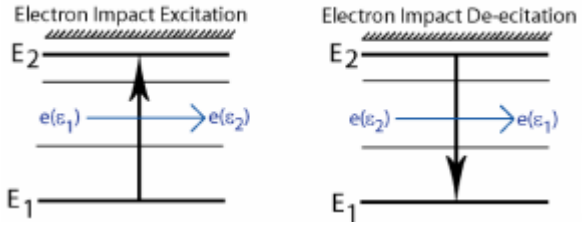

Fig. 2.1.1 – Schematic diagram of the electron impact excitation (left) and electron impact de-excitation (right) atomic processes which occur in laser produced plasmas [50].

Electron Impact Ionization and Recombination

When a free electron collides with an atom or ion, enough energy may be transferred from the free electron to a bound electron to overcome the ionization potential of the atom/ion. The bound electron will then be ionized and enter the free electron continuum. The energy gained by the bound electron is equal to the energy lost by the free electron. This process is known as electron impact ionization [13] and is described by:

$$A^z + e_1 \Leftrightarrow A^{z+1} + e_1' + e_2 \qquad (2.1.2)$$

where A^{z+1} is an ion in charged state $z+1$, A^z is the ion of charge state z, e_1 and e_1' are the free electron before and after (lower energy) the collision and e_2 is the bound electron. This process is predominant in low density plasmas.

The inverse of this process is known as 3-body recombination and usually occurs in high density plasmas where the probability of two electrons entering the Debye sphere of an ion becomes relatively high. In 3-body recombination, one free electron is captured into an outer level of an ion. The second electron gains the energy lost by the captured electron. The balance equation for 3-body recombination is given by:

$$A^{z+1} + e_1(\varepsilon_1) + e_2(\varepsilon_2) \Leftrightarrow A^z + e_1(\varepsilon_1') \qquad (2.1.3)$$

where $e_1(\varepsilon_1)$ and $e_2(\varepsilon_2)$ are the free electrons before the interaction and $e_1(\varepsilon'_1)$ is a free electron with increased energy after the capture of the other free electron by the ion. Fig. 2.1.2 illustrates these processes graphically.

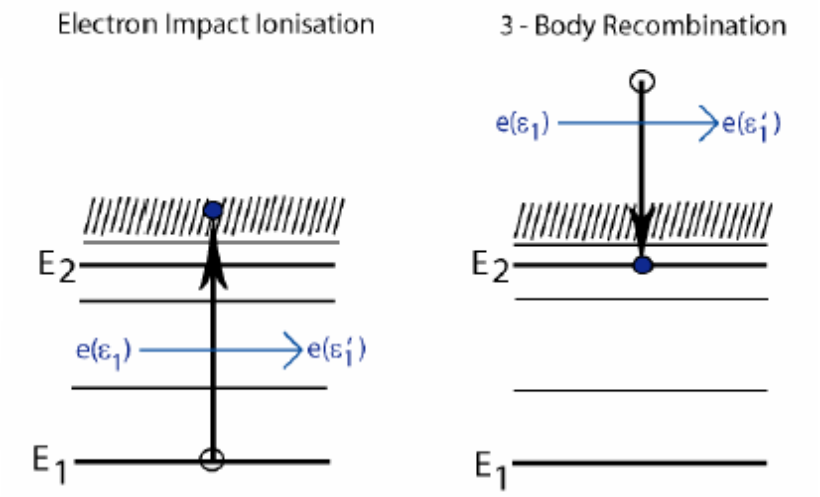

Fig. 2.1.2 - Schematic diagram illustrating the electron impact ionization (left) and 3-body recombination (right) atomic processes that occur in laser produced plasmas [50].

2.1.2. Radiative processes

Radiation processes are of fundamental importance in LPP, because the emission of radiation is related to line emission spectra and hence to the evaluation of the plasma temperature and the plasma density. Moreover, the inverse process, i.e. absorption of photons, includes the understanding of plasma ignition through the interaction with the laser photons.

Atomic radiative processes are generated from Bound-Bound transitions, Free-Bound transitions and Free- Free transitions.

Spontaneous Decay and Resonant Photoabsorption

Spontaneous Decay occurs when an electron drops from an excited state to one with lower energy releasing a photon in the process. The energy of the

liberated photon is equal to the energy difference of the electron before and after the transition. This process can be described by the formula:

$$A^* \rightarrow A + \gamma \qquad (2.1.4)$$

where A^* denotes the atom/ion in an excited state, A represents the atom/ion in a lower energy state and γ represents the photon released during the transition.

Conversely, photoabsorption occurs when a photon is absorbed by an electron in a low energy state that is consequently promoted to a state of higher energy. In this case, the energy difference of the electron before and after its transition is equal to the photon absorbed energy. This process can be described by the formula:

$$A + \gamma \rightarrow A^* \qquad (2.1.5)$$

The two processes are reported in Fig. 2.1.3.

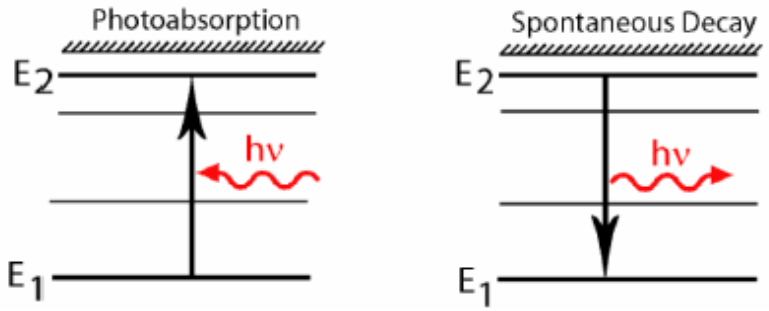

Fig. 2.1.3 – Schematic illustration of the photoabsorption (left) and spontaneous decay (right) atomic processes which occur in laser produced plasmas. E_1 and E_2 are lower and upper electron energy states of the atom/ion respectively [50].

Radiative Recombination and Photoionization

Radiative Recombination occurs when a free electron is in the vicinity of an ion, it can be captured by the ion and consequently recombine with the atom. During the process a photon is released with an energy equal to the energy difference of the electron before and after the transition. Radiative recombination can be described by:

$$A^{z+1} + e \Leftrightarrow A^{z} + \gamma \qquad (2.1.6)$$

where e is the free electron, A^{z+1} and A^{z} represent ions in charge state $z+1$ and z respectively and γ is the emitted photon.

The inverse process to Radiative Recombination is the Photoionisation, i.e. the well know photoelectric effect. In this process, the absorption of a photon by a bound electron results in the release of the electron into the continuum. The photoelectric effect is described by the equation:

$$A^{z} + \gamma \Leftrightarrow A^{z+1} + e \qquad (2.1.7)$$

Fig. 2.1.4 illustrates the two bound to free processes.

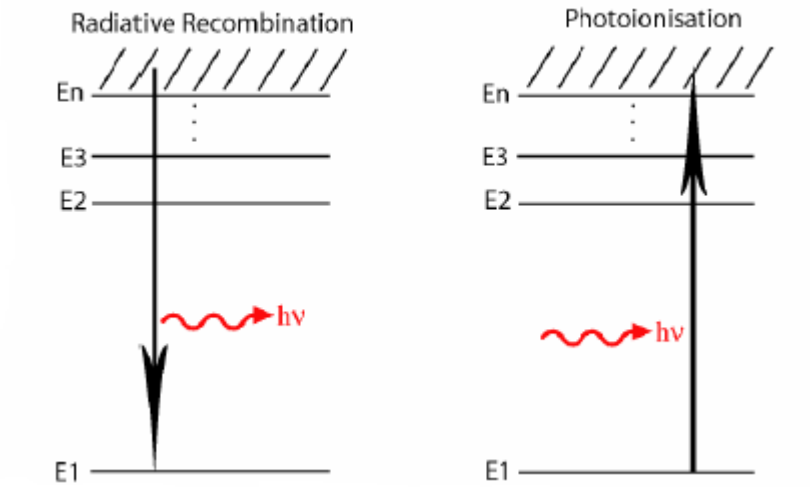

Fig. 2.1.4 – Schematic illustration of the Radiative Recombination (left) and Photoionization (right) atomic processes that occur in laser produced plasmas. E_1, E_2, E_3…E_n are bound electronic states of the atom / ion [50].

2.2. X-ray emission

Once the plasma has gained thermal energy, part of this energy is converted into e.m. radiation in the X-ray spectral range. Three different processes, namely Bremsstrahlung, recombination and line emission contribute to the X-ray emission.

In the first mechanism, free electrons interacting with the Coulomb potential of the ions, radiate in a continuum electromagnetic spectrum. The second process consists in the transition from initial free electron states to bound electron states and produces a continuum electromagnetic spectrum. The third emission mechanism produces a line spectrum as a result of transitions between discrete (bound) levels of ionized atoms [51]. In the following, we will discuss of these mechanism in detail.

2.2.1. Bremsstrahlung

Bremsstrahlung (free-free emission) produces a continuum of radiation where the logarithm of the x-ray energy spectrum is a straight line when the electron distribution is a Maxwellian. Often, laser-produced plasmas are best represented using a bi-Maxwellian structure due to the presence of hot electrons. The plasma is described by two temperature components, a thermal (or 'cold') temperature, T_c, representing the bulk of the plasma electrons, and a suprathermal (or 'hot') temperature, T_h, describing the smaller number of high energy electrons produced by the interaction of the laser electric field with the plasma.

The free-free emission from plasma can be calculated using [52]:

$$\varepsilon_B(\omega, T_e) \propto \frac{Z n_e^2}{\sqrt{T_e}} exp\left(-\frac{\hbar\omega}{k_B T_e}\right) \qquad (2.2.1)$$

To account for a two-temperature electron distribution, Eq.(2.2.1). is calculated for both temperatures and the total emission is given by the summation, taking into account the smaller number of hot electrons, n_h, in comparison to the number of cold electrons, n_c, by introducing a relative fraction, f, such that $n_h = f n_c$.

2.2.2. Recombination emission

Recombination radiation (free-bound) occurs when a free electron recombines with an ion initially at a charge state $Z + 1$, to form an ion having charge state Z. Defining E_k^e the kinetic energy of the electron and E_Z^n the energy of the final atomic state, the emitted photon has an energy:

$$\hbar\omega = E_k^e + E_Z^n \qquad (2.2.2)$$

Since the initial electron energies can take values over a continuum, the radiation is emitted in a continuum frequency spectrum. However the contribution of each transition to the continuum satisfies the condition $\hbar\omega \geq E_Z^n$ (recombination edge), so that the continuum recombination spectrum is characterized by "jumps", corresponding to different recombination stages. The contribution of this kind of process to the X-ray spectrum of a laser-plasma can be understood by using the following formula for the spectral emission coefficient [52]:

$$\varepsilon_r(\omega, T_e) \propto W_B \frac{Z^3 n_e^2}{\sqrt{T_e^3}} \sum_{n=1}^{\infty} \frac{1}{n^3} exp\left(\frac{Z^2 E_H}{n^2 k_B T_e} - \frac{\hbar\omega}{k_B T_e}\right) \qquad (2.2.3)$$

where E_H =13.6 eV is the Hydrogen ionization energy.

2.2.3. Line emission

Spectral line emission (bound-bound) is emitted when an electron decays from an excited state E_u to a lower energy level E_l, emitting a photon with energy $\hbar\omega_0 = E_u - E_l$ equal to the difference between the levels. Its rate coefficient is the Einstein coefficient:

$$A_{ul} = \frac{4}{3\hbar c} m_e r_0 \omega_0^3 g_l \sum_{j=1}^{3} \left|\langle f | x_j | i \rangle\right|^2 \qquad (2.2.4)$$

where r_0 is the classical electron radius, $\langle f|x_j|i\rangle$ is the matrix element of the x_j operator between the final and the initial states and g_l is the degeneracy of the final state.

The emission coefficient due to the spontaneous decay , that is, the specific power radiated per unit volume, solid angle and frequency interval, corresponding to the transition from the upper state u to the lover state l is:

$$\varepsilon(\omega) = \frac{\hbar\omega}{4\pi} A_{ul} N_Z^u L(\omega - \omega_0) \qquad (2.2.5)$$

where N_Z^u is the density of the ions in the upper state and $L(\omega-\omega_0)$, which is normalized to 1, is the line shape. In this formula, the energies of the levels and the Einstein coefficient are intrinsic properties of the radiating ions or atoms, and tabulated values [53] have been obtained by quantum mechanics calculations and confirmed by indirect measurements. On the contrary, both N_Z^u and $L(\omega-\omega_0)$ depend on the physical conditions of the plasma in which the radiating atoms or ions are embedded. In particular, populations are determined by the dynamical balance of several collisional and radiative processes inside the plasma.

Three main physical processes determine the line shape:

a. the finite radiative lifetime of the bound states involved in the transition (natural broadening);
b. the thermal motion of radiating atomic systems (Doppler broadening);
c. the interaction of radiating systems with the rest of the plasma (pressure broadening).

Natural line broadening is determined by the sum of transition probabilities for all spontaneous transitions originating from both upper and

lower levels involved in the transition. In this case the line shape is a Lorentzian:

$$L(\nu - \nu_{u,l}) = \frac{L_0}{1 + \left[\frac{2(\nu - \nu_{u,l})}{\Delta\nu_N}\right]^2} \qquad (2.2.6)$$

where the characteristic width is determined by the mean lives of the two levels τ_l and τ_u according to the following expression:

$$\Delta\nu_N = \frac{1}{2\pi\tau_l} + \frac{1}{2\pi\tau_u} \qquad (2.2.7)$$

Doppler broadening depends on the Maxwellian (thermal) velocity distribution of ions and leads to a normalized Gaussian line profile written as:

$$L(\nu - \nu_{u,l}) = L_0 exp\left[-\left(\frac{2\sqrt{\ln 2}\,(\nu - \nu_{u,l})}{\Delta\nu_D}\right)^2\right] \qquad (2.2.8)$$

with

$$\Delta\nu_D = \frac{2\nu_{u,l}}{c}\sqrt{\frac{2\ln 2\, k_B T}{M}} \cong 6.65 \times 10^{-9}\sqrt{\frac{T_i(eV)}{A}} \qquad (2.2.9)$$

where the FWHM depends upon the ionic temperature T_i and the atomic mass number A.

Pressure broadening is the result of collisions that reduce the effective lifetime of a state, leading to broader lines. The characterizing parameter of this phenomenon is ν_P, i.e. the collisions frequency between atoms. Considering negligible the collision duration compared to the lifetime of atomic levels, for an interaction with a cross section σ, the line shape is essentially a Lorentzian and the FWHM is given by:

$$\Delta\nu_P = \frac{1}{2\pi\tau_P} \approx \frac{\sigma v_{rel} n_P}{2\pi} \qquad (2.2.10)$$

where n_p is the number density of the perturbers and v_{rel} is the relative velocity of the interacting atomic systems.

The so-called Stark broadening is the most important pressure broadening mechanisms in a plasma. It is due to the interaction of the radiating system with the microscopic electric fields produced by the surrounding particles.

2.3. Equilibria in Plasma

The first issue to be addressed in the study of emission of radiation from a plasma is the kind of equilibrium to be considered. The degree of interaction among the three plasma sub-systems, namely electrons, ions and radiation, must be specified in order to determine the population of all available energy levels. Consequently, one can determine the spectral distribution of radiation energy emitted via bound-bound, free-bound and free-free transitions.

There are a number of approximations that can be used in order to establish the population distribution within plasma at a specific temperature. In the following, a summary of the main results on plasma equilibria will be given with emphasis on the conditions to be fulfilled, in terms of density and temperature, for the various types of equilibria to hold.

2.3.1. Complete Thermal Equilibrium - CTE

When radiation cannot escape from the plasma volume due to re-absorption effects (the so-called opacity) within its volume, the plasma is said to be optically thick and every atomic process occurring in the plasma is balanced by an equal and opposite process (for example the rate of collisional excitation equals the rate of collisional de-excitation). In this case, the plasma

is said to be in CTE - Complete Thermal Equilibrium: it is an ideal case for low energy laser expanding plasmas.

Although this kind of equilibrium does not apply to laboratory plasmas and is only approached in stellar interiors, it can be considered as a reference condition in the limit of high plasma density.

A plasma is said to be in CTE when electrons, ions and radiation are strongly coupled to each other and share the same temperature.

The CTE can be assumed when [49]:

a. all particles follow to the Maxwell velocity distribution law:

$$f(v) = 4\pi n_e v^2 \sqrt{\left(\frac{m_e}{2\pi k_B T_e}\right)^3} exp\left(-\frac{m_e v^2}{2k_B T_e}\right) \qquad (2.3.1)$$

b. the population distributions over the states of any atom or ion are given by the Boltzmann formula:

$$\frac{N_{z-1}(p)}{N_{z-1}(q)} = \frac{g_{z-1}(p)}{g_{z-1}(q)} exp\left(-\frac{\chi_{z-1}(p)}{k_B T_e}\right) \qquad (2.3.2)$$

where $n(p)$, $n(q)$, $g(p)$ and $g(q)$ are respectively the populations and statistical weights of states labeled with p and q, and $\chi_{z-1}(p)$ is the energy difference between levels p and q;

c. the number of ions in a charge state Z relative to the number in state $Z-1$ is given by the Saha equation:

$$\frac{N_z n_e}{N_{z-1}} = 2\sqrt{\left(\frac{2\pi m_e k_B T_e}{h^2}\right)^3} \frac{2g_z}{g_{z-1}} exp\left(-\frac{\chi_{z-1}}{k_B T_e}\right) \qquad (2.3.3)$$

where N_z and N_{z-1} are the ion stage populations, g_z and g_{z-1} are the statistical weights associated to the energetic levels within these ion stages, T_e is the electron temperature, χ_{z-1} is the ionization potential of the ion of charge $z-1$.

d. the radiation intensity distribution as a function of frequency and temperature can be described by the black body radiation distribution function:

$$I(\nu, T) = \frac{2h\nu^2}{c^2}\left[\frac{1}{exp\left(\frac{h\nu}{k_B T_e}\right) - 1}\right] \qquad (2.3.4)$$

Since the laser plasma is a highly dynamical system, CTE cannot exist, as clearly evidenced by the emitted radiation and by the velocity distributions. For more practical reasons, equilibrium models have been developed to describe plasmas in different regimes with less demanding requirements respect to CTE.

2.3.2. Local Thermal Equilibrium – LTE

The LTE model is very close to CTE and is applicable to high density and hot plasmas, such as solar interiors, and laser plasmas at the early stage of their expansion. LTE is assumed when the plasma density increases to very large values (> 10^{15} cm^{-3}) and the rate of collisions prevails on radiative processes. This minimizes the amount of energy losses and thus the system is locally approximated to a thermodynamic equilibrium system.

LTE is distinguished from complete thermodynamic equilibrium in that the temperature need not be the same everywhere, and the spectrum is not characteristic of a pure blackbody.

Due to the mass difference, the electrons have larger velocities than the ions, being more collisional. They are therefore responsible for the bulk plasma collisional transitions, which rate is used to determine the electron temperature.

The expression of electrons density required to obtain the LTE is:

$$n_e \geq 1.6 \times 10^{14} T_e^{1/2} \chi(p,q)^3 cm^{-3} \qquad (2.3.5)$$

where the electron temperature, T_e, and the highest ionization energy of any atoms or ions, χ (p, q), are expressed in eV.

2.3.3. Coronal Equilibrium – CE

For relative low density plasmas LTE cannot be applied, since the electron density decreases drastically. The solar corona for example, has a high temperature (10^6 K) but is usually at low density (10^8 cm^{-3}). In this case, the relative populations of high energy levels are controlled by the collisions between particles. In this case, coronal equilibrium prevail.

CE can be applied if [49]:

$$n_e \leq 5.9 \times 10^{10} Z^6 T_e^{1/2} exp\left(\frac{Z^2}{10T_e}\right) cm^{-3} \qquad (2.3.6)$$

This expression is valid for hydrogen-like ions assuming as upper limit the level n=6.

2.3.4. Collisional Radiative Equilibrium – CRE

CRE describes a middle range of density values between LTE and CE: it tends to the CE at low density and to LTE at higher plasma density. Both collisional (only involving electrons) and radiative processes are taken into account. The velocity distribution is still supposed to be Maxwellian: the electron-electron relaxation time is smaller than electron heating time. Ion populations of charge *z+1* must not change dramatically when the quasi-steady-state population of ions of charge *z* has been established. Moreover, in CRE the plasma is supposed optically thin to its own radiation.

Fig. 2.3.1 illustrates and summarizes the range of validity of each model for a range of plasma densities and temperatures.

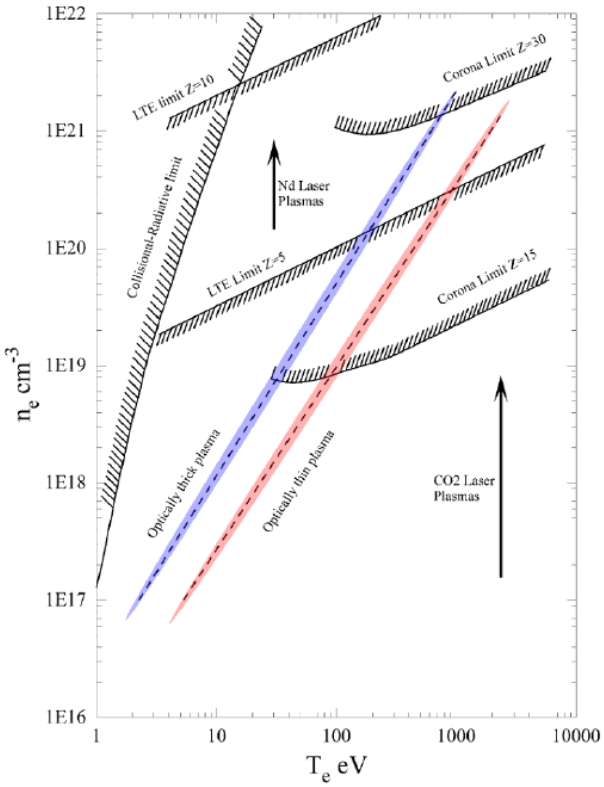

Fig. 2.3.1 - Ranges of validity for the application of the different plasma equilibrium models.

For a Nd:YAG laser plasma with electron density on the order of $1 \cdot 10^{18}$ $cm^{-3} < n_e < 5 \cdot 10^{19}$ cm^{-3}, with low charge states, on the order of $1 < z < 5$ the validity of the model is listed as follow:

a. LTE model applies for electron temperatures on the order of $10 < T_e < 100$, i.e. in the early stage of the plume expansion;
b. CR model applies only for higher temperatures, up to $T_e = 30$eV ;
c. CRE model applies only for very low temperatures, hence when the plasma cools down, i.e. at later expansion stages, for density values between the validity range of LTE and CR.

2.4. Dynamics of laser ablation

Laser ablation of solids with nanosecond pulses of high intensity leads to complicated interactions of the laser beam with both the solid and the ablated material. There exist a number of processing parameters, which determine the dynamics of ablation and properties of the generated plasma [54-58] . Some of the fundamental physical features such as the nature of the laser absorption in the vaporized material and acceleration mechanism for the ions are not yet fully understood.

Interaction of a nanosecond laser pulse on a solid surface causes heating and melting of the irradiated volume. The rapid rise in temperature leads to intense evaporation of atoms and molecules from the solid surface that is to the formation of an expanding plasma. The laser power density critically controls the basic properties of these plasmas. Generated plasma also depends on other laser parameters like, pulse width, intensity profile and the material characteristics. Even at relatively low intensities near the threshold for ablation, it is observed that the ablated material is significantly ionized and the ions in the plasma plume have energies ranging up to several hundred electron volts (eV). After the initial ionization, it is the field strength and the

quiver motion of free electrons that enables further ionization of matter, forming a dense 'free' electron cloud. If the electron density is high enough in the Debye-sphere, the plasma behaves in a collective manner. The first salient aspect of the laser-induced plasma is its fast dynamics, along with its inhomogeneity in density, temperature and flow velocity. The laser interaction itself is characterized by a limiting electron density beyond which no electromagnetic propagation is possible i.e., beyond critical density where laser is efficiently absorbed by the electron population through collisional inverse bremsstrahlung [59-61]. This property is the main reason for laser plasmas to be very hot and more or less close to ideality, and is responsible for sharp density variations in the transition zone from under-dense to over-dense plasma.

Initially the expansion of the plume is primarily driven by the plasma pressure gradients [62], but there may be an additional contribution from coulomb repulsion between the ions if there is significant net loss of the more mobile electrons. In any case, when the plume has propagated more than a few hundred millimeter from the target surface, major part of the initial thermal energy in the plasma is converted to the directed kinetic energy of the ions, which are much more massive than the electrons.

The adiabatic expansion models of Anisimov et al. [54] and Singh and Narayan [55] have proved to be very useful for the understanding and interpretation of the laser ablation experiments.

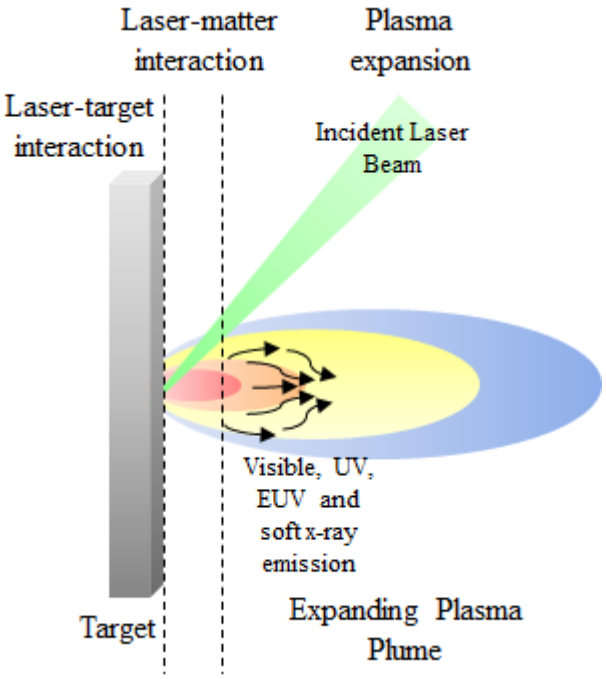

Fig. 2.4.1 – A schematic view of the processes that take place during ablation by a ns laser pulse. Light absorption in the solid, ejection of the ablated material in a plasma plume and the interaction of the light with the plume, and the plasma expansion.

Different stages of laser-matter interaction and plasma formation mechanisms (Fig. 2.4.1) are explained in the coming sections of this chapter.

2.4.1. Laser-Target interaction

When the intense laser beam strikes the target surface, part of the energy is reflected back and the remaining part is absorbed by the electrons in the target. Once inside the material, absorption causes the intensity of the light to decay with depth at a rate determined by the material's absorption coefficient α. In general, α is a function of wavelength and temperature, but for constant α, intensity I decays exponentially with depth z according to the Beer–Lambert law:

$$I(z) = I_0 e^{-\alpha z} \qquad (2.4.1)$$

where I_0 is the intensity just inside the surface after considering reflection loss.

The primary heating of the target leads to strong evaporative ejection of material. Since the heating is extremely fast, surface temperatures close to the thermodynamic critical temperature can be reached. After a period of tens of picoseconds, the electrons and atoms in the solid equilibrate which leads to a strong heating of the irradiated volume. The removal of the material from the target by laser irradiation depends on the coupling of the beam with the solid. Intense heating of the surface layers by high-powered nanosecond laser pulses occurs, resulting in melting and/or evaporation of the surface layers, depending on its energy density. These thermal effect of nanosecond interaction of laser beams with metals have been dealt with extensively in the literature [63, 64]. Essentially, it involves the solution of one-dimensional heat flow equation with appropriate boundary conditions taking into account the phase change in the material. Heating rate, melting, evaporation during pulsed-laser irradiation are influenced by the laser parameters, i.e. laser intensity, pulse duration and wavelength, and thermo-physical properties of the material. In addition to this, the behavior of the plasma expansion also depends on the initial plume dimensions and background gas pressure.

During the rising edge of the laser pulse, radiation is absorbed by electrons in the so-called skin depth layer, raising them to higher energy states in the conduction band. These electrons then pass this energy on to the lattice during collisions, which quickly heat and melt the surface. This results in a decreased reflectivity of the surface, thereby increasing the proportion of the laser-light that is absorbed by the target. The skin depth hence represents the length in which the laser EM field can penetrate into the solid target.

For aluminum target irradiated by a Nd:YAG laser with wavelength of 1.064 μm, $\delta \simeq 5$nm.

For nanosecond time-scale pulses a significant amount of heat is conducted from the skin depth layer into the bulk of the material, to a depth known as L_{th}, called diffusion length or heat penetration depth [65]:

$$L_{th} = \sqrt{2D_{th}\tau} \qquad (2.4.2)$$

where τ is the duration of the laser pulse and D_{th} is the material's thermal diffusivity. Under such conditions the energy of the laser pulse is stored inside a hole that can be approximated to a cone having the base diameter equal to the ablation spot size, and height comparable to the diffusion length. Hence, L_{th} fixes the depth of the crater produced by the laser pulse interacting with the target. By adding to the diffusion length the skin depth we obtain the total absorption depth $Z = L_{th} + \delta$. In the nanosecond pulse regime, generally L_{th} is on the order of some μm, hence the relation $L_{th} \gg \delta$ is valid.

2.4.2. Laser-Matter interaction

In the second stage, the material from the heated volume is ejected from the target but continues to absorb energy from the laser beam, resulting in the formation of a thin layer ionized of vapor on the surface of the target. In the early experiments, the physical mechanisms involved in the absorption of the laser energy by the evaporating material were identified as the source for very high temperature (~1 keV) plasma.

The high surface temperature induced by laser irradiation leads to emission of positive ions and electrons from free surface. The flux of ions and electrons as a function of temperature can be predicted by the Richardson and

Langmuir-Saha equations [66-68] respectively. Both of these equations show an exponential increase in the fraction of ionized species with temperature.

Different mechanisms can play an important part in the ionization of the laser-generated species. Impact ionization and other mechanisms, especially photoionization, thermal ionization of photon-activated species and electronic excitation may affect the concentration of the excited species.

The evaporated material from the target is further heated by the absorption of the laser radiation. The heating of the evaporated material is controlled by the plasma absorption coefficient, which depends on the concentration of the ionized species, on the plasma temperature and on the laser wavelength. The absorption coefficient of the plasma can be expressed as:

$$\alpha_p = 3.69 \times 10^8 \left(\frac{Z^3 n_i^2}{T^{0.5}\nu^3}\right)\left[1 - exp\left(-\frac{h\nu}{k_B T}\right)\right] \qquad (2.4.3)$$

where Z, n_i and T are the average charge, the ion density, and the temperature of the plasma respectively.

The laser radiation is highly absorbed if the value of the product αL, where α is the absorption coefficient and L is the plume dimension in the plane perpendicular to the target surface, is large. However since α is proportional to the plasma density, the strongest absorption occurs near the target surface and the subsequent heating of the evaporated material is strongly related to its value.

Because of the high expansion velocities of the leading plasma edge, the electron and ion densities decrease very rapidly with time and space, which makes the plasma transparent to the laser beam for large distance away from the target surface. The laser radiation again reaches the target. These processes merge into a smooth self-regulating regime with the generation,

heating and expansion of plasma taking place throughout the length of the laser pulse.

2.4.3. Plasma expansion

After the end of the laser pulse, quick electrons are the first vaporized particles that escape from the plume; they are then followed by accelerated ions of different charge states. In this early expansion stage, several Double Layers (DLs) [69] can be formed and strong electrostatic fields creating plasma instabilities can break the plasma quasi neutrality over lengths larger than λ_D. DLs are known as localized electrostatic potential structure created by two equal opposite space-charge layers, which are capable of sustaining high potential drops in collisionless plasmas. In a low power density regime ($\sim 2 - 25 J/cm^2$), a DL structure can manifest through double-peaked time-of-flight ion signals, as studied by Bulgakova [70]. Increasing the laser fluence, a transition region is observed and more than one DL can be observed [71].

The presence of DLs in LPP can be supposed when the simultaneous existence of hot and cold electron population (which is indicated with TET-Two Electron Temperature) is detected. However also in a SET-Single Electron Population plasma DL can be formed [70].

After the termination of the laser pulse, no particles are evaporated and injected into the inner edge of the plasma. An anisotropic adiabatic expansion occurs where the temperature, T, decreases with the plasma dimension, in accordance with the adiabatic thermodynamic equation given by [55]:

$$T[X(t)Y(t)Z(t)]^{\gamma-1} = const \qquad (2.4.4)$$

where *X(t)*, *Y(t)* and *Z(t)* are the dimensions of the expanding plasma in the three orthogonal directions, and γ is the ratio of the specific heat capacities at constant pressure and constant volume.

The thermal energy is rapidly converted into kinetic energy, with plasma attaining supersonic expansion velocities.

Finally, when the plasma becomes spatially broadened, the free streaming of the plasma plume starts during its last stage of expansion. The plume becomes collisionless since $L/\lambda_L >> 1$, where L is the plasma length and λ_L is the mean free path. In this last stage the plasma expands isothermally. Then the plasma decays into the free flight and no longer collisions occur.

Chapter 3

Experimental set-up

In this chapter, a report of experimental technique for the spatio-temporal evolution of the laser produced plasma and the various diagnostics needed for the experiments are given.
Moreover, the samples preparation technique and the features of nanostructures investigated will be discussed.

3.1. Laser setup

In the present work, studies on plasma formed by the interaction of a focused laser beam on different nanowires targets are described.

The laser used in our experiment is a Q-switched Nd:YAG laser having a maximum energy of 2 J, a fundamental wavelength of 1064 nm, a duration of 6 ns and a repetition rate of 10 Hz.

The laser pulse is focused onto a flat target by means of a plano-convex lens with 75 mm focal length, and 25 mm diameter. The interaction with the target occurs inside a vacuum chamber, where a pressure of about 10^{-5} mbar is kept by means of a turbo-molecular pump. The laser beam impinges on the target with an angle of 30° with respect to the normal. This is the axis along which the expansion direction of the plasma occurs. The best focusing condition of the laser beam on the target was obtained by varying the lens-target distance in order to maximize the soft X-ray yield. The total intensity reached was in the range 10^{12}-10^{13} W/cm^2.

The vacuum chamber is cylindrical stainless steel tube with diameter 80 cm and is provided with appropriate windows for laser beam entrance and light collection.

A schematic representation of the vacuum chamber and relative diagnostics is shown in Fig. 3.1.1.

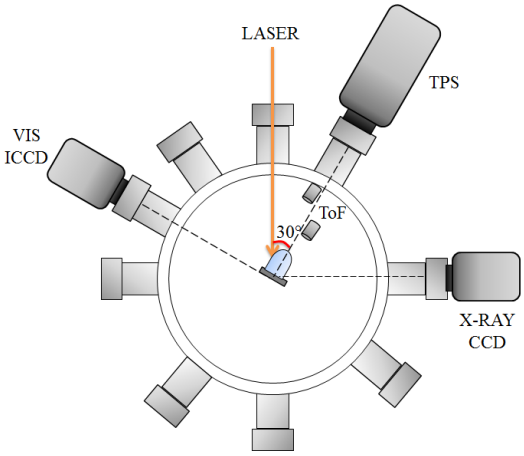

Fig. 3.1.1 – Schematic view of the experimental setup showing the main diagnostics used in the experiment.

A metal target holder has been employed to keep the target in position and to connect it to an externally controlled X-Y-Z motor. The z-axis movimentation is used to change the distance between the lens and the target in order to find the focus position; while movimentation along x and y-axis is need to avoid errors due to local heating and drilling by providing fresh surface for ablation.

Several detectors for visible and X-ray radiation and ionic component studies (described in detail in the following sections) are connected to the vacuum chamber. All the diagnostic is equipped with an external trigger signal, which is synchronized with the beginning of the laser pulse.

3.2. Optical fast imaging

Time resolved optical imaging of laser produced plasmas with fast framing cameras has been a useful and widely used diagnostic over the past three decades [72-74].

The detector used for the optical fast imaging is an Intensified Charged Coupled Device (ICCD), comprised a gated intensifier coupled to a front illuminated (CCD) camera via a high quality relay lens system (Fig. 3.2.1), which was supplied by Andor Technology.

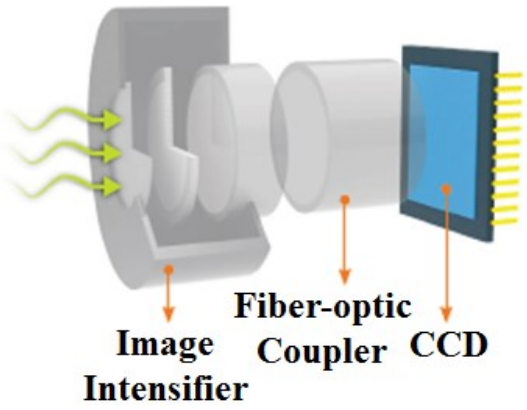

Fig. 3.2.1 – Sketch of an Intensified CCD.

The CCD chip consist in 1024×1024 pixels with a pixel size of 13 μ m and an effective active area of 13.3×13.3 mm^2.

The Image Intensifier tube is an evacuated tube, which comprises a Photocathode, a Microchannel plate (MCP) and a Phosphor screen, as shown in Fig. 3.2.2, and the properties of these determine the performance of the device [75].

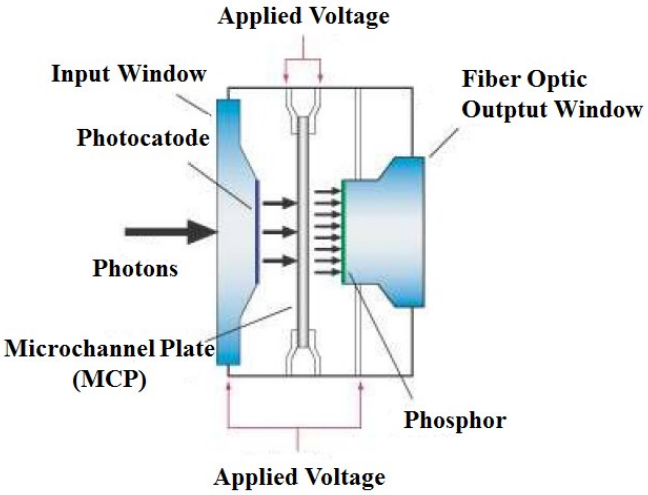

Fig. 3.2.2 – Overview of Image Intensifier construction.

The photocathode is coated on the inside surface of the input window and it captures the incident image. When a photon of the image strikes the photocathode, a photoelectron is emitted, which is then drawn towards the MCP by an electric field. The MCP is a thin disc (about 1 mm thick) which is a honeycomb of glass channels typically 6-10 μm, each with a resistive coating. A high potential is applied across the MCP, enabling the photoelectron to accelerate down one of the channels in the disc. When the photoelectron has sufficient energy, it dislodges secondary electrons from the channel walls. These electrons in turn undergo acceleration, which results in a cloud of electrons exiting the MCP. The degree of electron multiplication depends on the gain voltage applied across the MCP, which can be controlled in the camera.

The output of the image intensifier is coupled to the CCD typically by a fiber optic coupler.

The high temporal resolution means that the plasma can be tracked over time and subsequently the images processed to extract important information such as their spatio-temporal distributions and velocities.

The ICCD is equipped with an internal Digital Delay Generator (DDG). An external trigger source activates the DDG, so that it can control the image intensifier for gating applications.

The bright plasma emission was observed through a window perpendicularly placed to the plasma expansion direction.

3.3. X-Ray emission characterization

Due to the strong X-ray emissivity of laser-produced plasmas, a CCD-camera in X-rays domain coupled with an array of pinhole is a fundamental diagnostic tool.

The CCD camera, by Andor Technology, consists of a 26.7×6.7 mm^2 CCD device with 1024×256 X-ray sensitive silicon pixels, allowing the direct detection of X-ray photons. Each pixel is 26 μm size and it is back illuminated; in this way the absorption of X-rays in the low-energy domain is minimized. The CCD can be cooled down to a temperature of 100 °C (under vacuum) obtaining a strong reduction of the dark-signal [76].

The Quantum Efficiency (QE) of the CCD is an important parameter because it allows deducing the probability that incident photons are absorbed in the depletion region of the sensor. Although there are other factors, which effect the final shape of the QE curve, such as the different materials and their different absorption coefficient and the reflectance of the silicon, the most dominant and straightforward impact on the sensor QE is the structure of the CCD [77]. The QE for our detector is the green dashed curve in Fig. 3.3.1. To note is the discontinuities or edges seen in the QE are the result of the intrinsic properties of the silicon, the absorption edges L-edge at 100.6 eV and K-edge at 1.8 keV.

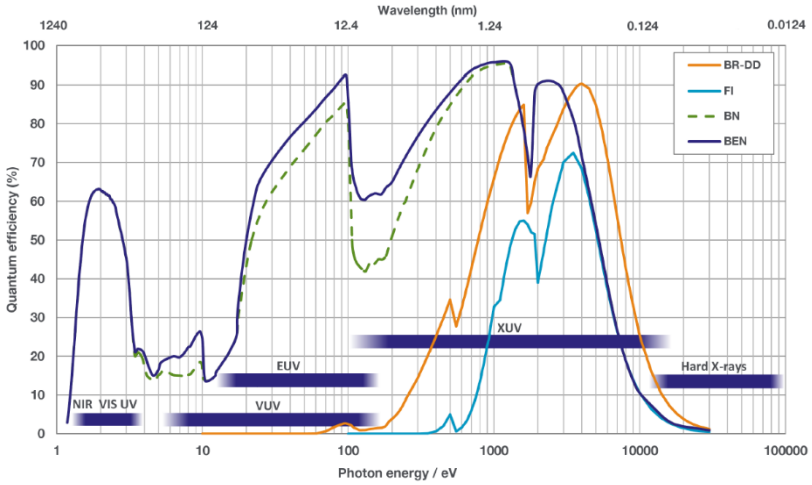

Fig. 3.3.1 – QE curve for X-ray detection.

The camera was equipped with a pinhole array in order to allow the detection of simultaneous signals, as shown in Fig. 3.3.2. Each pinhole, with 1 mm diameter, was filtered to be sensitive to a different spectral region by using Al-made attenuators of increasing thicknesses, ranging from 3 to 20 μm.

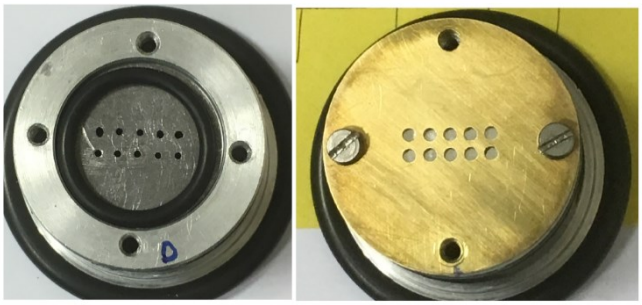

Fig. 3.3.2 – An eight-pinhole array on the left and Al-made attenuators on the right.

The X-ray transmission curves for different Al thickness are plotted in Fig. 3.3.3 as a function of the X-ray photon energy in the range from 100 eV to 10 keV [78]. The imaging channels filtered with 'thin' Al foil (2 – 10 μ m) are sensitive to photon energies under 1 keV, while higher thicknesses are sensitive to energies above approximately 3 keV.

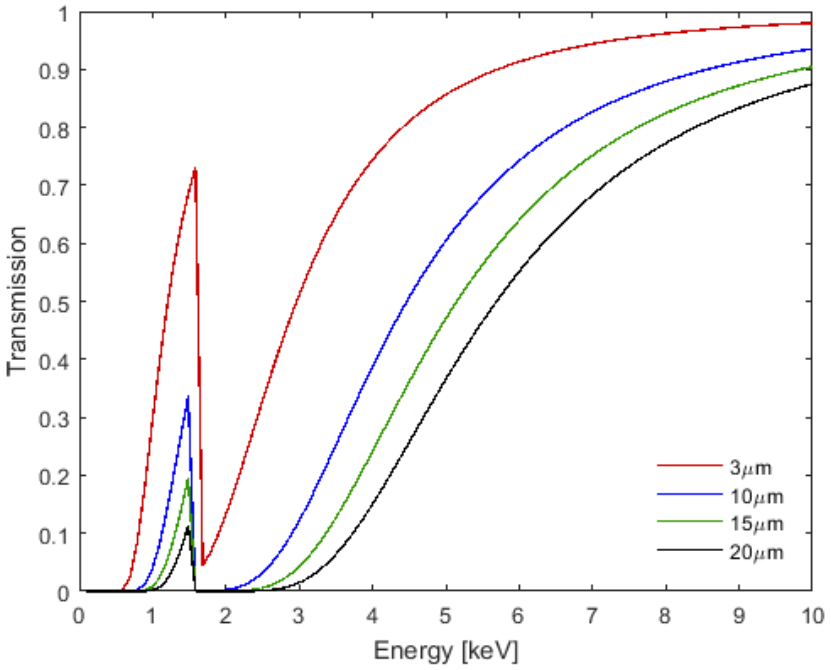

Fig. 3.3.3 – X-ray transmission curves of 3 - 10 - 15 - 20 μm thick Al foil.

3.4. Time of Flight studies

Time-of-flight measurements allow to collect the passing electrons or ions (depending on the polarity of the bias voltage). By knowing the exact moment in which the laser strikes the target surface, the velocity distribution of charged particles escaped from the plasma can be calculated.

For this measurement, LEMO connectors at negative voltage have been used as ion collectors. Signals from the LEMO were amplified outside the chamber and sent to a digital oscilloscope, which register them as a change in current.

Ion collectors at different distances have been placed inside the chamber, one approximately 15 cm from the target (ToF near) and one approximately 30 cm (ToF far), to about 5° respect to the plasma direction propagation.

3.5. Thomson Parabola Spectrometer

The Thomson Parabola Spectrometer (TPS) has been employed to characterize ion beams.

The working principle [79-83], is based on parallel electric and magnetic fields acting on a well-collimated ion beam propagating orthogonally to the fields themselves. The Lorentz force splits the different ion species of the according to their charge-to-mass ratio and energy. The result is a series of parabolic traces on a detector, each of them corresponding to a well-determined ion species.

Ions enter the TPS through two pinholes. The first one is 1 mm in diameter and 2 cm thick double layer matrix of brass and lead in order to collimate the ions beam and to shield the detector from γ - and x-rays. The second is 100 μm in diameter and 1 mm thick aluminum layer; it is responsible for the spatial and energetic resolution of the spectrometer. The pinhole distance is 10 cm. Later, a deflection sector composed by parallel electric and a magnetic field partially overlapping with each other is placed. The magnet length is 15 cm and the iron is H shaped in order to provide a field as uniform as possible along the particle trajectory. While the electrodes are copper plates with a length of 7 cm. The distance of the fields centers is 6 cm long, so the overlapping zone is 5 cm long and the electric field end 2 cm after the magnetic one.

The vacuum chamber is connected to an independent camera operating at a pressure of 10^{-6} Torr, to provide differential pumping and isolation from the target chamber. After passing the drift region, which allows to increase the particles deflection and separation among different traces, the ions position is detected using a imaging system. In our case, a microchannel plate coupled to a phosphor screen 2 cm in diameter (MCP-PH) and a reflex camera has been used to acquire the produced light.

The full spectrometer layout is reported in Fig. 3.5.1, with the distances of each sector from the collimator to the detector.

The TPS was placed in backward direction, rotated 30° angle to incidence direction of laser beam and at a distance of the MCP-PH from the target of 137 cm.

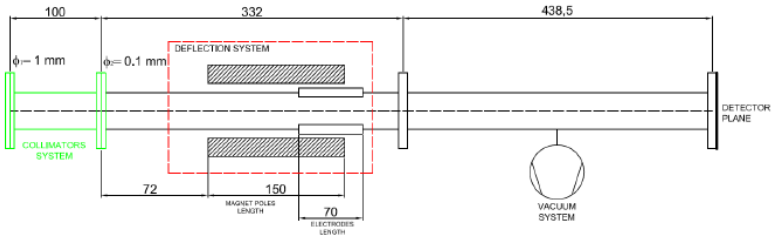

Fig. 3.5.1 – Thomson Parabola Spectrometer layout.

3.6. Nanostructured targets

The plasma is produced by interaction of laser with nanostructured targets. Therefore, in the following section, we will briefly describe the fabrication technique of metal nanowires and the features of nanostructured targets used.

3.6.1. Sample preparation technique

A well-established strategy for NWs fabrication is electro-chemical deposition in Porous Anodized Alumina Templates.

Porous Alumina (aluminum oxide, Al_2O_3) is obtained by electrochemical anodization in sulphuric or oxalic acid solutions (depending on desired diameter) of pure aluminum sheets, producing a layer of porous oxide with highly regular geometry (honeycomb-like hexagonal cell structure, as can be seen in Fig. 3.6.1). The pores - or channels - created this way are perpendicular to the surface and have a narrow distribution of diameter and

length. Due to this, they can be used as "guides" for deposition of metals, allowing the fabrication of nanowires [84].

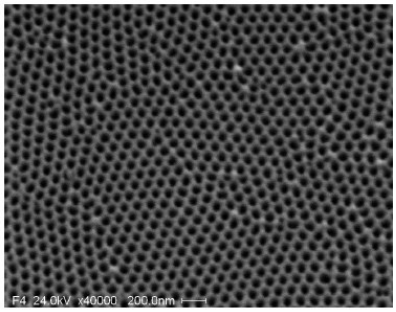

Fig. 3.6.1 – SEM image of view from above nanoporous alumina.

Several geometrical parameters of the alumina template can be controlled by anodization conditions (Fig. 3.6.2):

- The distance between the centers of adjacent pores called *interpore distance* d_{int};
- The *pore diameter* d_p;
- The *barrier thickness*, i.e. the thickness of continuous oxide layer at the bottom of channels;
- The *wall thickness*, i.e. the thickness of oxide forming a wall between the pores.

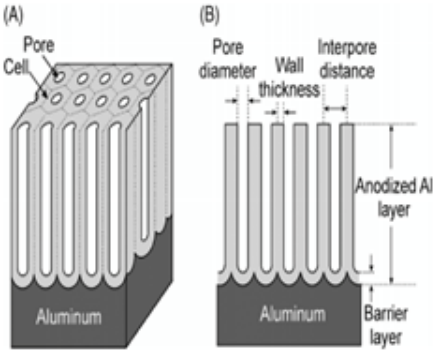

Fig. 3.6.2 – Idealized structure of anodic porous alumina (A) and a cross-sectional view of the anodized layer (B).

Once a nanoporous matrix with the desired geometry has been obtained, the pores are filled with metal through electrodeposition. The electrodeposition method consists in the growth of a metallic material on top of a conducting substrate, by electrochemically reducing metal ions present in an electrolyte solution.

Since alumina is non conductive, the barrier layer at the bottom of the pores prevents electrodeposition using DC current.

Therefore, AC deposition is used. This is possible because the barrier acts in a similar way to a capacitor and current rectifier, allowing growth of nanowires in the pores. NWs deposited in AC are insulated from each other and the aluminum substrate.

In order to allow DC deposition, it is necessary to remove the barrier by detaching the whole oxide layer from the aluminum substrate. The barrier can be removed from the bottom in mechanical or chemical way, but this requires a thick oxide layer to survive the process. A different approach to barrier layer opening is electrochemically etch the barrier from the pores side. DC deposition can be used to grow NWs independently of total oxide thickness, and without detachment from the bulk aluminum. It should be noted that the electrical behavior of the resulting material is affected in that the nanowires deposited in DC directly contact the aluminum substrate.

Changing anodization and deposition conditions allows control over the resulting NWs shape and structure. Moreover, many different metals can be deposited in the pores [85-88]. In this way, it is possible to investigate the behavior of plasma produced by laser-nanomaterial interaction with different features.

3.6.2. Irradiated samples

The samples were produced at the INFN nanotechnology lab in Bologna with the aim to compare the main variables of interest: nanowires composition, nanowires diameter, nanowires length, alumina thickness. A sample of bulk aluminum was also irradiated, to be used as reference.

Nickel NWs were produced changing the following parameter:

- ***NWs diameter***: nanowires of different diameters can be produced by using different electrolytes during anodization. In this case, 20 nm diameter NWs were obtained via sulphuric acid anodization, while 50 nm NWs via oxalic acid anodization.
- ***NWs length***: nanowires of different length can be obtained adjusting deposition times.
- ***Metal contact***: the base of nanowires can be in direct contact with the aluminum substrate, or separated by an insulating oxide layer few tens of nm thick. Most samples have been produced without electrical contact (via AC deposition), but one sample has been produced via DC deposition, so its NWs are directly in contact with the aluminum substrate.
- ***NW confinement***: for most samples, the alumina template is left intact after NWs deposition, so NWs are "confined" in the alumina. For the DC sample, the alumina layer was dissolved by chemical attack in a limited region, leaving the nanowires "freestanding". This could be done only to a sample with contacted NWs, since non contacted NWs collapse without support from the template.

Moreover, in order to compare the performances of nanowires composition, the samples were filled with four different metals (cobalt, iron, nickel and silver), and similar other parameters.

All targets irradiated with relative parameters are listed in Table 3.6.1.

NWs metal	***Al-Bulk***	***Co-Thin***	***Fe-Thin***	***Ni-Thin***	***Ag-Thin***
Support label	Al04	Ad7	Ad10	Ad3	AlN4
NWs diameter [nm]	/	20	20	20	40
NWs length [µm]	/	10	10	10	8
Al_2O_3 Thickness [µm]	/	10	10	10	12
Metal contact	/	No	No	No	No
NWs confined	/	Yes	Yes	Yes	Yes

NWs metal	***Ni-Long***	***Ni-Short***	***Ni-DC***	***Ni-Free***
Support label	Ad20	Ad20	Ad22	Ad22
NWs diameter [nm]	50	50	50	50
NWs length [µm]	10	5	10	10
Alumina Thickness [µm]	15	15	15	15
Metal contact	No	No	Yes	Yes
NWs confined	Yes	Yes	Yes	No

Table 3.6.1 – Irradiated samples and relative parameters.

3.7. Crater morphology and composition studies

After laser irradiation, the morphology and composition of craters in targets were studied at INFN lab in Bologna with a Huvitz HDS-5800 optical microscope. It offers a range of magnification between 240x and 5800x, and it allows target movement with 2 μm precision in the x-y plane (parallel to target surface) and 100 nm precision in the z axis (normal to surface).

The microscope has very useful image manipulation capabilities: in particular, it allow to stitch together several images in order to produce a composite image of a large surface and quickly take several (dozens or hundreds) of images at different Z position, to determine the focal plane from each, and to generate a composite 3D-model of a surface. See Fig. 3.7.1 as examples of the generated models.

The capability to easily build 3D models of the craters and to measure their geometrical parameters (such as ablated volume and depth) has allowed qualitative observation and quantitative comparison of the craters formed on different targets.

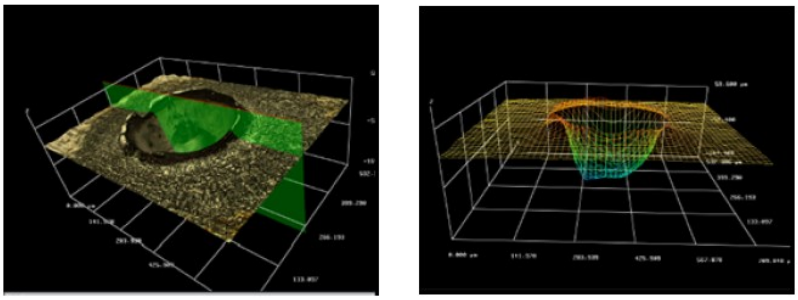

Fig. 3.7.1 – 3D model in colour view (left) and mesh view (right) generated by the optical microscope. This kind of models allow geometrical measurement with μm precision

Resolution of 3D models created by the microscope is limited by optical considerations, capabilities of the model-building software and artifacts.

Chapter 4

Experimental data: characterization of laser-produced plasmas

The experimental results regarding the characterization of plasmas produced by interaction of laser with aluminum-bulk and nanostructured materials expanding in vacuum will be presented in this chapter.

Preliminary calculations of nuclear reaction rates will be also shown.

4.1. Optical fast imaging

Fast photography provides two-dimensional snap shots of the three-dimensional LPP propagation. It is one of the versatile diagnostic tools for understanding the expansion dynamics of laser created plumes.

In laser-produced plasmas, the physical and chemical properties [89, 90] of the target are one of the governing factors determining the ion charge state, velocity, particle density, etc. Hence, depending upon the target material, the generated plume's ion emission features (velocity, flux) as well as plasma properties (temperature, density) will vary even at constant laser intensity. Therefore, we have investigated the behavior of plasma produced by interaction with different targets.

Fig. 4.1.1- Fig. 4.1.5 give typical time-resolved images for Al bulk and nanostructured targets (nanowires of Co, Fe, Ni and Ag). All these images

are spectrally integrated in the region 200–700 nm, while each image is obtained from a single laser shot and normalized to its maximum intensity in order to easily compare them to each other. A 2 ns gate width was used to image plasma at early times (<50 ns) and at later times a gate width increasingly large was used. In fact, a shorter gate width was more desirable during early expansion times to minimize spatio-temporal mixing and optimize the imaging of internal structures. Plasma properties are no longer rapidly changing at later times; therefore, a longer gate width is acceptable and used for compensating the reduction in plasma intensity with time.

The colors in the ICCD camera images indicate different radiation intensity values. Higher counts observed in the images may correspond to areas of high temperature and particle density in the plasma plume.

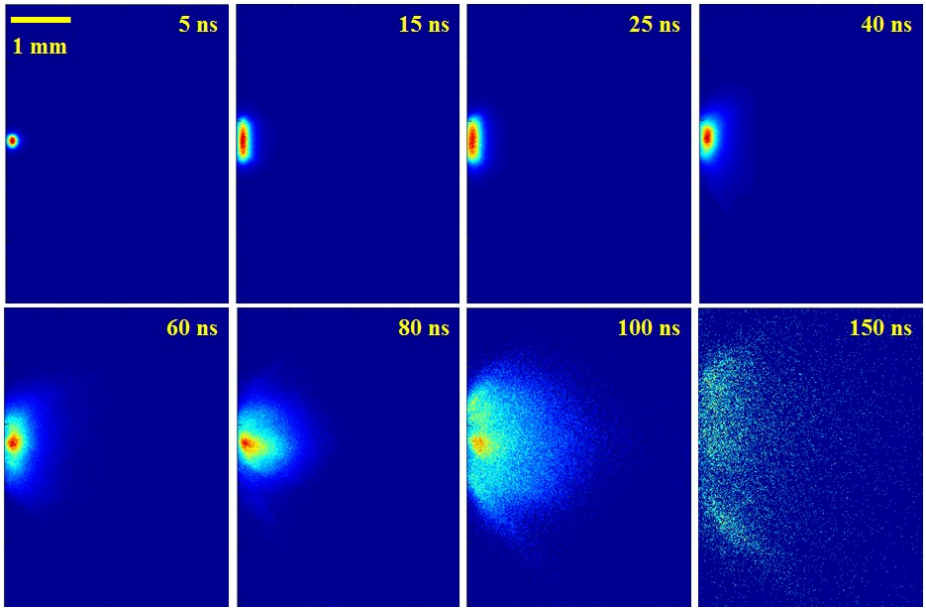

Fig. 4.1.1 – Time sequence of fast photography images showing the spatio-temporal evolution of the Al-Bulk plume at various delays.

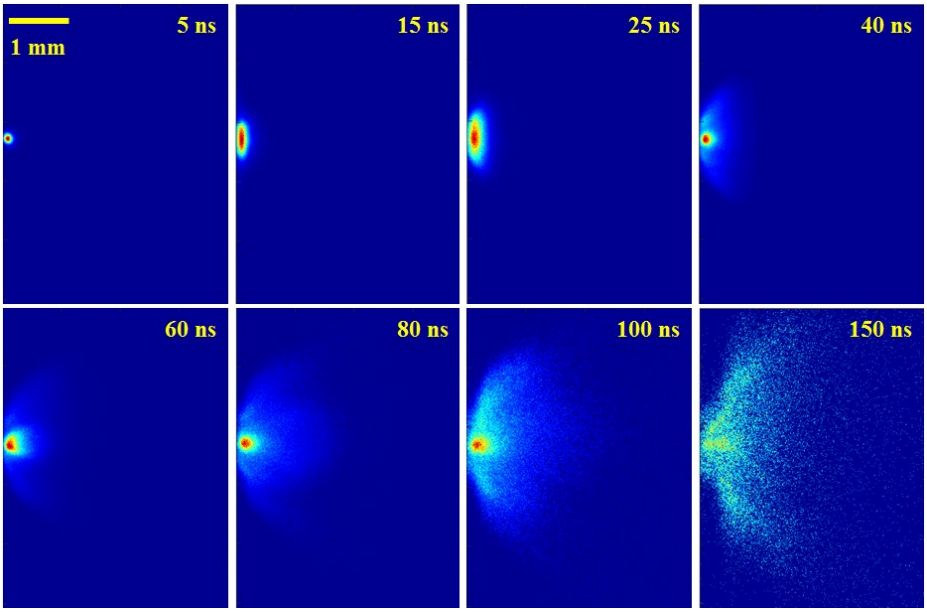

Fig. 4.1.2 – Time sequence of fast photography images showing the spatio-temporal evolution of the Co-Thin plume at various delays.

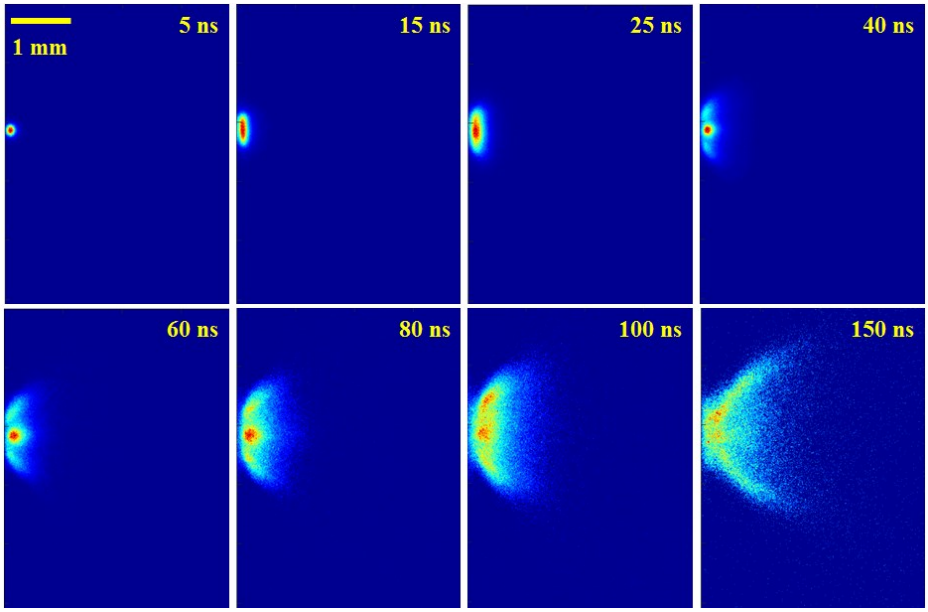

Fig. 4.1.3 – Time sequence of fast photography images showing the spatio-temporal evolution of the Fe-Thin plume at various delays.

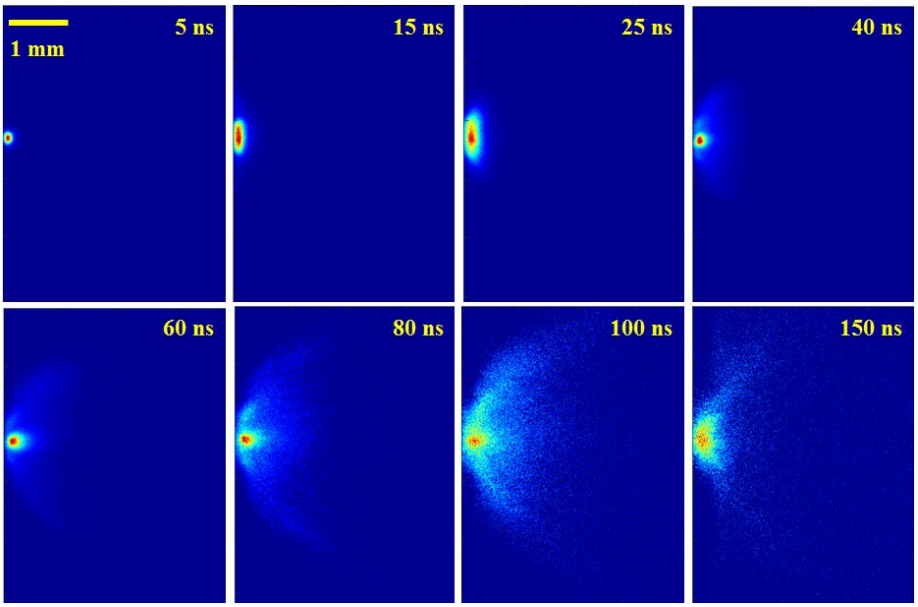

Fig. 4.1.4 – Time sequence of fast photography images showing the spatio-temporal evolution of the Ni-Thin plume at various delays.

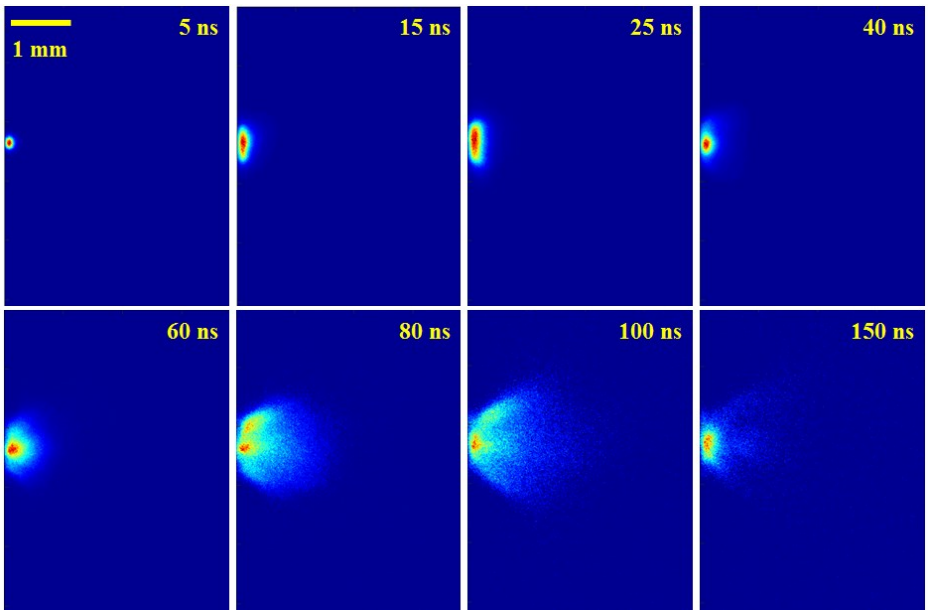

Fig. 4.1.5 – Time sequence of fast photography images showing the spatio-temporal evolution of the Ag-Thin plume at various delays.

Collisions inside the plasma play a major role in determining the spatio-temporal evolution: when the particle densities are high enough collisions induce the formation of a thermalization layer called Knudsen layer (KL) within a few mean free paths from the target surface, investigated by Kelly and others [91-93]. The formation of the KL results in stopped or backward moving material close to the target, as noticeable from fast photography image at 40 ns for all targets. The backward moving particles are either re-condensed or reflected from the target surface. The KL formation is followed by strongly forward peaked velocity distributions away from the target surface with an Unsteady Adiabatic Expansion (UAE) of the plasma.

Detailing the spatio-temporal evolution, Al-bulk and nanostructured targets show the same behavior in the first 40 ns. At early times, the plume front is spherical with a spot size of about 300 μ m; as time evolves, the plume front becomes sharpened and expands in height until to 40 ns.

After this time, the Al-bulk target expands with a duration of about 100 ns. Instead, at later time, nanostructured targets show internal structures, with a central region more dense and hotter and tails directed sideways at lower densities and temperatures, and the plume appears more confined. The lifetime of the plasma plume is found to be higher respect to Al-bulk plasma.

Plots of the emission intensity as a function of distance along the longitudinal expansion direction at different times provide a useful insight into the internal structures in the plume (Fig. 4.1.6 - Fig. 4.1.10).

For easier comparison, each profile has been normalized to its maximum intensity.

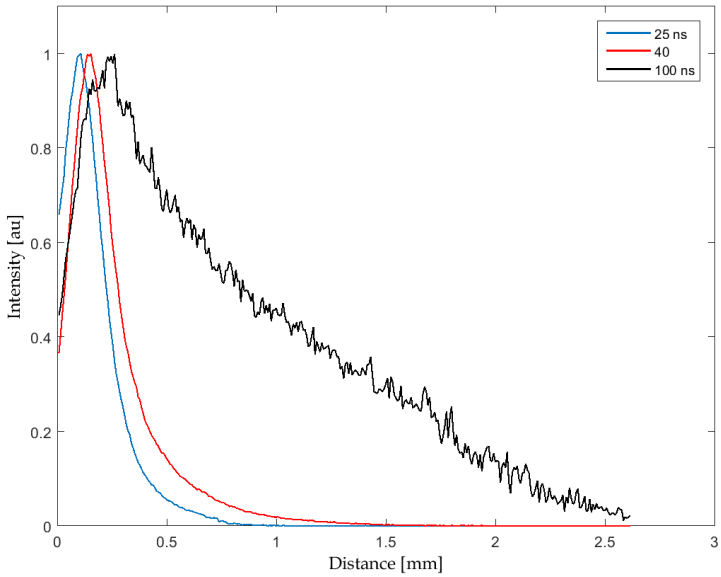

Fig. 4.1.6 – Intensity counts obtained from the ICCD images for various times during the evolution of the plasma for Al Bulk target.

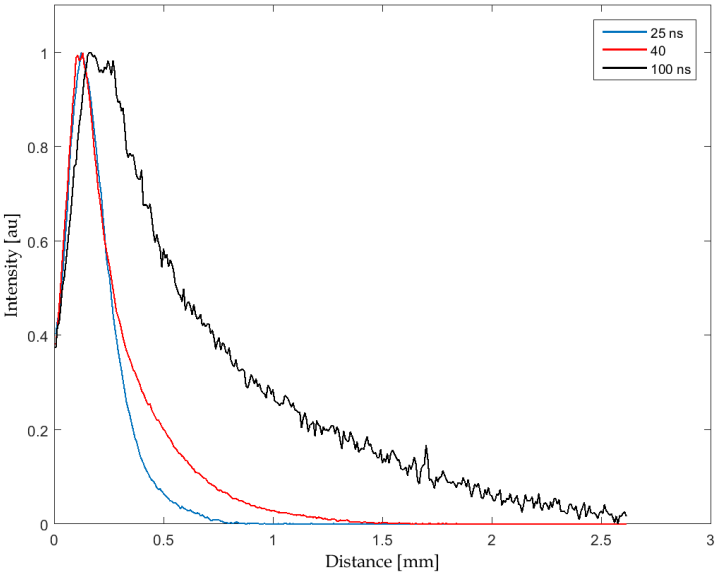

Fig. 4.1.7 – Intensity counts obtained from the ICCD images for various times during the evolution of the plasma for Co-Thin target.

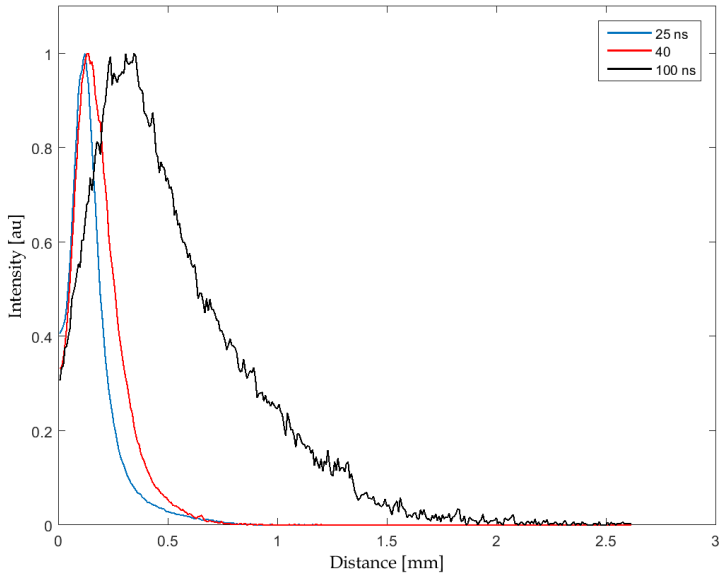

Fig. 4.1.8 – Intensity counts obtained from the ICCD images for various times during the evolution of the plasma for Fe-Thin target.

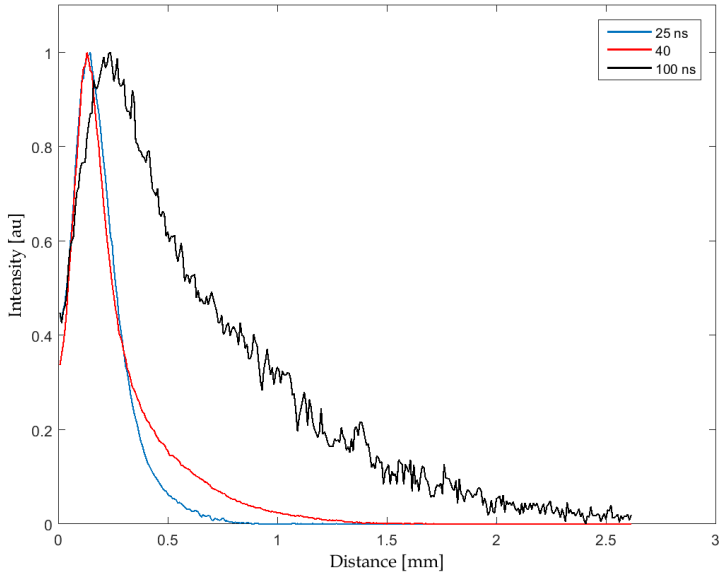

Fig. 4.1.9 – Intensity counts obtained from the ICCD images for various times during the evolution of the plasma for Ni-Thin target.

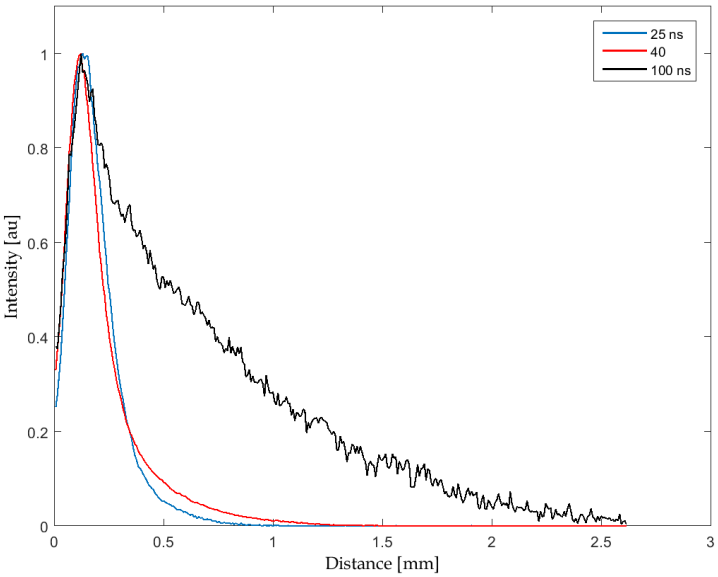

Fig. 4.1.10– Intensity counts obtained from the ICCD images for various times during the evolution of the plasma for Ag-Thin target.

The emission intensity profiles show a single peak distribution indicating uniform emission along the target normal. However, at higher delays, some nanostructured targets outline a double peak due to the hot central region and to the tails that expand laterally.

Moreover, increasing the delay, the center of mass shift away from the target.

In order to obtain a better understanding of the plasma expansion and evolution, position-time plots of the luminous front are created. In this way, it is possible to study the expansion velocity of the visible plasma plume, deduced from fit of the R-t plots.

Since the plasma imaging shows significant uncertainty in recording plume front positions, we consider its position based on a 90% reduction in the maximum intensity.

The R-t plots show a linear trend until about 40 ns, followed by a flat region, and finally, by increasing the temporal delay, the plume-front distance enhances again. This behavior reflects that observed in spatio-temporal evolution imaging.

At the same time, the flux obtained by integrating the visible image for each temporal delay and by normalizing for the exposure time was represented. An increasing of integral visible flux is highlighted where the R-t trend changes slope. This is further confirmation of the KL formation.

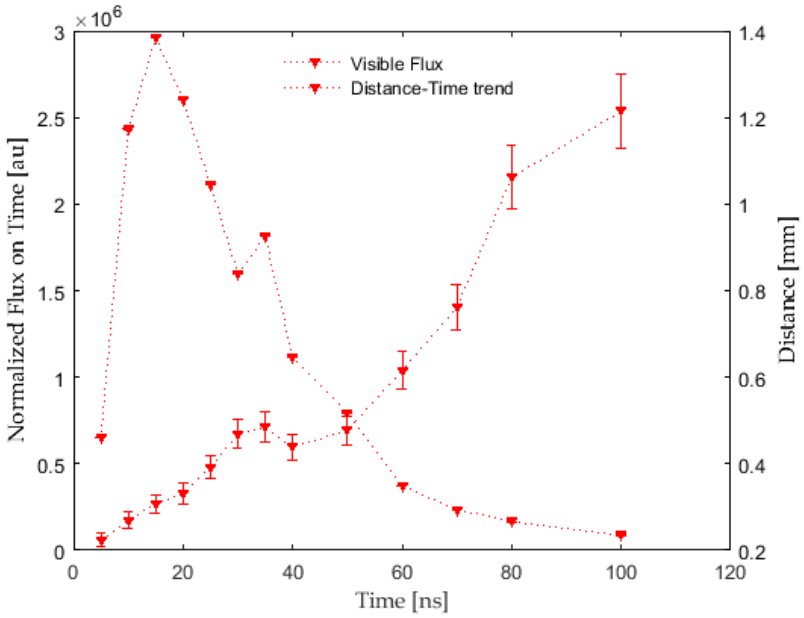

Fig. 4.1.11 – Position-time (R-t) and integral flux plots obtained from the ICCD images for Fe-Thin target.

Fig. 4.1.12 shows the R-t plots for all targets. One can separate the contribution due to the early times from that obtained at higher delays: for all targets, the plasma expansion velocity in the first region (slow component) is the same within the error, while it is different in the second region (fast component), as highlighted in Table 4.1.1.

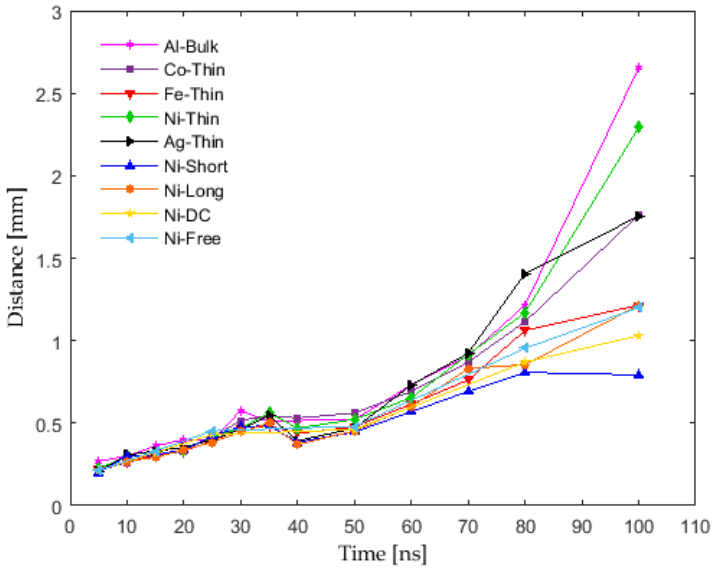

Fig. 4.1.12 –R-t plots for all targets.

Target	***Fast velocity [m/s]×10⁴***	***Slow velocity [m/s]×10⁴***
Al-Bulk	4.18±0.95	1.07±0.24
Co-Thin	2.42±0.30	1.14 ±0.15
Fe-Thin	1.56±0.23	0.93±0.09
Ni-Thin	3.54±0.67	1.04±0.11
Ag-Thin	2.45±0.25	0.99±0.10
Ni-Short	1.09±0.08	1.02±0.13
Ni-Long	1.42±0.12	0.95±0.07
Ni-DC	1.16±0.27	1.08±0.10
Ni-Free	1.45±0.95	1.19±0.04

Table 4.1.1 – Plasma expansion velocity obtained from the slope of linear line fit for each target.

These data confirm the observations of the imaging. The Al bulk target provides a slightly higher velocity than the nanostructured targets filled with different metals, whereas substantial differences are observed when compared with the velocity of the other nanostructured targets, for which the plasma evolves more slowly and has a longer life. This could be evidence of plasma stagnation, which implies a hotter and more dense plasma.

Detailed comparisons in relation to the geometry and to the deposition technique of the samples are given in section 4.5.

4.2. X-ray

The time integrated X-ray flux with appropriate spectral selection is employed in order to gather valuable physical information on laser-matter interaction process.

Fig. 4.2.1 shows a typical X-ray image taken by using a 10-channel pinhole-camera, which points out the effect of different filtering conditions: thinner absorbers have a higher flux than the larger thicknesses.

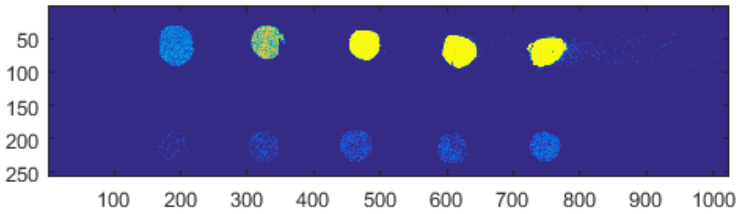

Fig. 4.2.1 – X-ray images of a plasma obtained simultaneously from a single shot by using a 10-channel pinhole-camera, where each channel indicates a different spectral region.

The X-ray signal was acquired over the entire duration of plasma because the X-ray pulse duration is comparable with that of the laser pulse producing the plasma [94, 95], while the minimum acquisition time for the detector is 10 μs.

The flux through each channel was estimated by selecting a Region Of Interest (ROI) with the same size for all channels.

Table 4.2.1 contains the mean X-ray flux for each absorber thickness considered.

Because Al absorbers are sensitive to certain photon energies, as shown in Fig. 3.3.3, the flux through a channel is the integral over the spectral region of the CCD sensor sensitivity (Fig. 3.3.1), with the effect of the filters. For this reason, in order to assign a spectral value to each channel, the deconvolution between the X-ray flux and the quantum efficiency curve of the CCD-camera is carried out.

In this way, it was possible to plot the X-ray flux as function of the extrapolated energy by 10% of the transmission curve for different thickness absorber, as can be seen in Fig. 4.2.2.

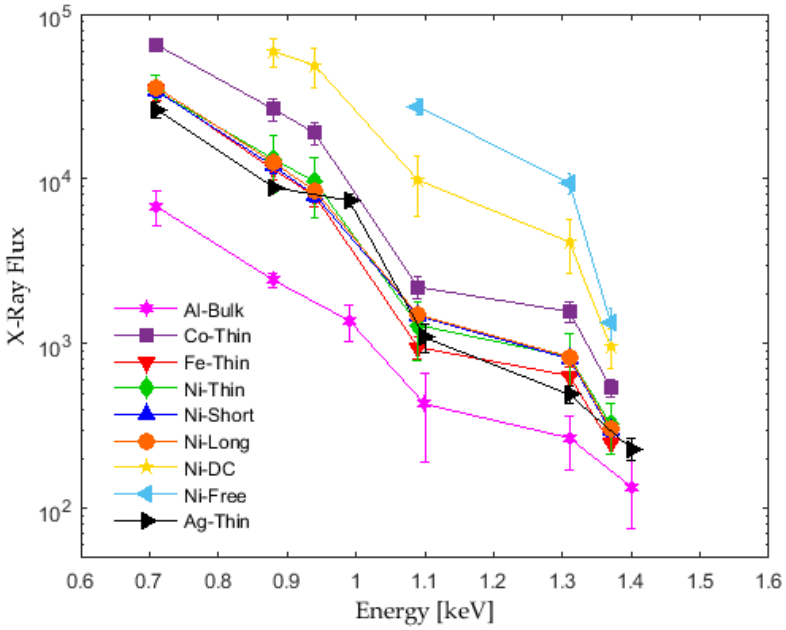

Fig. 4.2.2 – X-ray flux for all targets as function of the extrapolated energy by 10% of the transmission curve for different thickness absorber.

X ray flux [counts]×10²

Target	***Absorber Thickness [µm]***		
	3	***5***	***6***
Al-Bulk	62.5 ± 15.7	22.8±2.3	13.0 ± 3.5
Co-Thin	598.9 ± 46.7	248.9 ±42.1	178.7 ± 31.1
Fe-Thin	319.1 ± 45.7	107.3 ± 16.0	74.2 ± 10.9
Ni-Thin	313.2 ± 83.9	124.2 ± 49.5	90.4 ± 37.7
Ag-Thin	242.3 ± 27.1	83.6 ± 2.5	69.4 ± 6.4
Ni-Short	314.0 ± 32.8	112.4 ± 10.6	75.0 ± 7.1
Ni-Long	329.9 ± 33.1	118.3 ± 11.3	79.8 ± 8.2
Ni-DC	Sat.	558.1 ± 122.0	460.1 ± 132.2
Ni-Free	Sat.	Sat.	Sat.
Target	***Absorber Thickness [µm]***		
	9	***15***	***17***
Al-Bulk	4.1 ± 2.4	2.5 ± 0.9	1.2 ± 0.6
Co-Thin	20.9 ± 3.3	14.7 ± 2.3	4.8 ± 0.6
Fe-Thin	9.0 ± 1.4	6.0 ± 0.9	2.2 ± 0.3
Ni-Thin	12.3 ± 5.1	7.8 ± 3.1	2.9 ± 1.1
Ag-Thin	10.3 ± 2.1	4.6 ± 0.6	2.0 ± 0.4
Ni-Short	14.0 ± 1.1	7.6 ± 0.6	2.96± 0.2
Ni-Long	14.2 ± 1.1	7.8 ± 0.6	2.7 ± 0.2
Ni-DC	93.3 ± 39.2	38.9 ±14.9	8.6 ± 2.6
Ni-Free	259.9 ± 30.3	88.2 ± 12.6	12.2 ± 0.3

Table 4.2.1 – X-ray flux for each absorber and for each target.

First, it is reasonable to say that, for every target, X-ray energies greater than 1.3 keV can be reached. Moreover, for all nanostructured targets, the X-ray flux is higher than that of Al-bulk target. About that, some considerations are necessary: the relative yield due to three main processes responsible for the X-ray emission from plasmas, as discussed in section 2.2, depends upon the atomic number Z of the target material.

For medium values of the atomic number ($Z \leq 20$, as Al-bulk target), the plasma produced is predominantly populated by H-like through Be-like ions. In these conditions, a single emission line can carry a significant fraction (a few %) of the total X-ray emission energy between 0.5 and 10 keV. Due to the sharpness of emission lines ($\Delta \upsilon / \upsilon \approx 10^4$), their intensity can overcome continuum emission by several orders of magnitude.

When high Z targets materials ($Z \geq 20$, as nanostructured targets) are used, the plasma is populated by ions with several bound electrons. The resulting spectrum consists of a complex series of emission lines, typical of many-electron systems. The density of emission lines in the spectrum is so large that they merge, giving rise to a quasi-continuum emission.

According to the preceding discussion, the X-ray conversion efficiency is also found to strongly depend upon the target atomic number.

Fig. 4.2.3 shows the total X-ray yield between 0.7 and 20 keV and the conversion efficiency (in % of the laser energy) for plasmas produced from different Z targets in conditions similar to those used in this work: the plasma was generated by 8ns Nd:Glass laser pulses focused in a 100μm diameter focal spot at an intensity of 4×10^{13} W/cm^2 [96].

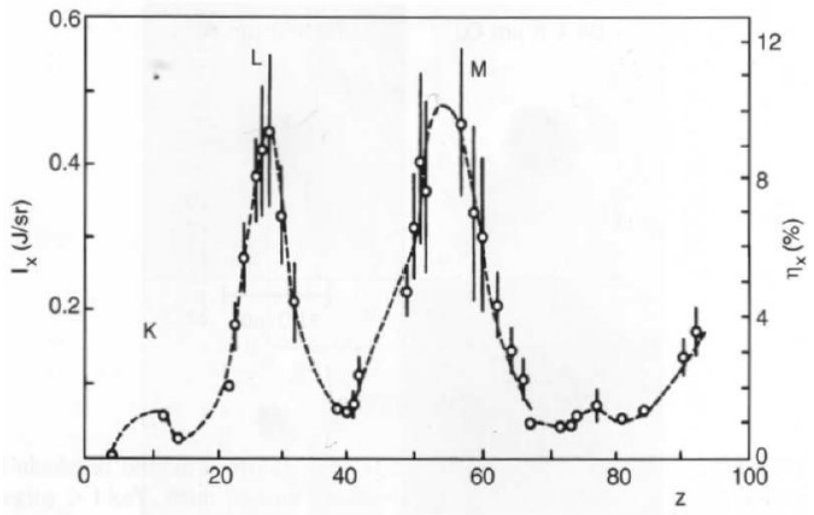

Fig. 4.2.3 – Yield of x-ray emission between 0.7 keV and 20 keV as a function of the atomic number of the irradiated target. Maxima of emission are measured when the atomic configuration is optimum for the excitation of resonance lines from K-, L- and M shells [96].

The emission exhibits four maxima as the atomic number of the target is progressively increased from Z=4 (Beryllium) through to Z=92 (Uranium). The physical reason of this characteristic behavior is that, as the Z of the target increases for fixed interaction conditions, the atomic configuration is optimum for the generation of resonance line emission from the K-, L-, M- and N-shells. In general, the behavior of the X-ray yield as a function of the atomic number depends upon the considered spectral range because the contribution of resonance emission from different shells lies in different regions of the spectrum for different atomic numbers.

Therefore, the comparison between bulk aluminum and nanostructures filled with different metals could be explained in relation to different chemical composition, even if it is important to take into account that, in the nanostructured targets, only 10-15% of the oxide layer is filled with metal.

Moreover, another feature to point out is that the nanostructure surface is dark, then is much less reflective than Al-bulk. Consequently, this could lead to a higher X-ray flux for nanostructured targets.

In the light of these considerations, the differences in X-ray fluxes can be explained. However, targets with the same atomic number (namely Ni), but different geometry and deposition technique, produce different amounts of X-ray flux. In section 4.5, details on X-ray flux trends by varying the nanostructure parameters will be given.

4.3. Time of flight measurements

The time of flight (TOF) measurements provide excellent technique to determine the velocity distribution of the plasma. The TOF profiles as a function of distance from the target surface were investigated.

An example of TOF ion profile obtained by placing the probe closest to the target surface for a Co nanostructured target is shown in Fig. 4.3.1

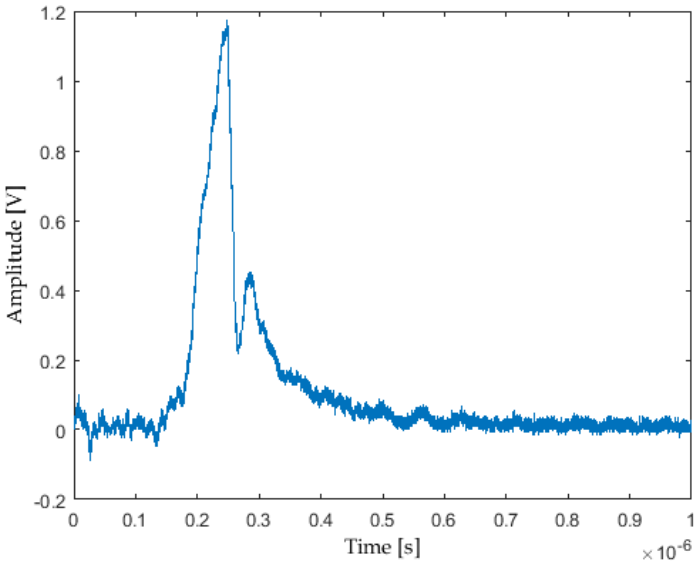

Fig. 4.3.1 – Time of flight ion signal obtained for ToF closest from Co-Thin target.

. The time of flight signal exhibits a double peak structure, associated to that observed by fast imaging. Therefore, emitted ions may be divided into two groups: fast ions and slow ions.

However, from ion profile of farthest TOF to the target surface, the double peak structure disappears, as shown in Fig. 4.3.2, because the probe is not be able to distinguish particles in flight with different velocities. Indeed, the peak ion velocity of the far probe is intermediate between the fast and slow peak velocities of the near ToF.

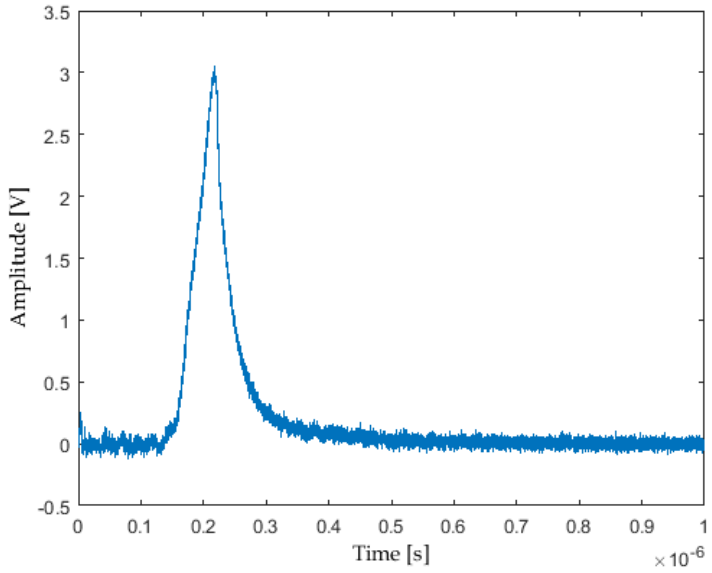

Fig. 4.3.2 – Time of flight ion signal obtained for ToF farthest from Co-Thin target.

The peak of each profile corresponds to the maximum probable arrival time of ion flux into the collector. Therefore, the velocities of ions in near and far ToF was estimated for all targets, as listed in Table 4.3.1 -Table 4.3.2.

Ions at very large distances evolve with velocities higher than those estimated from plume expansion in the visible (on the order of 10^4 m/s).

Target	*Fast ion velocity [m/s]×10^5*	*Slow ion velocity [m/s]×10^5*
Al-Bulk	3.84 ± 0.26	3.38 ± 0.22
Co-Thin	3.96 ± 0.26	3.40 ± 0.23
Fe-Thin	3.81 ± 0.25	3.24 ± 0.22
Ni-Thin	3.83 ± 0.25	3.36 ± 0.22
Ag-Thin	3.59 ± 0.24	3.25 ± 0.22
Ni-Short	3.95 ± 0.26	3.40 ± 0.23
Ni-Long	4.03 ±0.27	3.43 ± 0.23
Ni-DC	4.10 ± 0.27	3.50 ± 0.23
Ni-Free	3.93 ± 0.26	3.56 ± 0.24

Table 4.3.1 – Fast and slow component of ion velocity of near-ToF.

Target	*Ion velocity [m/s]×10^5*
Al-Bulk	3.54 ± 0.11
Co-Thin	3.74 ± 0.12
Fe-Thin	3.59 ± 0.11
Ni-Thin	3.66 ± .011
Ag-Thin	3.33 ± 0.10
Ni-Short	3.71 ± 0.12
Ni-Long	3.77 ± 0.12
Ni-DC	3.72 ± 0.12
Ni-Free	3.59 ± 0.11

Table 4.3.2 – Ion velocity of far-ToF.

The velocities for all targets are equal within the uncertainty; this means that the ToF are quite far from the target for which the plasma expand freely.

4.4. Morphological analysis

Most observed craters have a sharp circular shape, with diameters ranging between 150 and 180 μm. A crater's depth (measured at the deepest point) is, in most cases, greater than its radius but a little smaller than its diameter (the exception being Al-Bulk, which has greater radius than depth). The crater bottom is hemispherical in general shape, but often displays a structure called "channel", (see Fig. 4.4.1) a straight narrow indentation, resembling a knife cut, which begins at the center of the crater and points downward, toward the same direction as the parallel component of the incoming laser beam.

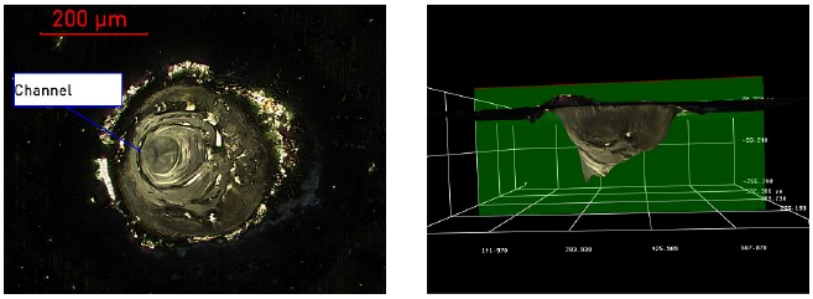

Fig. 4.4.1 – The channel structure, common in craters of all targets, seen from top (left) and side (right). As can be seen, the channel is a strongly asymmetric deep indentation in a mostly hemispheric crater. In this image, the laser beam arrived from the right.

This structure is certainly related to the inclination of the incoming laser beam, but surprisingly it is usually much more narrow (few tens of μ m) than the spot size of the beam, so it seems unlikely to be a direct consequence of the spatial distribution of laser intensity. While its exact origin is unsure, optical observation led to hypothesize that it originates from a rapid cooling of convection patterns at the crater bottom.

Since the advantage of nanostructured materials compared to bulk aluminum lies in the volumetric heating of matter, it was decided to simply measure depth and volume of the craters. They have been measured in the following way:

- ***Depth***: one chooses a line along which the crater's depth profile will be measured. The line was parallel to the laser beam direction and passing through the point of maximum depth. Since surface outside the crater is quite flat (within two μm) for all considered targets, depth is simply calculated as the height difference between a point well outside the crater (in order to exclude local swelling and other near-crater features) and the deepest point of the crater.
- ***Volume***: a 2D measurement region and a reference level were defined to measure the volume. Reference level is taken at the surface, while the 2D region was defined simply selecting a circle a few tens of μm wider than the crater in order to avoid ambiguities in the exact criteria for crater edge definition.
  Empty volume will be calculated below the reference level, and only in the selected region.

In the following table, depth and volume data from all the irradiated targets are presented [97].

Target	*Depth [μ m]*	*Volume [μ m^3 / 10^6]*
Al-bulk	139±3	3.67±0.13
Co-Thin	184±3	4.52±0.05
Fe-Thin	171±4	3.39±0.09
Ni-Thin	160±3	3.99±0.08
Ag-Thin	145±3	4.40±0.20
Ni-Short	180±4	4.67±0.05
Ni-Long	203±10	5.32±0.24
Ni-DC	189±4	4.20±0.07
Ni-Free	172±10	3.69±0.24

Table 4.4.1– Average depth and value of craters for each target.

As expected, of all considered targets Al-Bulk has the lowest mean value for crater depth. It also has a lower crater volume compared to most targets, exceptions being the iron NWs target and the freestanding NWs target, due to lower crater radius in those targets. Moreover, greater volume does not necessarily imply greater plasma production, since matter can be removed at liquid or gaseous state.

4.5. Discussion of results

Targets with different parameters were developed at the INFN nanotechnology lab in Bologna in order to investigate the LPP behavior and to understand by means of which metals and geometries is achieved a more hot and dense plasma.

Targets were compared with each other in terms of:

- ***NWs metal***: three targets with similar atomic number (Ni-Thin, Co-Thin and Fe-Thin) and a target with larger atomic number (Ag-Thin) were prepared to study the different response to irradiation;
- ***NWs diameter***: for this comparison, oxalic acid (Ni-Long target, 50 nm diameter) and sulphuric acid (Ni-Thin target, 20 nm diameter) have been used.
- ***NWs length***: NWs of different length have been grown on the same target by rising it partly out of the solution during electrodeposition. In this way, two regions with NWs 5 and 10 μm long have been obtained (Ni-Short and Ni-Long), with every other parameter being equal.
- ***Electrical contact***: in order to study the effect of the absence of oxide layer between the NWs bottom and the aluminum substrate, a single target with contacted NWs (Ni-DC) has been produced and compared with Ni-Long target, which is AC produced and has similar other parameters.
- ***NWs confinement***: for DC targets, the alumina layer can be partially dissolved by a chemical attack without destroying the NWs. In order to study the role of alumina in the laser-target interaction, it has been dissolved leaving "freestanding" NWs in target Ni-Free and was compared with the confined ones.

4.5.1. Comparison between NWs metals

Comparisons of ablation depth, plasma expansion velocity from optical fast imaging and from ToF measurements for nanostructured targets filled

with different metals are shown in Fig. 4.5.1. In order to collate different diagnostics, each data set is normalized to its maximum.

From morphological analysis, it has been found that craters in Co are the deepest and greatest in volume; they are about 15% larger than in Fe, Ni and Ag, indicating that most of the volume gain is due to deeper ablation, with little difference in crater radius.

Comparing the plasma expansion velocity for the different metals turns out that Fe, Co and Ag expand slower than Ni. In particular, the lowest velocity is obtained for Fe-Thin target; the reasons for this is that, observing the spatio-temporal evolution images, plasma produced by interaction with Fe target expands more in radial direction rather than longitudinal direction. Furthermore, the craters in Fe have the smallest radius among all targets.

Concerning the ToF, no differences are observed depending on the metal.

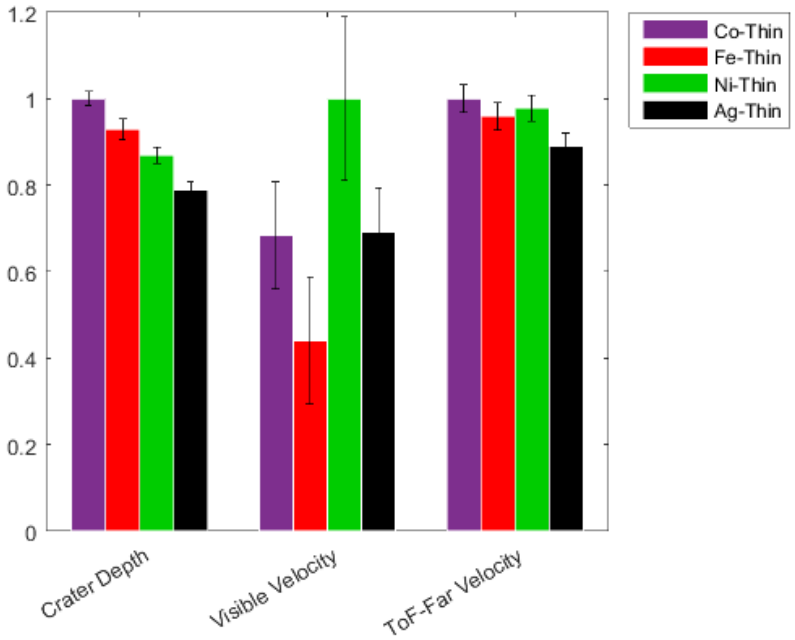

Fig. 4.5.1 – Comparison of ablation depth and plasma expansion velocity estimated by visible and ToF diagnostics for nanostructured targets filled with different metals, each normalized to its maximum.

Then, visible and X-ray fluxes were compared in order to investigate their behavior depending on metal nanowires, as shown in Fig. 4.5.2 -Fig. 4.5.3.

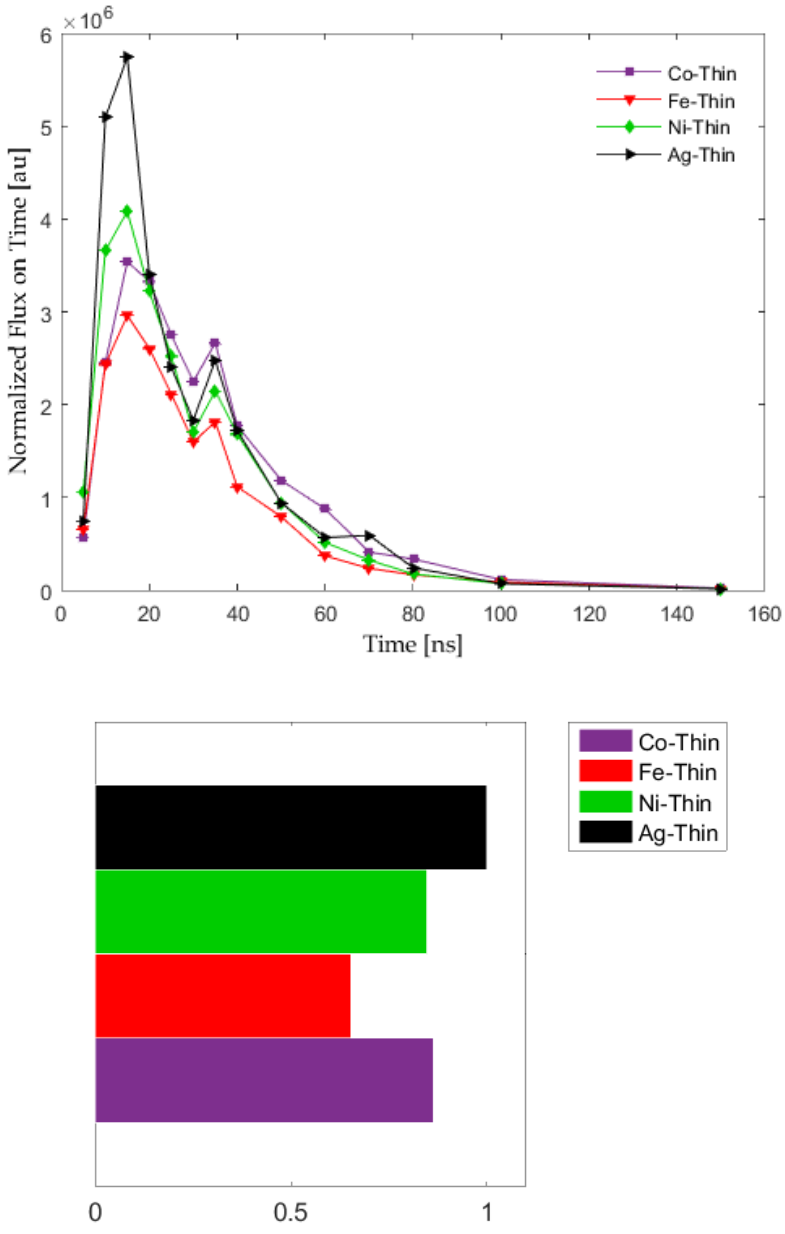

Fig. 4.5.2 – Visible flux as function of time (up) and integrated flux over the time (down) for nanostructured targets filled with different metals.

Excluding the behavior of Fe, one can be observe that the Ag has the higher visible flux than other targets, while Co and Ni are comparable with each other.

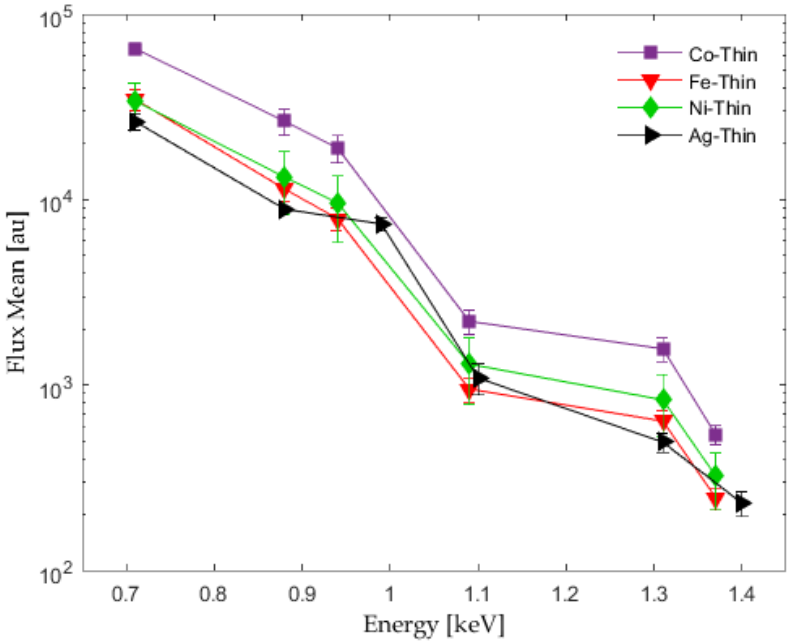

Fig. 4.5.3 – X-ray flux for nanostructured targets filled with different metals as function of the extrapolated energy by 10% of the transmission curve for different thickness absorber.

Conversely, the X-ray flux of Co, for all absorbers, is about twice than that of the other metals, which are comparable.

The results obtained for visible and X-ray flux are consistent between them: for a given nanostructured material, smaller optical fluxes correspond to larger X-ray fluxes, which implies that the spectral energy of the plasma is shifted towards larger energies, namely in EUV and X-ray domains. The apparent differences can be ascribed at the different craters morphology.

Co target seems to be, eventually, the better metal for further investigations.

4.5.2. Comparison between NWs diameter

The targets chosen for this comparison were Ni-Thin (sulphuric, ~20 nm) and Ni- Long (oxalic, ~50 nm). It should be noted that Ni-Long has a thicker alumina layer compared to Ni-Thin, which could affect the reliability of the comparison.

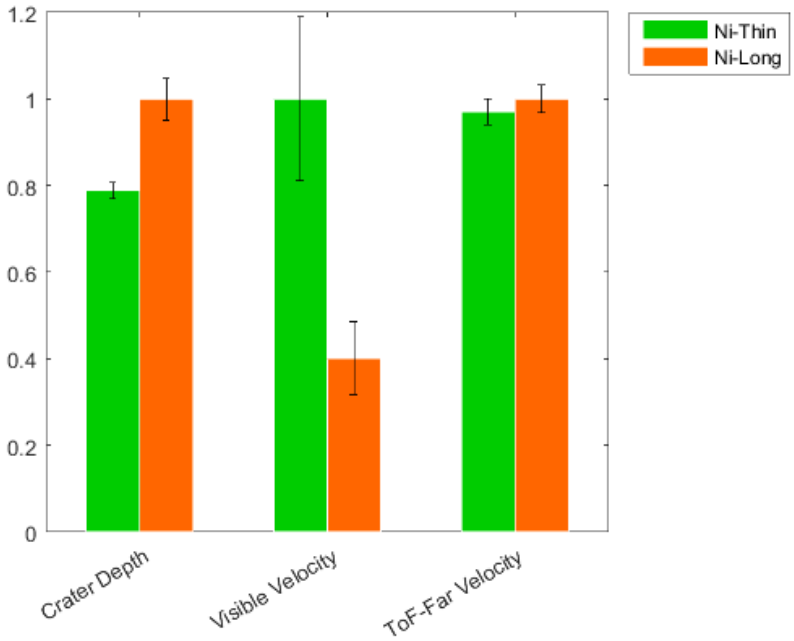

Fig. 4.5.4 – Comparison of ablation depth and plasma expansion velocity estimated by visible and ToF diagnostics for targets with different NWs diameter, each normalized to its maximum.

As can be seen in Fig. 4.5.4, morphological data show a considerably larger depth for craters in Ni-Long. According to these results, visible plasma expansion analysis shows a velocity for Ni-Thin almost two times greater than the Ni-Long ones. It means that plasma created at greater depths expands more slowly, thus resulting stagnant.

While from ToF investigations no difference are deduced, velocities are equal within uncertainty.

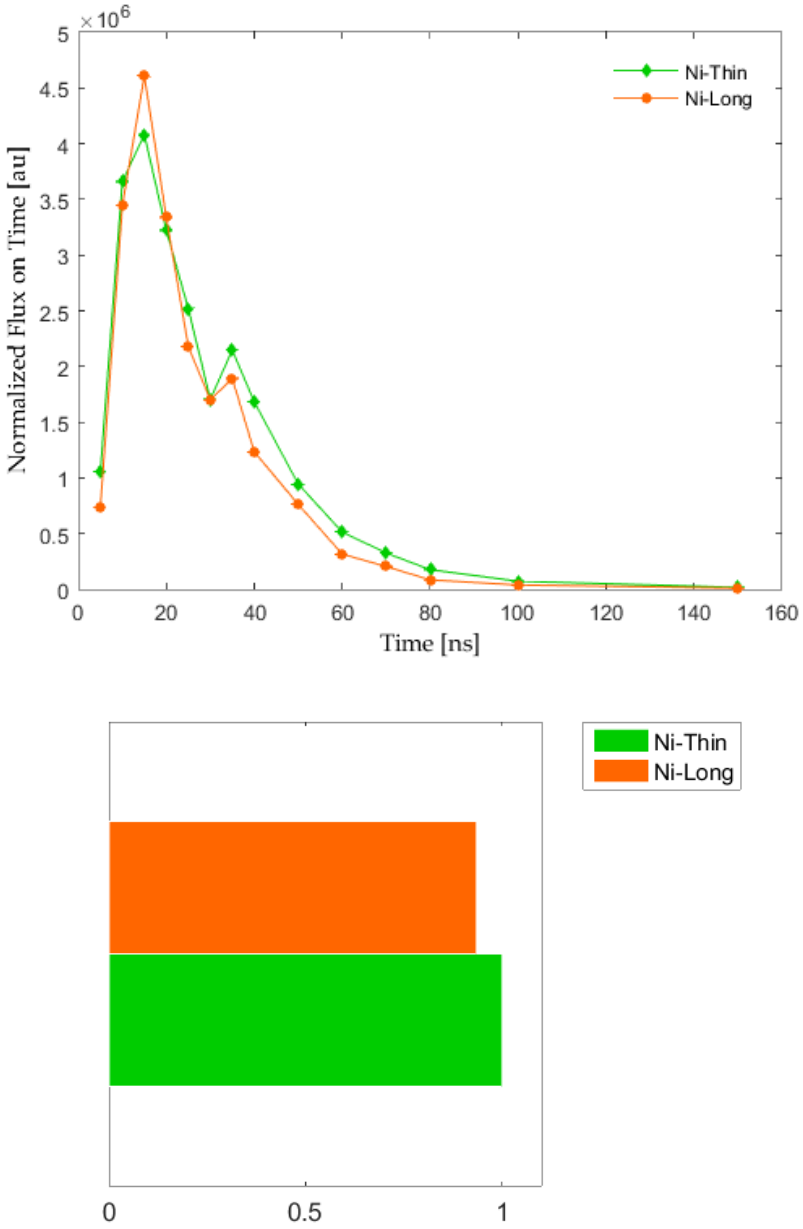

Fig. 4.5.5 – Visible flux as function of time (up) and integrated flux over the time (down) for targets with different NWs diameter.

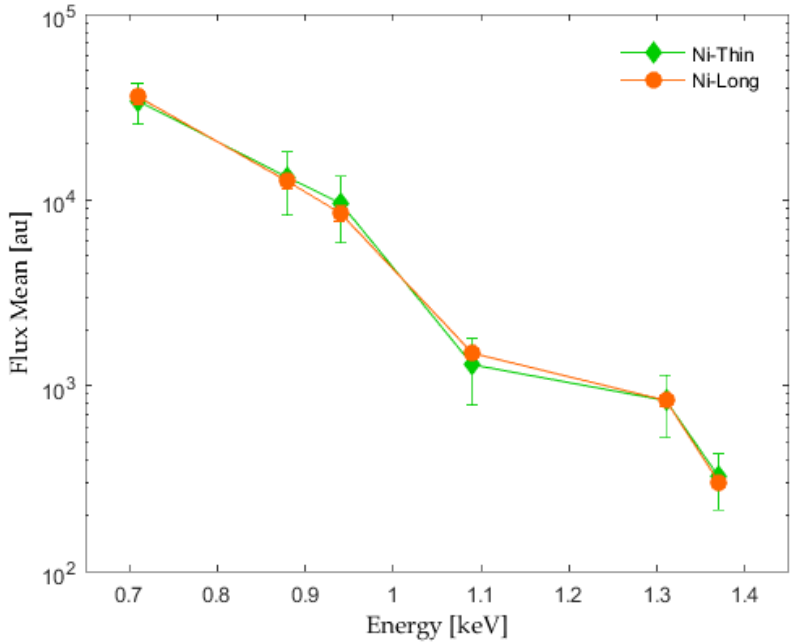

Fig. 4.5.6 –X-ray flux for targets with different NWs diameter as function of the extrapolated energy by 10% of the transmission curve for different thickness absorber.

Both in optical and in X-ray flux comparison, no difference are evident, fluxes are equal within uncertainty.

Although the craters analysis and plasma expansion velocity could lead to hypothesize that nanostructured targets with bigger diameter are more suitable to form hotter and denser plasmas, the results derived from visible and X-ray fluxes are in disagreement with the above. One possible explanation for these discrepancies could be correlated to the resonance effect: since has been demonstrated that transmission of light through nanowires arrays has resonant peaks for wavelength multiple of the array period (namely interpore distance in our case, which is linked with NWs diameter), the oxalic geometry might be closer to resonance conditions compared to that sulphuric.

4.5.3. Comparison between NWs length

For NWs length comparison targets Ni-Short and Ni-Long are used.

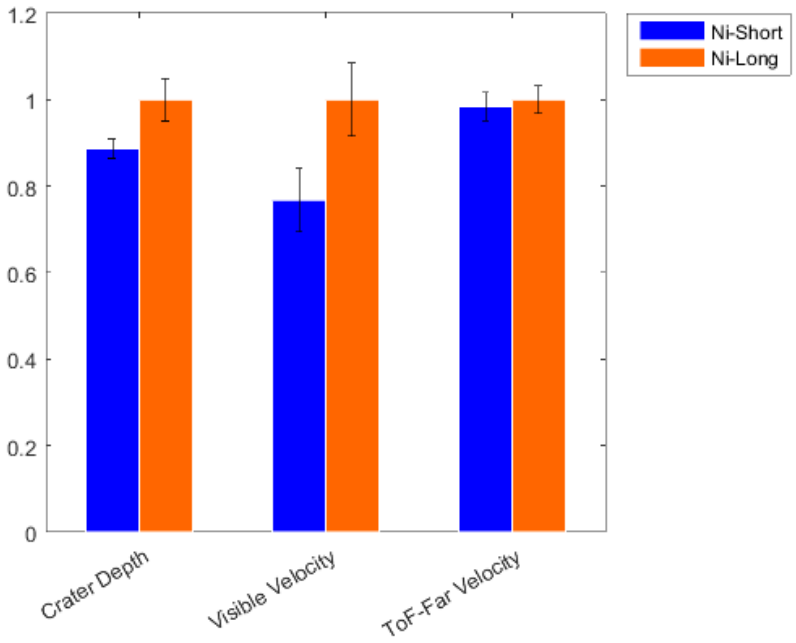

Fig. 4.5.7 – Comparison of ablation depth and plasma expansion velocity estimated by visible and ToF diagnostics for targets with different NWs length, each normalized to its maximum.

Even for nanostructured targets with different length, morphological data show an increase in depth for craters in Ni-Long. While visible plasma expansion analysis shows a velocity for Ni-Short smaller than the Ni-Long ones. This could be related to the spatio-temporal evolution, which, as for Fe, shows a plasma that expands mainly in radial direction, hence is 'more' confined in longitudinal direction.

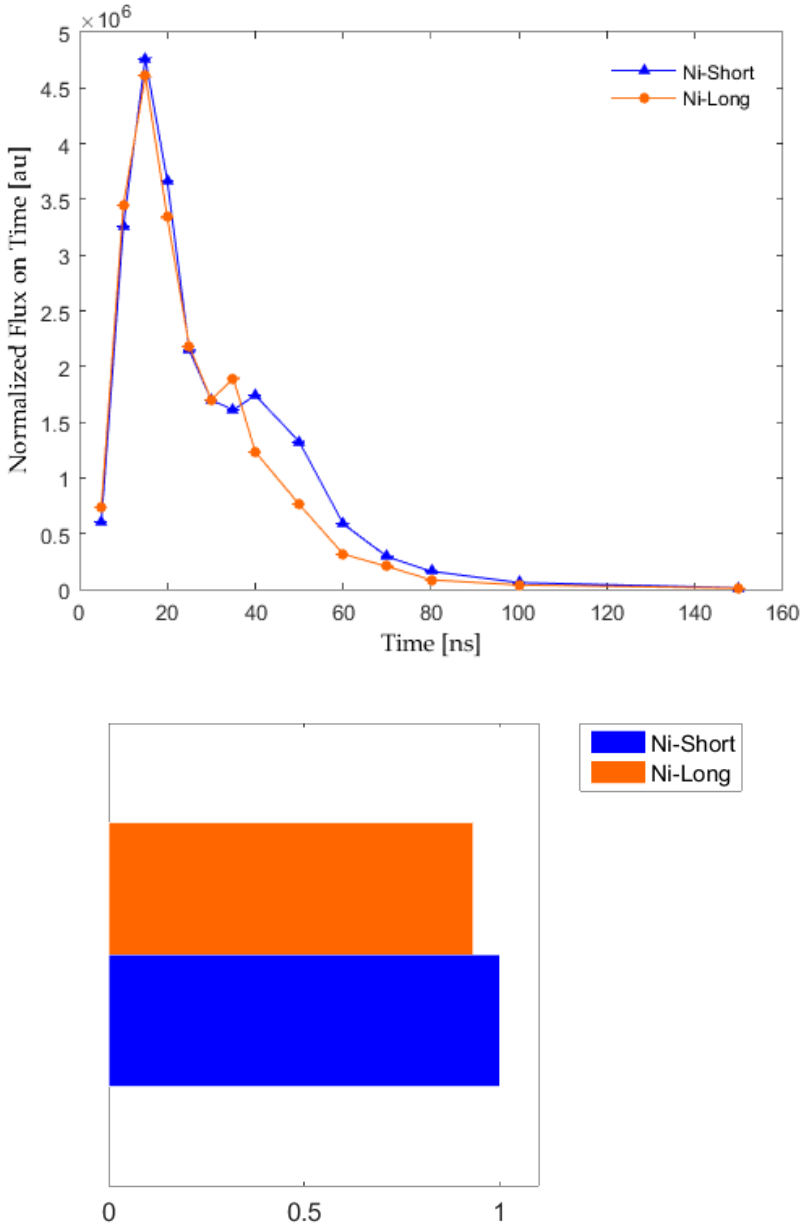

Fig. 4.5.8 – Visible flux as function of time (up) and integrated flux over the time (down) for targets with different NWs length.

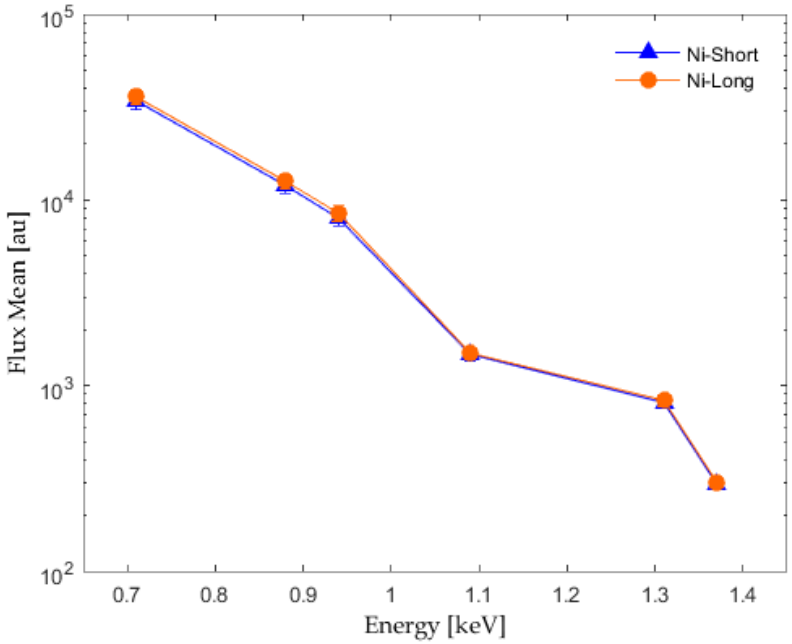

Fig. 4.5.9 – X-ray flux for targets with different NWs length as function of the extrapolated energy by 10% of the transmission curve for different thickness absorber.

From comparison of both optical and X-ray flux no difference between lengths of NWs target are deduced.

Therefore, nanowires length is not of relevant importance for the production of a plasma adapted for nuclear astrophysics studies.

4.5.4. Comparison between AC and DC deposition

AC/DC comparison is based on targets Ni-DC and Ni-Long, that have identical nominal parameters (~50 nm diameter, 10 μm long NWs). To change is the deposition technique: target Ni-DC has been fabricated via direct current electrodeposition, instead of alternate current like all the other targets. Therefore, for DC target, there is no continuous oxide layer between the base of NWs and the aluminum substrate, which means that NWs are in electrical continuity with the metal substrate.

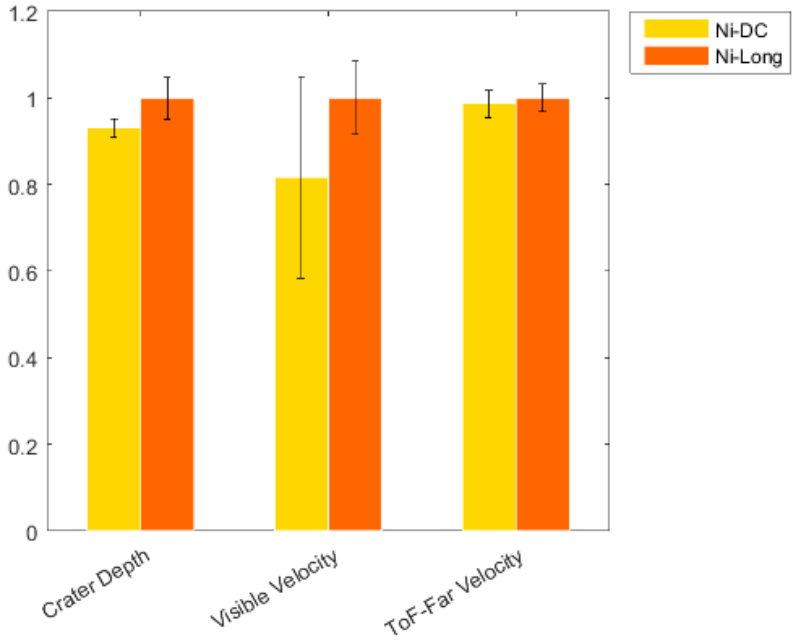

Fig. 4.5.10 – Comparison of ablation depth and plasma expansion velocity estimated by visible and ToF diagnostics for targets with different deposition techniques, each normalized to its maximum.

Differences of craters depth and plasma expansion velocity between the targets are below uncertainty, as shown in Fig. 4.5.10. The expansion of Ni-DC plasma proceeds more slowly than Ni-Long plasma, but is not statistically significant.

Nevertheless, enormous differences are highlighted in terms of both visible and X-ray flux in agreement to each other: while optical flux of Ni-DC target is five times smaller (Fig. 4.5.11), the X-ray measurements show a flux five times higher than Ni-Long target (Fig. 4.5.12).

Therefore, DC deposition seems a promising approach for future targets.

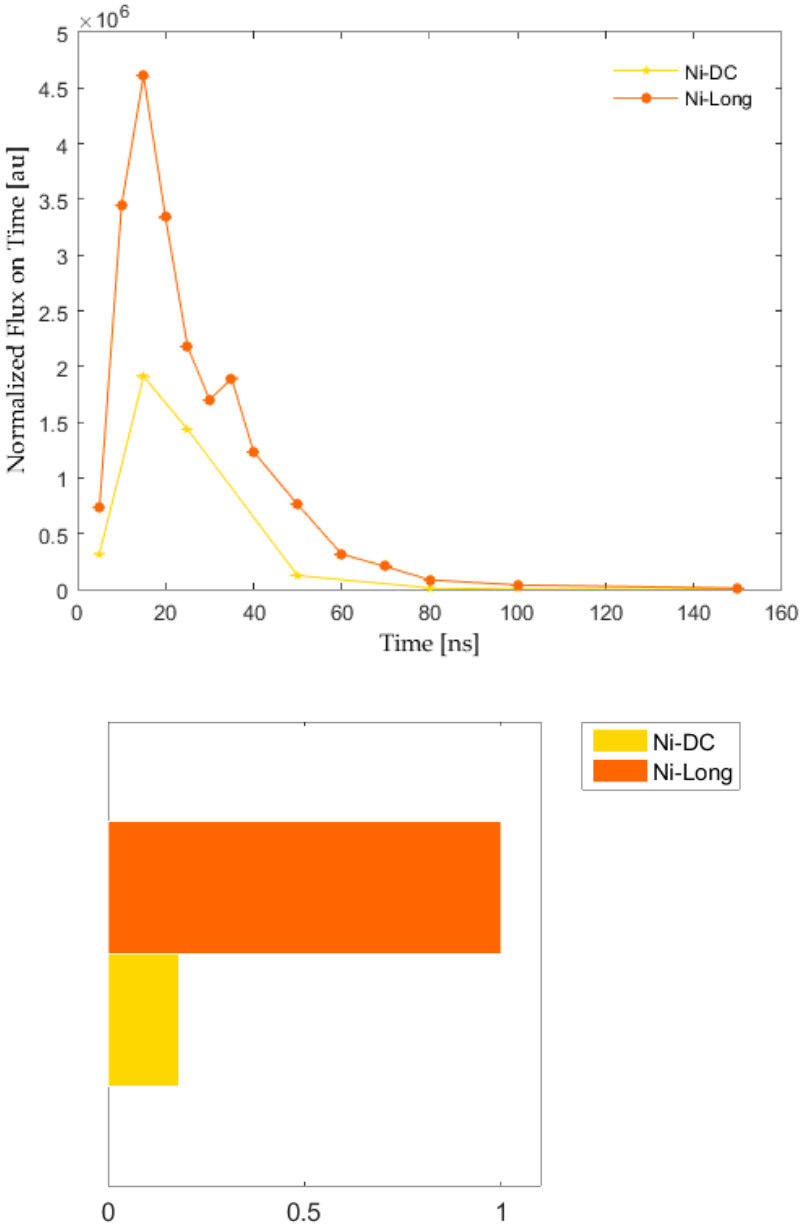

Fig. 4.5.11 – Visible flux as function of time (up) and integrated flux over the time (down) for targets with different deposition techniques.

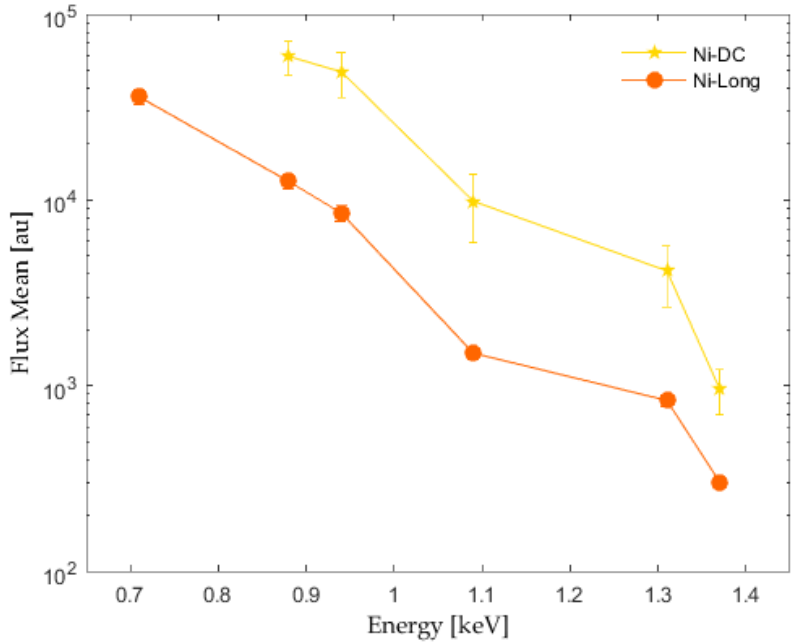

Fig. 4.5.12 – X-ray flux for targets with different deposition techniques as function of the extrapolated energy by 10% of the transmission curve for different thickness absorber.

4.5.5. Comparison between Confined and Freestanding NWs

Ni-DC and Ni-Free are compared to study the effect of the alumina layer on laser-target interaction. Since Ni-Free target has been obtained by chemically removing alumina on the same physical sample of Ni-DC, except for confinement, the two targets are identical.

As shown in Fig. 4.5.13, confined craters show a slightly larger (not statistically significant) depth and much larger volume. Free NWs craters have smaller volume compared to any other sample. This is probably due to the reduced thermal conduction and shockwave propagation in absence of the alumina matrix.

Data from visible expansion velocities show that plasma produced by laser interaction with Ni-DC target expands slowly than Ni-Free plasma, which, however, has a large uncertainty due to the limited data available.

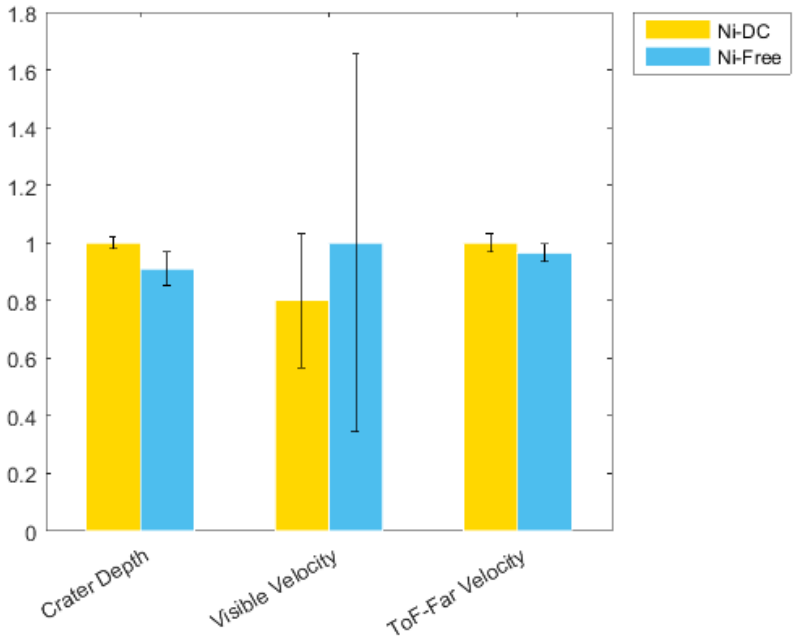

Fig. 4.5.13 – Comparison of ablation depth and plasma expansion velocity estimated by visible and ToF diagnostics for confined and freestanding NWs, each normalized to its maximum.

Comparison of visible fluxes emphasizes that a large amount of plasma is produced in laser - Ni-Free target interaction, about two-and-a-half times respect to Ni-DC.

Conversely, X-ray data show a flux much higher (of about a factor 2) for the free NWs target, compared to the flux of the confined NWs region. The first three thicknesses of Al-absorbers in Ni-Free are saturated; therefore, this target produces by far the highest X-ray flux in any target tested. Although this is an interesting result, it should be considered that the almost complete

lack of oxide layer in the free NWs region is very likely to lead to a higher measured flux due to a reduced self-shielding.

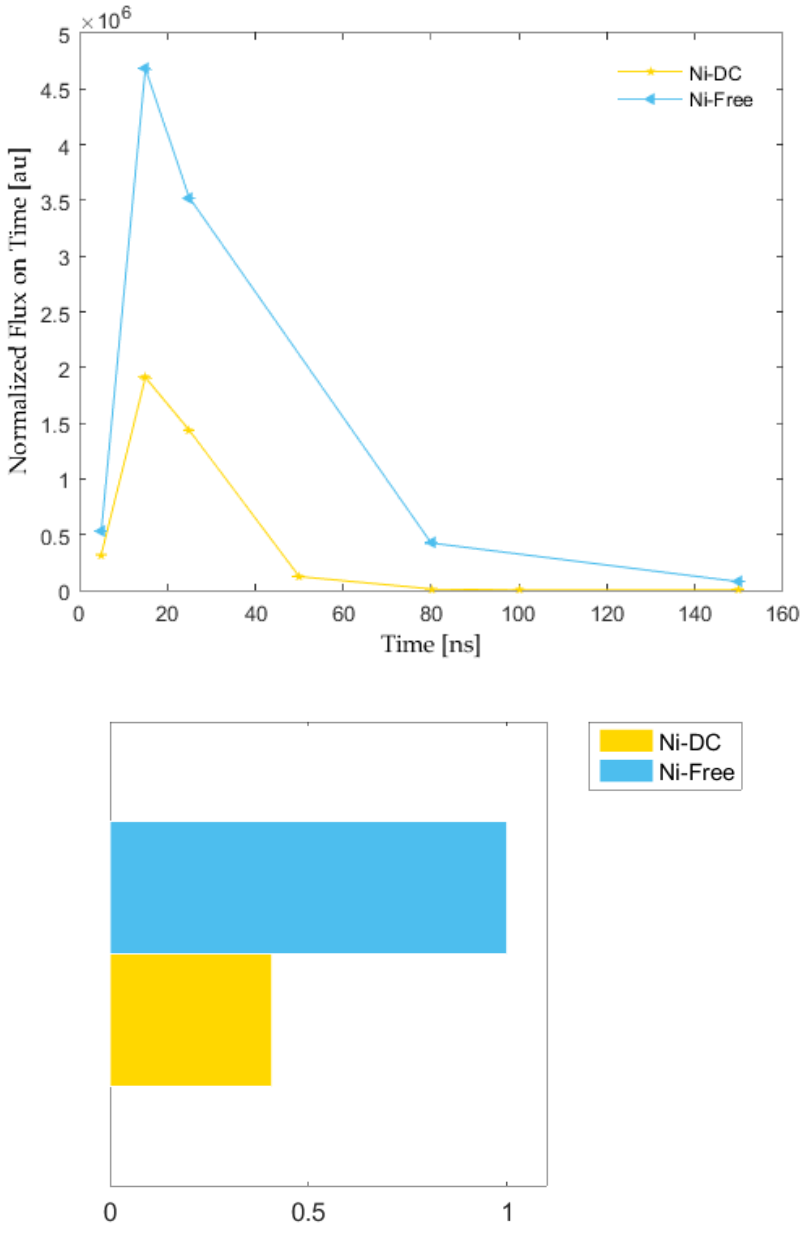

Fig. 4.5.14 – Visible flux as function of time (up) and integrated flux over the time (down) for confined and freestanding NWs.

From a target production point of view, it is not yet clear if freestanding NWs are a more attractive target for plasma production compared to confined ones, but the high X-ray flux is promising, and understanding the differences between freestanding and confined nanowires could lead crucial insight on the role of the oxide layer in plasma formation.

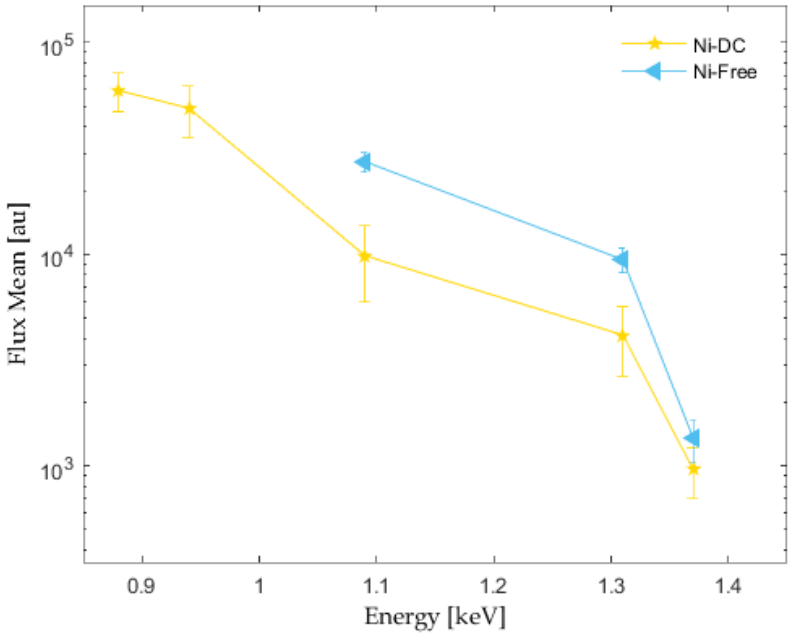

Fig. 4.5.15 – X-ray flux for confined and freestanding NWs as function of the extrapolated energy by 10% of the transmission curve for different thickness absorber.

4.6. Spectrograms analysis

The investigation of ion energy spectra plays a very important role to better understand the nuclear fusion process in a plasma. Ion kinetic energy distribution signals for each charge state were measured using the TPS.

A typical spectrogram contains a bright halo, which constitutes the origin of the parabolic ion traces, due to X-radiation and neutral particle produced by the laser-plasma interaction propagating straight through the

electromagnetic field, and parabolic traces associated to protons and other ions outgoing from the bright region, as shown in Fig. 4.6.1.

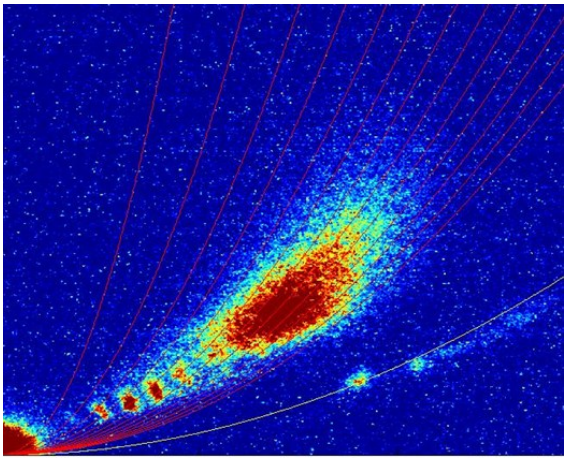

Fig. 4.6.1 – Typical TPS spectrograms.

Since the TPS is optimized to work at higher energies (in the MeV range), the resolution of lower energies (of the order of keV) is poor: is not possible to distinguish nor different ionic species, nor various charge states, which are overlapped to each other. Therefore, investigations are carried out only in aluminum bulk target.

Preliminary results of ion emitted by laser interaction with Al-bulk target allow to observe two separate regions: one related to some ion species characterized by a very narrow energy spread, and the other one that has to be related to the plasma core.

The production of very narrow energy spread protons from aluminum target was predicted in the past [98, 99] and represent the plasma plume multi-fragmentation process, producing bunches of fast ions. In fact, other than the classical hydrodynamic expansion of the plasma, some non linear processes driven by the formation of Double or Multy-layers also occur, all boosted by

the fast expulsion of prompt electrons during the early stage of the laser-target interaction.

The first region is made of small spots characterized low energy spread, which selecting apposite cuts highlight a Gaussian-like distribution with very small energy spread. Each of them with different charge states was fitted and the mean energy was extracted. In Table 4.6.1 the energies of these spots with different charge state are listed.

Ions	***Energy [keV]***
Al^{4+}	34.5 ± 6.2
Al^{5+}	36.6 ± 3.6
Al^{6+}	36.7 ± 4.2
Al^{7+}	37.0 ± 2.9

Table 4.6.1 – Energy of ion bunches with different charge states in Al-bulk targets.

Since the plasma core shows a Maxwellian distribution, it is possible to fit the spectra of the different ion species with a given charge state and to obtain the temperature parameter, listed in Table 4.6.2 for each charge state.

Ions	***Temperature [keV]***
Al^{9+}	11.9 ± 0.3
Al^{10+}	12.0 ± 0.4
Al^{11+}	11.7 ± 0.3
Al^{12+}	11.7 ± 0.3
Al^{13+}	13.8 ± 0.3

Table 4.6.2 – Temperature parameter for some state charge of Al.

4.6.1. Considerations on fusion reaction rates

The next aim is to realize nanostructured deuterated target in order to study the d-d reaction, which can occur through one of the two equal probable reaction channels:

$$d + d \rightarrow T(1.01\ MeV) + p\ (3.02\ MeV)$$

$$d + d \rightarrow\ ^{3}He(0.82\ MeV) + n\ (2.45\ MeV)$$

Therefore, is of crucial importance to calculate the total number of fusion reaction for the future measurements of d-d reaction rates in plasma.

As is well-known, the effectiveness of a fusion fuel is characterized by its reactivity $<\sigma v>$. Curves of the reactivity as a function of the temperature, obtained by numerical integration of Eq. (1.1.10) with the best available cross-sections, are shown in Fig. 4.6.2 for the reactions of interest to controlled fusion. The d-d reaction is the second most probable, at temperatures T <25 keV.

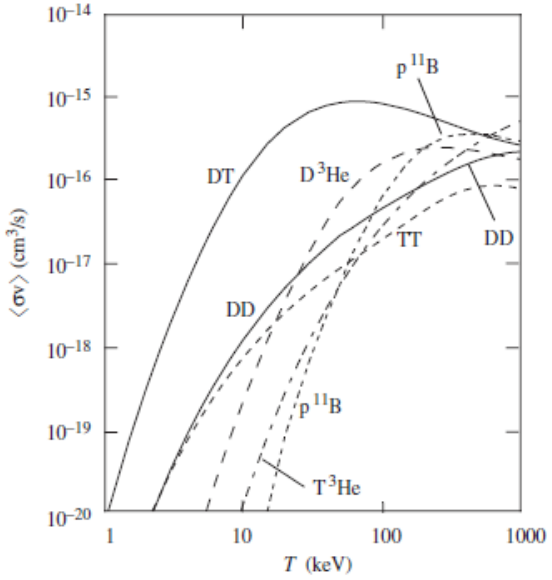

Fig. 4.6.2 – Fusion reactivity, in terms of the average of the fusion cross-section σ over the relative velocities v, vs. plasma temperature for different reactions.

The estimated plasma temperatures with TPS are good in order to expect the occurrence of nuclear fusions. For this reason, the investigation of nanostructured materials is of fundamental importance to optimize their characteristics and to obtain a plasma suitable for nuclear fusion.

However, the effect due to the plasma electrons should not be neglected. Since the ES is not directly measurable, only by comparing the experimental fusion rates with the simulated numbers (with and without screening) it is possible to determine how large is the ES influence.

The procedure to realize deuterated targets consists in a "sealing" process in deuterated water of the target with nanowires deposited in the alumina matrix [100]. In detail, the sample is immersed in boiling deuterated water (at 100° C at atmospheric pressure) for at least 30 minutes. This allows the formation of deuterated hydrates of alumina, which completely seal the tops of the alumina channels, over the nanowires.

Conclusions

High power laser interaction with solids has become an important technique in several scientific disciplines, going from matter science to nuclear physics, to many industrial applications. It is well-established that the absorption of laser light from a solid material leads to very rapid heating of it, resulting in formation of a plasma with high temperature and density.

Laser produced plasma has a very short temporal existence and is transient in its nature, with a fast evolution of the characteristic parameters that are heavily dependent on the irradiation conditions such as incident laser intensity, irradiation spot size, ambient gas composition and pressure, but also they depend on target material.

The investigations made in this work are centered around the characterization and dynamics of plasma generated during Nd:YAG laser ablation in ns domain of bulk and nanostructured targets, with the aim to demonstrate the effectiveness in the production of laser-produced plasmas more hot, dense and stagnant by interaction with nanostructured materials.

Results for different targets are compared in terms of optical and X-ray emission, ion velocity distribution and ablation depth of the produced plasma.

The nanostructured targets used in this study are metamaterials consisting in aligned metal nanowires grown by electrodeposition into a porous alumina matrix, obtained on a thick aluminum substrate. These materials were developed with specific geometrical parameters in order to maximize absorption in the visible and IR wavelengths.

In particular, to study which parameters lead to stagnant plasmas, highest X-ray flux and ablation efficiency, nanowires were produced with different length, diameter, metal and deposition technique.

Large differences have been found among the studied targets.

The first immediate results comes from spatio-temporal evolution in visible region of different plasmas: the Al-Bulk plasma has a shorter duration than all other: this is an evidence of plasma stagnation. At the same times, all nanostructured targets have shown a large increase in both X-ray fluxes and ablation efficiency compared to bulk aluminum.

Substantial differences were also observed between nanostructured targets with different characteristics.

In particular, comparing nanostructured target filled with different metals one can observes that cobalt nanowires have a two-fold increase in X-ray flux compared to nickel, iron and silver nanowires, and deeper craters.

An even larger difference, a factor of five, has been obtained when two different nanowires deposition techniques, alternate current vs. direct current, are applied. Even optical and morphological data are in agreement with X-ray emission measurements. Therefore, DC deposition is promising approach.

The differences highlighted in these measurements between bulk aluminum and nanostructured materials cannot be easily explained considering only the properties of the elements present in the targets, like different atomic number or thermal conductivity of the nanowires. Nor even are related to different reflectivity of targets, since nanostructured targets, with the same absorbance, show divergent characteristics.

A possible explanation for the observed differences is the so-called plasmonic effect, that plays an important role in electromagnetic energy absorption. Due to this effect, the light pulse is converted into an electrical pulse (at the top of the nanowire) and it propagate along the nanowire.

Therefore, differences among targets could be explained in terms of different plasmonic propagation lengths, which is dependent on geometrical parameters of the nanowires and electrical conductivity.

All these experimental evidences and valuations on plasma temperature lead to deem that stagnant plasmas with high temperature and density can be obtained by means of nanostructured materials, with potential application in the study of d-d reaction.

Nanostructured targets filled with deuterium hydrates will be realized in collaboration with INFN nanotechnology lab in Bologna. Neutrons detectors will be placed outside the vacuum chamber to detect the residual neutrons produced in the reaction.

The experiment will give the opportunity to investigate the electron screening in a stellar-like environment.

References

[1] D. D. Clayton, Principles of Stellar Evolution and Nucleosynthesis, Chicago and London: University of Chicago Press, 1968.

[2] H. J. Assenbaum, K. Langanke and C. Rolfs, "Effects of electron screening on low-energy fusion cross sections," *Z. Physik A - Atomic Nuclei ,* vol. 327, no. 4, pp. 461-468, 1987.

[3] T. P. Hughes, "Plasma and laser light," London, Adam Hilger, 1975.

[4] J. F. Ready, "Development of plume of material vaporized by giant-pulse laser," *Appl. Phys. Lett.,* vol. 3, no. 1, p. 11, 1963.

[5] N. G. Basov and O. N. Krokhin, "Conditions for heating up of a plasma by the radiation from an optical generator," *JEPT,* vol. 19, no. 1, p. 123, 1964.

[6] A. W. Ehler and G. L. Weissler, "Vacuum ultraviolet radiation from plasmas formed by a laser on metal surfaces," *Appl. Phys. Lett.,* vol. 8, no. 4, p. 89, 1966.

[7] P. Langer, G. Tonon, F. Floux and A. Ducauze, "Laser induced emission of electrons, ions, and X rays from solid targets," *IEEE J. Quantum Electron.,* vol. 2, no. 9, p. 499, 1966.

[8] E. Archbold and T. P. Hughes, "Electron Temperature in a Laser-heated Plasma," *Nature,* vol. 204, p. 670, 1964.

[9] H. Sonnenberg, H. Heffner and W. Spicer, "Two-photon Photoelectric effect in Cs3Sb," *Appl. Phys. Lett.,* vol. 5, no. 5, p. 95, 1964.

[10] E. M. Logothetis and P. L. Hartman, "Three-Photon Photoelectric Effect in Gold," *Phys. Rev. Lett.,* vol. 18, p. 581, 1967.

[11] N. G. Basov, P. G. Kruikov, S. D. Zakharov, Y. V. Senatskii and S. V. Tchekalin, "Experiments on the observation of neutron emission at the focus of the high-power laser radiation on a lithium deuteride surface," *IEEE J. Quantum Electron.,* vol. 4, p. 864, 1968.

[12] H. M. Smith and A. F. Turner, "Vacuum Deposited Thin Films Using a Ruby Laser," *Appl. Opt.,* vol. 4, p. 147, 1965.

[13] M. P. Kalashnikov, P. V. Nickles, T. Schlegel, M. Schnuerer, F. Billhardt, I. Will, W. Sandner and N. N. Demchenko, "Dynamics of Laser-Plasma Interaction at 1018 W/cm2," *Phys. Rev. Lett.,* vol. 73, no. 2, p. 260, 1994.

[14] T. Tajima and J. M. Dawson, "Laser Electron Accelerator," *Phys. Rev. Lett.,* vol. 43, no. 4, pp. 267-270, 1979.

[15] S. Pfalzner, An Introduction to Inertial Confinement Fusion, New York: Taylor & Francis Group, 2006.

[16] V. L. Ginzburg, Propagation of Electromagnetic Waves in Plasmas, New York: Pergamon Press, 1964.

[17] F. F. Chen, Introduction to plasma physics and controlled fusion, New York: Plenum Press, 1974.

[18] R. J. Goldston and P. H. . Rutherford, Introduction to Plasma Physics, Philadelphia: Institute of Physics Publishing, 1995.

[19] S. Eliezer, The interaction of High-Power Lasers with Plasmas, Philadelphia: Institute od Physics Publishing, 2002.

[20] S. C. Wilks and W. L. Kruer, "Absorption of ultrashort, ultra-intense laser light by solid and overdense plasmas," *IEEE J. Quantum Electron.,* vol. 33, no. 11, pp. 1954-1968, 1997.

[21] D. W. Forslund, J. M. Kindel and K. Lee, "Theory of Hot-Electron Spectra at High Laser Intensity," *Phys. Rev. Lett.,* vol. 39, no. 5, p. 284, 1977.

[22] K. Estabrook and W. L. Kruer, "Properties of Resonantly Heated Electron Distributions," *Phys. Rev. Lett.,* vol. 40, no. 1, p. 42, 1978.

[23] W. L. Kruer, The physics of Laser Plasma Interactions, Redwood City: Addison-Wesley, 1988.

[24] N. G. Denisov, "On a Singularity of the Field on an Electromagnetic Wave Propagated in an Inhomogeneous Plasma," *JETP,* vol. 31, no. 4, p. 609, 1957.

[25] J. P. Freidberg, R. W. Mitchell, R. L. Morse and L. I. Rudsinski, "Resonant Absorption of Laser Light by Plasma Targets," *Phys. Rev. Lett.,* vol. 28, no. 13, p. 795, 1972.

[26] K. G. Estabrook, E. J. Valeo and W. L. Kruer, "Two-dimensional relativistic simulations of resonance absorption," *Phys. Fluids,* vol. 18, no. 9, pp. 1151-1159, 1975.

[27] H. A. Baldis, E. M. Campbel and W. L. Kruer, "Laser plasma interactions," in *Handbook of Plasma Physics Vol. III*, Amsterdam, A. Rubenchik, and R.Z. Sagdeev, 1991.

[28] S. Kneip, B. I. Cho, D. R. Symes, H. A. Sumeruk, G. Dyer, I. V. Churina, A. Belolipetski, A. Henig, O. Wehrhan, E. Förster, T.

D. Donnelly and T. Ditmire, "K-shell spectroscopy of plasmas created by intense laser irradiation of micron-scale pyramid and sphere targets.," *High Energy Density Physics,* vol. 4, no. 1, pp. 41-48, 2008.

[29] S. Mondal, I. Chakraborty, S. Ahmad, D. Carvalho, P. Singh, A. D. Lad, V. Narayanan, P. Ayyub, G. R. Kumar, J. Zheng and Z. M. Sheng, " Highly enhanced hard x-ray emission from oriented metal nanorod arrays excited by intense femtosecond laser pulses.," *Physical Review B,* vol. 83, no. 3, p. 035408, 2011.

[30] T. Nishikawa, S. Suzuki, Y. Watanabe, O. Zhou and H. Nakano, "Efficient water-window X-ray pulse generation from femtosecond-laser-produced plasma by using a carbon nanotube target," *Applied Physics B,* vol. 78, no. 7-8, pp. 885-890, 2004.

[31] A. V. Ovchinnikov, O. F. Kostenko, O. V. Chefonov, O. N. Rosmej, N. E. Andreev, M. B. Agranat, J. L. Duan, J. Liu and V. E. Fortov, "Characteristic X-rays generation under the action of femtosecond laser pulses on nano-structured targets.," *Laser and particle beams,* vol. 29, no. 02, pp. 249-254, 2011.

[32] S. Kahaly, S. K. Yadav, W. M. Wang, S. Sengupta, Z. M. Sheng, A. Das, P. K. Kaw and G. R. Kumar, "Near-complete absorption of intense, ultrashort laser light by sub-λ gratings.," *Physical review letters,* vol. 101, no. 14, p. 145001, 2008.

[33] H. A. Sumeruk, S. Kneip, D. R. Symes, I. V. Churina, A. V. Belolipetski, G. Dyer, A. Bernstein, T. D. Donnelly and T. Ditmire, "Hot Electron and X-ray Production from Intense Laser Irradiation of Wavelength-scale Polystyrene Spheres.," *Physics of plasmas,* vol. 14, no. 6, p. 062704, 2007.

[34] H. A. Sumeruk, S. Kneip, D. R. Symes, I. V. Churina, A. V. Belolipetski, T. D. Donnelly and T. Ditmire, "Control of strong-laser-field coupling to electrons in solid targets with wavelength-scale spheres.," *Physical review letters,* vol. 98, no. 4, p. 045001, 2007.

[35] P. P. Rajeev, P. Taneja, P. Ayyub, A. S. Sandhu and G. R. Kumar, "Metal nanoplasmas as bright sources of hard x-ray pulses.," *Physical review letter ,* vol. 90, no. 11, p. 115002, 2003.

[36] P. P. Rajeev, S. Banerjee, A. S. Sandhu, R. C. Issac, L. C. Tribedi and G. R. Kumar, "Role of surface roughness in hard-x-ray emission from femtosecond-laser-produced copper plasmas.," *Physical Review A,* vol. 65, no. 5, p. 052903, 2002.

[37] L. Cao, Y. Gu, Z. Zhao, L. Cao, W. Huang, W. Zhou, X. T. He, W. Yu and M. Y. Yu, "Enhanced absorption of intense short-pulse laser light by subwavelength nanolayered target," *Physics of Plasmas,* vol. 17, no. 4, p. 043103, 2010.

[38] G. Chatterjee, P. K. Singh, S. Ahmed, A. P. L. Robinson, A. D. Lad, S. Mondal, V. Narayanan, I. Srivastava, N. Koratkar, J. Pasley, A. K. Sood and G. R. Kumar, "Macroscopic transport of mega-ampere electron currents in aligned carbon-nanotube arrays," *Physical review letters,* vol. 108, no. 23, p. 235005, 2012.

[39] P. K. Singh, I. Chakraborty, G. Chatterjee, A. Adak, A. D. Lad, P. Brijesh, P. Ayyub and G. R. Kumar, "Enhanced transport of relativistic electrons through nanochannels," *Physical Review Special Topics-Accelerators and Beams,* vol. 16, no. 6, p. 063401, 2013.

[40] Z. Zhao, L. Cao, L. Cao, J. Wang, W. Huang, W. Jiang, Y. He, Y. Wu, B. Zhu, K. Dong, Y. Ding, B. Zhang, Y. Gu, M. Y. Yu and T. E. He, "Acceleration and guiding of fast electrons by a

nanobrush target," *Physics of Plasmas ,* vol. 17, no. 12, p. 123108, 2010.

[41] S. Bagchi, P. P. Kiran, K. Yang, A. M. Rao, M. K. Bhuyan, M. Krishnamurthy and G. R. Kumar, "Bright, low debris, ultrashort hard x-ray table top source using carbon nanotubes," *Physics of Plasmas,* vol. 18, no. 1, p. 014502, 2011.

[42] U. Chakravarty, V. Arora, J. A. Chakera, P. A. Naik, H. Srivastava, P. Tiwari and P. D. Gupta, "X-ray enhancement in a nanohole target irradiated by intense ultrashort laser pulses," *Journal of Applied Physics,* vol. 109, no. 5, p. 053301, 2011.

[43] P. P. Rajeev, P. Ayyub, S. Bagchi and G. R. Kumar, "Nanostructures, local fields, and enhanced absorption in intense light–matter interaction.," *Optics letters,* vol. 29, no. 22, pp. 2662-2664, 2004.

[44] U. Kreibig and M. Vollmer, "Theoretical Considerations," in *Optical Properties of Metal Clusters*, Springer Berlin Heidelberg, 1995, pp. 13-201.

[45] M. Nikbakht and M. H. Mahdieh, "Local field enhancement of nano-structured metallic target irradiated by polarized laser beam," *Journal of the European Optical Society-Rapid publications,* vol. 7, 2012.

[46] S. Lal, S. Link and N. J. Halas, "Nano-optics from sensing to waveguiding," *Nature photonics,* vol. 1, no. 11, pp. 641-648, 2007.

[47] J. Lima, J. Adam, D. Rego, V. Esquerre and V. Bordo, "Optical properties of nanowire metamaterials with gain," *Optics Communications,* vol. 379, pp. 25-31, 2016.

[48] M. A. Purvis, V. N. Shlyaptsev, R. Hollinger, C. Bargsten, A. Pukhov, A. Prieto, Y. Wong, B. M. Luther, S. Wang and J. J.

Rocca, "Relativistic plasma nanophotonics for ultrahigh energy density physics," *Nature Photonics,* vol. 7, no. 10, pp. 796-800, 2013.

[49] T. Fujimoto, Plasma Spectroscopy, Springer Berlin Heidelberg, 2008.

[50] D. Salzmann, Atomic physics in hot plasmas (No. 97), New York: Oxford University Press on Demand., 1998.

[51] H. R. Griem, Plasma Spectroscopy., New York: McGraw-Hill Book Company, 1964.

[52] D. Giulietti and L. A. Gizzi, "X-ray emission from laser-produced plasmas," *La Rivista del Nuovo Cimento (1978-1999),* vol. 21, no. 10, pp. 1-93, 1998.

[53] A. Martin G. and L. Wiese W., *Chem. Ref. Data,* vol. 15, p. 537, 1983.

[54] S. I. Anisimov, B. S. Luk'yanchuk and A. Luches, "An analytical model for three-dimensional laser plume expansion into vacuum in hydrodynamic regime," *Applied surface science,* vol. 96, pp. 24-32, 1996.

[55] R. K. Singh and J. Narayan, "Pulsed-laser evaporation technique for deposition of thin films: Physics and theoretical model," *Physical Review B,* vol. 41, no. 13, p. 8843, 1990.

[56] Ž. Andreić, D. Gracin, V. Henč-Bartolić, H. J. Kunze, F. Ruhl and L. Aschke, "Dynamics of laser-produced carbon plasma," *Physica Scripta,* vol. 53, no. 3, p. 339, 1996.

[57] B. Toftmann, J. Schou and J. G. Lunney, "Dynamics of the plume produced by nanosecond ultraviolet laser ablation of metals," *Physical Review B,* vol. 67, no. 10, p. 104101, 2003.

[58] B. Doggett and J. G. Lunney, "Expansion dynamics of laser produced plasma," *Journal of Applied Physics,* vol. 109, no. 9, p. 093304, 2011.

[59] F. F. Chen, "Laser accelerators," in *Physics of laser plasma*, 1992, pp. 483-517.

[60] P. Mulser and D. Bauer, High power laser-matter interaction (Vol. 238)., 2010: Springer Science & Business Media.

[61] R. P. Godwin, "Fresnel absorption, resonance absorption, and x rays in laser-produced plasmas," *Applied optics,* vol. 33, no. 6, pp. 1063-1069, 1994.

[62] Y. B. Zeldovich and Y. P. Raizer, "Physics of shock waves and high-temperature hydrodynamic phenomena," 1965.

[63] R. F. Wood, J. R. Kirkpatrick and G. E. Giles, "Macroscopic theory of pulsed-laser annealing. II. Dopant diffusion and segregation," *Physical Review B,* vol. 23, no. 10, p. 5555, 1981.

[64] R. K. Singh, P. Tiwari and J. Narayan, "Nature Of Pulsed Laser Deposition Technique And In-Situ Processing Of YBa2Cu3O7 Superconducting Thin Films," in *International Society for Optics and Photonics*, 1990.

[65] F. Ruhl, L. Aschke and H. J. Kunze, "Selective population of the n= 3 level of hydrogen-like carbon in two colliding laser-produced plasmas," *Physics Letters A,* vol. 225, no. 1, pp. 107-112, 1997.

[66] S. Amoruso, "Modeling of UV pulsed-laser ablation of metallic targets," *Applied Physics A,* vol. 69, no. 3, pp. 323-332, 1999.

[67] J. G. Lunney and R. Jordan, "Pulsed laser ablation of metals," *Applied surface science,* vol. 127, pp. 941-946, 1998.

[68] G. Sony and V. P. N. Nampoori, Application of Imaging to Study the Evolution and Dynamics of Laser Produced Plasma from Solid and Thin Film Li Targets (Doctoral dissertation, Cochin University of Science & Technology)., 2011.

[69] S. Eliezer and H. Hora, "Double layers in laser-produced plasmas," *Physics Reports,* vol. 172, no. 6, pp. 339-407, 1989.

[70] N. M. Bulgakova, A. V. Bulgakov and O. F. Bobrenok, "Double layer effects in laser-ablation plasma plumes," *Physical Review E,* vol. 62, no. 4, p. 5624, 2000.

[71] H. Hora, Laser Plasma Physics: forces and the nonlinearity principle., Spie Press., 2000.

[72] J. Siegel, G. Epurescu, A. Perea, F. J. Gordillo-Vázquez, J. Gonzalo and C. N. Afonso, "Temporally and spectrally resolved imaging of laser-induced plasmas," *Optics letters,* vol. 29, no. 19, pp. 2228-2230, 2004.

[73] W. Whitty and J. P. Mosnier, "Diagnostic of an expanding laser-produced lithium plasma using ICCD frame photography and shadowgraphy," *Applied surface science,* vol. 127, pp. 1035-1040, 1998.

[74] D. B. Geohegan, "Fast intensified-CCD photography of YBa2Cu3O7− x laser ablation in vacuum and ambient oxygen," *Applied physics letters,* vol. 60, no. 22, pp. 2732-2734, 1992.

[75] Andor iStar Intensified Cameras Tecnology User Guide.

[76] Andor Newton X-Ray Tecnology User Guide.

[77] Andor Newton X-Ray Tecnology Specification.

[78] "http://cxro.lbl.gov/," [Online].

[79] M. J. Rhee, "Compact Thomson spectrometer," *Review of scientific instruments,* vol. 55, no. 8, pp. 1229-1234, 1984.

[80] K. Harres, M. Schollmeier, E. Brambrink, P. Audebert, A. Blažević, K. Flippo, D. C. Gautier, M. Geißel, B. M. Hegelich, F. Nürnberg, J. Schreiber, H. Wahl and M. Roth, "Development and calibration of a Thomson parabola with microchannel plate for the detection of laser-accelerated MeV ions," *Review of Scientific Instruments,* vol. 79, no. 9, p. 093306, 2008.

[81] D. Jung, R. Hörlein, D. Kiefer, S. Letzring, D. C. Gautier, U. Schramm, C. Hübsch, R. Öhm, B. J. Albright, J. C. Fernandez, D. Habs and B. M. Hegelich, "Development of a high resolution and high dispersion Thomson parabola," *Review of Scientific Instruments,* vol. 82, no. 1, p. 013306, 2011.

[82] J. A. Cobble, K. A. Flippo, D. T. Offermann, F. E. Lopez, J. A. Oertel, D. Mastrosimone, S. A. Letzring and N. Sinenian, "High-resolution Thomson parabola for ion analysis," *Review of Scientific Instruments,* vol. 82, no. 11, p. 113504, 2011.

[83] R. F. Schneider, C. M. Luo and M. J. Rhee, "Resolution of the Thomson spectrometer," *Journal of applied physics,* vol. 57, no. 1, pp. 1-5, 1985.

[84] H. Masuda and K. Fukuda, "Ordered metal nanohole arrays made by a two-step replication of honeycomb structures of anodic alumina," *Science,* vol. 268, no. 5216, p. 1466, 1995.

[85] M. P. Proenca, C. T. Sousa, J. Ventura, M. Vazquez and J. P. Araujo, "Ni growth inside ordered arrays of alumina nanopores: enhancing the deposition rate," *Electrochimica Acta,* vol. 72, pp. 215-221, 2012.

[86] L. Malferrari, A. Jagminienė, G. P. Veronese, F. Odorici, M. Cuffiani and A. Jagminas, "Alumina Template-Dependant Growth of Cobalt Nanowire Arrays," *Journal of Nanotechnology,* 2009.

[87] O. Jessensky, F. Müller and U. Gösele, "Self-organized formation of hexagonal pore arrays in anodic alumina," *Applied physics letters,* vol. 72, no. 10, pp. 1173-1175., 1998.

[88] R. Angelucci, F. Corticelli, M. Cuffiani, G. M. Dallavalle, L. Malferraxi, A. Montanari, C. Montanari, F. Odorici, R. Rizzoli and C. Summonte, "Application of nanotechnologies in high energy physics," *Nuclear Physics B-Proceedings Supplements,* vol. 125, pp. 164-168, 200..

[89] G. Baraldi, A. Perea and C. N. Afonso, "Dynamics of ions produced by laser ablation of several metals at 193 nm," *Journal of Applied Physics,* vol. 109, no. 4, pp. 043302-043302, 2011.

[90] A. Sunahara and K. A. Tanaka, "Atomic number Z dependence of dynamics of laser-ablated materials," *Fusion Engineering and Design,* vol. 85, no. 6, pp. 935-939, 2010.

[91] S. S. Harilal, R. C. Issac, C. V. Bindhu, V. P. N. Nampoori and C. P. G. Vallabhan, "Time Resolved Analysis of C2 Emission from Laser Induced Graphite Plasma in Helium Atmosphere," *Japanese journal of applied physics,* vol. 36, no. 1R, p. 134, 1997.

[92] W. Sesselmann, E. E. Marinero and T. J. Chuang, "Laser-induced desorption and etching processes on chlorinated Cu and solid CuCl surfaces," *Applied Physics A: Materials Science & Processing,* vol. 41, no. 3, pp. 209-221, 1986.

[93] Y. Iida, "Effects of atmosphere on laser vaporization and excitation processes of solid samples," *Spectrochimica Acta Part B: Atomic Spectroscopy,* vol. 45, no. 12, pp. 1353-1367, 1990.

[94] T. P. Tooman, "The Sandia laser plasma extreme ultraviolet and soft x-ray (XUV) light source.," in *In 1986 Quebec Symposium (pp. 186-193). International Society for Optics and Photonics.*, 1986.

[95] G. M. Davis, M. C. Gower, F. O'Neill and I. C. E. Turcu, "Plasma x-ray source for lithography generated by a≅ 30 J, 30 ns KrF laser," *Applied physics letters,* vol. 53, no. 17, pp. 1583-1585, 1988.

[96] K. M. Glibert, J. P. Anthes, M. A. Gusinow, M. A. Palmer, R. R. Whitlock and D. J. Nagel, "X-ray yields of plasmas heated by 8-nsec neodymium laser pulses.," *Journal of Applied Physics,* vol. 51, no. 3, pp. 1449-1451, 1980.

[97] M. Frassetto, Study of nanostructured targets for plasma production via laser ablation. Master Thesis, Università degli Studi di Bologna, Italia, 2016.

[98] D. Mascali, S. Tudisco, N. Gambino, A. Pluchino, A. Anzalone, F. Musumeci, A. Rapisarda and A. Spitaleri, "Prompt electrons driving ion acceleration and formation of a two-temperature plasma in nanosecond laser-ablation domain," *EPL (Europhysics Letters),* vol. 100, no. 4, 2012.

[99] S. Tudisco, D. Mascali, N. Gambino, A. Anzalone, S. Gammino, F. Musumeci, A. Scordino and A. Spitaleri, "Investigation of laser-produced aluminum plasma," *Nuclear Instruments and Methods in Physics Research Section A,* vol. 653, no. 1, pp. 45-51, 2011.

[100] L. Hao and B. R. Cheng, "Sealing processes of anodic coatings—past, present, and future," *Metal Finishing,* vol. 98, no. 12, pp. 8-18, 2000.